

Northumbria Research Link

Citation: Nkor, John Vurebari Koko (2021) Comparative life cycle and technical-economic analysis of renewable energy technologies and numerical modelling of heat pipes for application in solar thermal plants. Doctoral thesis, Northumbria University.

This version was downloaded from Northumbria Research Link:
<http://nrl.northumbria.ac.uk/id/eprint/48238/>

Northumbria University has developed Northumbria Research Link (NRL) to enable users to access the University's research output. Copyright © and moral rights for items on NRL are retained by the individual author(s) and/or other copyright owners. Single copies of full items can be reproduced, displayed or performed, and given to third parties in any format or medium for personal research or study, educational, or not-for-profit purposes without prior permission or charge, provided the authors, title and full bibliographic details are given, as well as a hyperlink and/or URL to the original metadata page. The content must not be changed in any way. Full items must not be sold commercially in any format or medium without formal permission of the copyright holder. The full policy is available online: <http://nrl.northumbria.ac.uk/policies.html>

**COMPARATIVE LIFE CYCLE AND
TECHNICAL-ECONOMIC ANALYSIS OF
RENEWABLE ENERGY TECHNOLOGIES
AND NUMERICAL MODELLING OF HEAT
PIPES FOR APPLICATION IN SOLAR
THERMAL PLANTS**

John V.K. NKOR

PhD

2021

**COMPARATIVE LIFE CYCLE AND TECHNICAL
ECONOMIC ANALYSIS OF RENEWABLE ENERGY
TECHNOLOGIES AND NUMERICAL MODELLING OF
HEAT PIPES FOR APPLICATION IN SOLAR THERMAL
PLANTS**

JOHN VUREBARI KOKO NKOR

A thesis submitted in partial fulfilment
of the requirements of the
University of Northumbria at Newcastle
for the degree of
Doctor of Philosophy

Research undertaken in the
Faculty of Engineering and Environment

June 2021

Abstract

This research presents a comparison between mainstream and emerging solar-thermal renewable energy technologies (RETs) using an integrated environmental and techno-economic assessment framework and the numerical modelling of heat pipes for solar thermal applications. Using the framework, the overall sustainability potential is quantified in terms of a novel environmental and techno-economic index (ETEI), combining the Levelised Life Cycle Impact (LLCI) with the Levelised Cost of Energy (LCOE). A set of three ‘mainstream’ (Photovoltaic-PV, Wind Turbine-WT, Bioenergy) and three ‘solar-thermal’ (Parabolic Trough Steam-driven turbine, Parabolic Trough and Linear Fresnel Reflectors, the latter two with Organic Rankine Cycle, respectively PT-ORC and LFR-ORC) RETs are used. Economic and environmental evaluation of the RETs for technological innovation is relevant in making an informed decision as to the value these technologies present. Hence, this study also assesses the efficiency of technical innovations of the six RETs, using the eco-efficiency approach by integrating life cycle assessment and life costing. A demonstration case study is presented for two sites with favourable renewable resources over 25-year operational life. The results show improved overall sustainability scores for solar-thermal, attributed mainly to the additional thermal energy recovery from the ORC. PV emerges as the most preferred option when only electricity generation is considered, whereas accounting for the additional thermal energy outputs makes PT-ORC as the most preferred option during to its technological maturity and LFR-ORC the second preferred option.

The transient behaviour of a heat pipe, designed by an industrial partner of the Northumbria University team, leading Horizon 2020 R & I Activity Project on the development of a small solar thermal plant, was investigated numerically. The heat pipe is a part of the plant, and its operation was studied for different tilt angles ($\theta = 0^\circ, 45^\circ, 90^\circ$). The numerical solutions were obtained using a fully implicit Finite Difference Method that considered the motion of the liquid and a known time-varying temperature boundary condition at the liquid front. The liquid front position was found to be dependent on the applied heat flux, the initial conditions, and the thermophysical properties of the working fluid. Additionally, the distribution of power output and wall temperatures was predicted.

The temperature distribution of the working fluid was consistent with experimental results from the previous literature and provided valuable insight into the room-temperature start-up phenomenon.

Contents

Abstract.....	iii
Contents.....	v
List of Figures.....	viii
List of Tables.....	x
Acknowledgements	xi
Declaration	xii
Nomenclature.....	xiii
Chapter 1 Introduction.....	1
1.1 Problem Statement	1
1.2 Research Objectives	4
1.3 Contribution to Knowledge	5
1.4 Structure of the thesis	6
Chapter 2 Background	8
2.1. Energy and sustainable development	8
2.2. Solar thermal concentrator types	10
2.2.1. Power Tower	11
2.2.2. Dish/Stirling	12
2.2.3. Parabolic Trough	12
2.2.4. Linear Fresnel Reflector	14
2.2.5. The overall concept of CSP plant technologies	15
2.3. Organic Rankine Cycle	18
2.3.1. ORC configurations	19
2.3.2. Selection of Organic working fluid	22
2.4. Energy storage technologies.....	25
2.4.1. Chemical energy storage system.....	25
2.4.2. Electrical energy storage system.....	25
2.4.3. Mechanical storage system	26
2.4.4. Thermal storage system	27
2.5. Heat pipe.....	28
2.6. Review of related works	31
2.7. Chapter summary.....	41
Chapter 3 Methodology	42
3.1. Integrated performance assessment framework	42

3.2. Life cycle assessment (LCA).....	44
3.2.1. Goal and scope definition	44
3.2.2. Inventory analysis.....	44
3.2.3. Impact assessment.....	44
3.2.4. Interpretation	45
3.2.5. Impact assessment (Environmental)	46
3.3. Life cycle costing (LCC)	48
3.4. Techno-economic analysis.....	50
3.5. Integrated performance index	51
3.6. Heat pipe deployment justification.....	53
3.7. Chapter summary.....	54
Chapter 4 Software and analytical tools	55
4.1 Umberto Software	55
4.2 System Advisor Model (SAM)	55
4.3 ANSYS	56
4.4 Matrix Laboratory (MATLAB).....	56
4.5 Life cycle assessment assumptions	57
4.6 Techno-economic assessment assumptions.....	57
4.6.1. Wind turbine system	58
4.6.2. Photovoltaic system.....	59
4.6.3. Biomass system	61
4.6.4. Concentrated Solar Power (CSP) system.....	61
4.7. Location	62
4.8. Chapter summary.....	64
Chapter 5 ETEA Results and Discussions	65
5.1. Case study	65
5.1.1. Scenario 1 (Spain).....	68
5.1.2. Scenario 2 (United States)	76
5.1.3. Validation.....	79
5.2. Chapter summary.....	80
Chapter 6 Computational fluid dynamics	81
6.1. Introduction	81
6.2. Numerical Model description	83
6.2.1. Governing equations.....	84

6.2.2. Multiphase model	87
6.2.3. Volume of Fluid (VOF) model	88
6.2.4. Mass and heat transfer during the evaporation and condensation processes 89	
6.2.5. Turbulence model.....	90
6.3. The example of the Computation Domain creation	90
6.4. Mesh generation	92
6.5. Boundary conditions applied in modelling heat pipes.....	94
6.6. Convergence criterion	95
6.7. Chapter summary.....	96
Chapter 7 CFD Modelling Results and Discussion.....	97
7.1. Simulations method for different tilt angles of the heat pipe	97
7.2. Examples of CFD results with visualisation of processes in the heat pipes....	102
7.3. CFD results for the Thermacore heat pipe (for application in a solar thermal plant) 105	
7.4. Validation of CFD modelling method by thermal studies	113
7.5. Further validation of the CFD modelling method for a heat pipe	119
7.5.1. Comparison with data for a copper wrapped screen wick.....	120
7.6. Chapter summary.....	124
Chapter 8 Conclusions and recommendations.....	125
8.1. Conclusions.....	125
8.2. Recommendations for future work	128
References	129
APPENDIX A.....	139
APPENDIX B.....	147
B1. 15% water-liquid filled ratio.....	147
B2. Water-vapour and Water-liquid volume of fraction.....	148
B3. Temperature profile	153
B4. Boundary Conditions	156
APPENDIX C	158
C1. UDF code for Heat Pipe	158
C2. UDF to reset the operating pressure	162

List of Figures

Figure 2.1: CSP global capacity (TWh) [35]	10
Figure 2.2: A generic CSP plant [36]	11
Figure 2.3: Power tower technology for generating electricity	12
Figure 2.4: Dish-Stirling System [38]	13
Figure 2.5: Simplified schematic of a parabolic trough power plant [39]	13
Figure 2.6: A linear Fresnel reflector system with a secondary reflector on top of the receiver [37]	14
Figure 2.7: Thermal efficiency for different collector technologies [41]	17
Figure 2.8: The schematic layout of a simple ORC system	19
Figure 2.9: Temperature-entropy of the simple ORC	20
Figure 2.10: The schematic layout of the recuperated ORC	21
Figure 2.11: Temperature-entropy diagram of the recuperated ORC	22
Figure 2.12: Temperature-entropy diagram of dry, isentropic, and wet fluids	23
Figure 2.13: Saturated vapour specific volume plotted against saturated temperature for water as well as some common refrigerants	24
Figure 2.14: Typical operation of steady-state heat pipe	29
Figure 2.15: Liquid-Vapour radii curvature in the (a) evaporator and (b) condenser sections	30
Figure 2.16: Heat pipe transient start-up profiles (a) Uniform (b) Frontal, and (c) Non-condensable gas with Frontal [98]	37
Figure 3.1: Schematic of the proposed integrated assessment framework	43
Figure 3.2: Life cycle boundary of the scoped RETs	45
Figure 3.3: Eco-efficiency performance indicator graph	52
Figure 4.1: Map of Spain	63
Figure 5.1: Global and beam irradiance for Spain	66
Figure 5.2: A plot showing the resource for wind speed, wet and dry temperatures in Spain	66
Figure 5.3: Global and beam irradiance for the United States	67
Figure 5.4: A plot showing the resource for wind speed, wet and dry temperatures in the United States	67
Figure 5.5: User demand profile used for the simulation of RETs	68
Figure 5.6: Annual energy output from different RETs (Note: left y-axis - Electrical energy only; right y-axis – Total energy, i.e. electrical and thermal combined, respectively shown as + and O) in Spain	69
Figure 5.7: Levelised life cycle impact of the RETs (Note: left y-axis – accounting for Electrical energy only; right y-axis – accounting for Total energy, i.e., electrical, and thermal combined, respectively shown as O and +) in Spain	70
Figure 5.8: Levelised cost of energy for the scoped 2 MW RETs in Spain	73
Figure 5.9: Eco-efficiency index scores	75
Figure 5.10: Annual energy output from different RETs (Note: left y-axis - Electrical energy only; right y-axis – Total energy, i.e., electrical and thermal combined, respectively shown as + and O) in the U.S.	77
Figure 5.11: Levelised cost of energy for the scoped 2 MW RETs in the U.S	78
Figure 6.1: The disciplines within CFD	82
Figure 6.2: Fluent process for performing simulations	83

Figure 6.3: The fluid element for demonstration of conservation laws [179]	84
Figure 6.4: Illustration of flow regimes [181]	87
Figure 6.5: Heat pipe geometry (a) Average temperature recorder sections (b) diameter of different parts (c) length of evaporator and condenser section	91
Figure 6.6: 2D and 3D computational domain general terminologies	92
Figure 6.7: Mesh generation for the 45 degrees heat pipe showing the evaporator and condenser sections	93
Figure 6.8: Mesh generation on the geometry surface	94
Figure 7.1: Three heat pipe orientations.....	97
Figure 7.2: Boiling process in the wicked heat pipe for temperature heat input of 333.15 K.....	103
Figure 7.3: Vapour volume fraction of horizontal heat pipe with 300 W constant heat input	104
Figure 7.4: Heat input rate in the evaporator for the temperature of the evaporator at 303.15 K.....	106
Figure 7.5: Heat rejection rate in the condenser for the temperature of the evaporator at 303.15 K.....	107
Figure 7.6: Variation of the liquid and vapour volume of fraction as a function of time (without dry-out)	107
Figure 7.7: Heat input rate in the evaporator for the temperature of the evaporator at 333.15 K.....	108
Figure 7.8: Heat rejection rate in the condenser for the temperature of the evaporator at 333.15 K.....	108
Figure 7.9: Heat transfer rate in the heat pipe as a function of the evaporator temperature for different tilt angles.....	113
Figure 7.10: Average temperature distribution in the heat pipe as a function of constant temperature heat input boundary condition at different tilt angles (a) vertical (b) 45 degrees and (c) horizontal.....	114
Figure 7.11: Average temperature distribution in the heat pipe as a function of constant heat input rate boundary condition at different tilt angles (a) vertical (b) 45 degrees and (c) horizontal	115
Figure 7.12: Dimensions (a) and schematic details (b) of heat pipe by Yan and Ochterbeck 1996 [191]	116
Figure 7.13: Validation and comparison of the current model with [191] without (a) and with (b) evaporation along the wetting region in the evaporator	118
Figure 7.14: Comparison of Transient Heat Pipe Temperature Profiles with Experimental Data in [101]	121
Figure 7.15: Comparison of liquid front position with experimental data in [101]	122
Figure 7.16: Liquid front position for 225 W (experimental and current) and 300 W (current study) predicting dryout.....	123

List of Tables

Table 2.1: The comparison of the different CSP technologies	16
Table 3.1: ILCD impact assessment method	47
Table 3.2: Life Cycle cost approaches	50
Table 4.1: CSP technology-specific design parameters.....	58
Table 4.2: Wind Turbine system cost.....	59
Table 4.3: Power-wall Specifications for PV system [12]	60
Table 4.4: PV system configuration	60
Table 4.5: PV system costs [12]	60
Table 4.6: Biomass system costs [160].....	61
Table 4.7: System costs for the modelled CSPs [153, 154, 156]	62
Table 5.1: Life cycle impacts of the scoped renewable energy technologies (kg/kWh)	71
Table 5.2: Comparison of actual/simulated published data and simulated data from this research	71
Table 5.3: Economic indicators of renewable energy technologies in Spain	74
Table 5.4: Economic indicators of renewable energy technologies in the U.S	79
Table 7.1: Comparison between horizontal heat pipe experimental data input rate of 172.87 W [188] and CFD simulated heat pipe with 145 W heat input rate.....	110
Table 7.2: Heat transfer rates in the heat pipe as the function of time and tilt angle for the temperature of the condenser at 353.15 K	110
Table 7.3: Heat transfer rates in the heat pipe as the function of time and tilt angle for the temperature of the condenser at 373.15 K	111
Table 7.4: Heat transfer rates in the heat pipe as the function of time and tilt angle for the temperature of the condenser at 393.15 K	112
Table 7.5: Summary of new heat pipe design parameters for the current study	117
Table 7.6: Heat pipe design parameters by [101]	119

Acknowledgements

First and foremost, I want to thank the Almighty God for grace, enablement, and strength for striving for the completion of this programme, despite the challenges along the way.

A PhD could be compared to running a marathon and at the very top, to whom I owe much gratitude is my supervisor, Professor Khamid Mahkamov for his mentorship, continuous backing, and encouragement throughout the completion of my doctoral work. His patience, thoughtful discussions and professionalism about the physical model served as an inspiration. He ensured I left no stone unturned to obtain impeccable results and presentation.

I would like to specially appreciate my parents, my brother and my sister who have so much faith in me for being very supportive and from which I sometimes draw strength and motivation for accomplishing this goal.

I am also grateful to Dr. Madeleine Combrinck for her technical input in the early stages of my work. Her suggestions and input served as a foundation that other findings were built upon.

I want to sincerely appreciate all the members of the Department of Mechanical and Construction Engineering at Northumbria University for creating a conducive environment to work in. I also want to thank Shivam Salokhe my PhD colleague for his wealth of knowledge in computational fluid dynamics from whom I learnt a great deal from. I also want to acknowledge my other PhD colleague in the Wynne Jones Building and the Futsal team for making Friday evenings before the lockdown memorable. To the technical and IT staffs, you have made my stay worthwhile.

Additionally, I am truly thankful to Pastor Dr. Samuel Ohiomokhare, James Udia and the entire DLBC Northeast and Cumbria Region, England for their prayers and financial support. They have truly created for me a home away from home.

Lastly, to all those friends, colleagues, and family members I have not mentioned by name, I am extremely thankful that you are in my life.

Declaration

I declare that the work contained in this thesis has not been submitted for any other award and that it is all my own work. I also confirm that this work fully acknowledges opinions, ideas, and contributions from the work of others.

Any ethical clearance for the research presented in this thesis has been approved. Approval has been sought and granted by the Faculty Ethics Committee on **27-08-2019**.

I declare that the Word Count of this Thesis is 28,610 words

Name: John V.K. Nkor

Signature:

Date: June 2021

Nomenclature

A	rotor area [m ²]
A_{pv}	photovoltaic module area [m ²]
A_e	external surface area of evaporator [m ²]
A_c	external surface area of condenser [m ²]
c	cost factor [\$]
C_{tot}	total thermal capacity of the heat pipe [J/K]
CO ₂	Carbon dioxide
d	degradation factor [%]
D	disposal factor [%]
E	external cost factor in the life cycle stage [\$]
E_t	electricity discounted value [%]
e_{out}	annual electricity output [MW]
E_{fuel}	emission factor [%]
eq	Equilibrium
F_t	fuel cost [\$]
G_k	turbulence kinetic energy generation [J/kg]
h	sensible enthalpy [J/kg]
H_{fg}	latent heat of liquid-vapor phase-change [kJ/kg]
I	solar irradiance [W/m ²]
I_t	cost of investment [\$]
\bar{J}_j	diffused heat flux [W/m ²]

k	dimensionless shape parameter
k_{eff}	effective conductivity [W/mK]
L	total heat pipe length [m]
M_t	cost for operations and maintenance [\$]
P_l	liquid pressure [Pa]
P_v	vapor pressure [Pa]
r	discount rate [%]
r_{cc}	effective capillary radius at condenser [m]
r_{ce}	effective capillary radius at evaporator [m]
S_{fuel}	annual carbon savings
S_m	mass added to the continuous phases by the water-liquid phases [kg]
S_{Mx}	source terms of x of the momentum equation [kgm/s]
S_{My}	source terms of y of the momentum equation [kgm/s]
S_{Mz}	source terms of z of the momentum equation [kgm/s]
S_h	volumetric heat sources and the heat chemical reaction
T	temperature [K]
t	time [s]
T_∞	ambient temperature [K]
T_{CLCC}	total conventional life cycle cost
T_{ELCC}	total environmental life cycle cost
T_{mix}	mixture temperature [K]
T_{sat}	saturation temperature [K]

V	wind speed [m/s]
x	cost element of nn
α_L	liquid volume fraction
α_V	vapour volume fraction
$\dot{m}_{e \rightarrow v}$	rate of mass transfer from liquid to vapour phase [kg/s]
$f(V)$	Weibull probability wind speed distribution function
ρ	air density [kg/m ³]
η_{pv}	overall efficiency of the photovoltaic unit [W/m ²]
δ	wall thickness [m]

Abbreviations

CFD	Computational Fluid Dynamics
CFC-11	Chlorofluorocarbon
CSP	Concentrated Solar Power
CTUe	Comparative Toxic Units ecotoxicity
CTUh	Comparative Toxic Units for humans
C ₂ H ₄	Acetylene
ETEI	Environmental and Techno-Economic Index
H ⁺	Hydrogen ion
LCA	Life Cycle Assessment
LCC	Life Cycle Costing

LCOE	Levelised Cost of Energy
LFR	Linear Fresnel Reflectors
LLCI	Levelised Life Cycle Impact
N	Nitrogen
NPV	Net Present Value
OECD	Organization for Economic Cooperation and Development
ORC	Organic Rankine Cycle
P	Phosphorus
PM2.5	Particulate matter
PT	Parabolic Trough
PV	Photovoltaic
RETs	Renewable Energy Technologies
SAM	System Advisor Model
Sb	Abiotic depletion potential
SOC	Soil Organic Carbon
TRL	Technology Readiness Level
U-235	Uranium-235
VOF	Volume of Fluid
WT	Wind Turbine

Chapter 1 Introduction

This Chapter discusses several critical global issues affecting the world's current energy demand and the potential for addressing some of these issues using renewable energy technologies. Additionally, the chapter discusses the motivation for developing an integrated environmental and economic framework for comparing renewable energy technologies and the operation of the heat pipe, along with the thesis's objectives, contribution to knowledge and structure.

1.1 Problem Statement

Between 2018 and 2050, global energy consumption is expected to increase by nearly 50%. It will be mainly driven by strong economic growth in countries in the Asia region, not in the Organization for Economic Cooperation and Development (OECD) [1]. However, alongside the rise in energy demand, there is also expected improvements in energy efficiency, availability of cleaner energy and reductions in the cost of energy for consumers [2]. Recently, disruptions in the energy sector have been caused by the Covid-19 pandemic, and the impact could be felt in the years to come [3]. The uncertainty surrounding the pandemic's duration, its social and economic consequences, and the energy policy responses open a vast array of possible energy futures. Global oil consumption reached 4,216 million tonnes per day in 2014, with a daily demand of 92.7 million barrels. Global oil consumption increased to 4,474 million tonnes per day in 2019, and global demand reached 100.1 million barrels per day [4]. However, the projected global demand for oil in 2020 decreased to 91.3 million barrels per day as a result of the pandemic's economic and mobility effects [5]. While fossil fuels are depleting on a daily basis, there is evidence that the world continues to require additional energy; thus, it is critical to develop new energy technologies and resources to meet global energy demand. In fulfilling the astronomical demand for clean energy, the transition to sustainable energy is expected to see a revolution in the renewable energy technology sector. At the same time, the climate emergency requires a drastic reduction in the global greenhouse gas emissions by 50% up to 2050. Hence, the European climate strategy seeks innovative approaches to attaining a carbon-neutral energy sector by 2050 [6].

Over the last decade, a plethora of renewable energy technologies (RETs) has emerged globally, leading to competitive scrutiny of their environmental and techno-economic viability [7-19]. There is an increasing demand to pursue power technologies that are both techno-economically efficient (including their life span and end-of-life decommissioning costs) and environmentally benign (in terms of their cradle-to-grave resource demands and emissions burdens) [20]. However, there is a lack of a clear approach in ascertaining the holistic sustainability of innovative RETs, specifically in terms of the following questions - a) How technologically viable it is? b) Can it be replicated at a low manufacturing cost and still meet the minimum energy performance ratio? c) Is it environmentally benign across its life cycle stages?

Renewable energy, according to the International Renewable Energy Agency, is undergoing a virtuous cycle of technological advancement and cost reduction. There has been a steady decline in the manufacturing cost of popular RETs, such as wind turbine, solar-thermal, photovoltaics, and biomass. Furthermore, the operation and maintenance (O&M) cost of these RETs has been significantly reduced using real-time data to enhance predictive maintenance [21]. These relative cost changes are altering the comparative economics of the production of energy from renewable resources. Nevertheless, additional cost reductions could be realised through further technological enhancements, competitive procurement, and efficient project implementation [21-23]. Apart from manufacturing, transport (and in some cases assembly) stages, emissions from operating RETs have significantly diminished.

Galiana and Green [24] argued that fostering a "technological revolution" in the field of RET would help to mitigate the challenges society face as a direct consequence of the inevitable environmental impacts caused by the use of conventional energy. A range of solar energy technologies has become available with differing performance characteristics. The two types of solar energy technologies widely available for generating power are photovoltaic (PV) and concentrated solar power (CSP) [25, 26]; scholars and industry experts have widely debated the worthiness of each for large-scale implementation to generate electricity [27, 28]. Component manufacturing contributes significantly to the systems scale environmental and techno-economic performance for

RETs. This typically includes readily installable preconstructed modules bought 'off-the-shelf', usually manufactured in another country with significant transportation burdens. To date, the uptake of these technologies has been determined mainly by their capital and operation & maintenance costs, which in turn depend on the type of material used in component manufacturing [29]. Challenges faced presently require not only responsive and productive systems but eco-efficient ones, which are concerned with minimising all sorts of waste. In essence, the eco-efficient approach must be implemented without increasing production costs and without causing any unintended immediate or future external environmental consequences [30] in order to achieve full sustainability. The concept of eco-efficiency allows for a desirable assessment of the co-benefits (Life cycle assessment and Life cycle costing) of technological innovations [19].

This research examines the integration of a Linear Fresnel Reflector and an Organic Rankine Cycle (LFR-ORC) technologies to generate electricity. As it can be seen from the review of literature in Chapter 2, there has been no published work related to the comprehensive study (environmental, energy, and economic) of the LFR-ORC systems. Therefore, this work systemically compares the LFR-ORC systems integration relative to the other five mainstream RETs to evaluate their energy output, environmental and economic performance, as described in Chapter 3. A sensitivity analysis performed for the LFR-ORC identified the heat pipe as the prospective component to be used in solar plants and the importance of their investigation in terms of heat transfer performance. For this reason, this work deploys 3-D CFD numerical models to study the phase change in the evaporator and condenser sections of the different heat pipe orientations to indicate how improvements can be made for solar thermal application. Existing heat pipe technologies must be significantly improved to meet higher heat transfer capabilities for thermal storage in solar thermal plants. By optimising the geometric and operating parameters, the heat transfer limit should be increased. To accurately predict the heat transfer limit and temperature distribution of a heat pipe, a three-dimensional heat transfer and flow CFD model encompassing both liquid and vapour must be developed. Literature search shows a very significant gap in presenting details and results of CFD modelling of heat pipes. In this study, a detailed three-dimensional CFD approach was used to simulate the heat pipe's steady-state performance. In the modelling process, it is taken

into account that a porous wick structure made of copper metal is used to transport the liquid from the condenser to the evaporator. Water is used as the working fluid because it has a high latent heat of vaporisation and is compatible with copper.

1.2 Research Objectives

This thesis aims to develop a methodology that assesses the environmental and techno-economic performance of six renewable energy technologies (RETs). This methodology would then be used to evaluate the competitiveness of the LFR-ORC relative to the other five mainstream RETs. This study also seeks to numerically investigate the performance of a heat pipe for solar thermal plant application by means of the 3-D CFD modelling technique. To evaluate the performance and competitiveness of the RETs and numerically analyse the performance of a heat pipe for solar thermal application, the following research objectives have been formulated:

1. To identify the environmental impacts which could affect the performance of the different RETs.
2. To quantify the techno-economic factors influencing the performance of the RETs.
3. To compare the performance of mainstream RETs with the LFR-ORC using an integrated sustainability assessment framework by employing a trade-off assessment and optimisation system.
4. To develop the detailed CFD model of heat transfer and flow of the heat pipe for solar thermal application.
5. To numerically investigate the operation of the heat pipe and to determine the effect of adding wick on the thermal performance of the heat pipe with different orientations.

The first objective seeks to identify the environmental criteria that are most relevant regarding sustainable practices using the conventional life cycle assessment (LCA) approach. It also aims to recognise materials and processes with high impacts on the environment and use appropriate environmental indicators to quantify the impacts.

The second objective quantifies the impacts breakthrough research and development have on the economic viability of an integrated process (outlining the low-cost potentials

of the integrated system, as well as identifying cost drivers and metrics for overall cost reductions).

The third objective focuses on how to identify direct linkages and trade-offs between the environmental and techno-economic assessment models while evaluating the benefits of the environmental measures and the corresponding economic impacts (maximise economic value (e.g., NPV) and minimise environmental impact (e.g., Global warming)). It also seeks to investigate improvement scenarios and alternatives through sensitivity analysis to infer the role of innovations and optimisation for performance enhancement for the LFR-ORC energy system.

The fourth and fifth objectives are to develop the numerical model and investigate the performance of the heat pipe for the solar thermal plant and the thermal effectiveness of wicks for the three pipe orientations, namely 0° (horizontal orientation), 45° and 90° (vertical orientation).

As a first step, a comprehensive environmental and techno-economic assessment (ETEA) framework, specific to the evaluation of RETs to the appropriate Technology Readiness Level (TRL)¹, is developed. TRL is a concept introduced by the National Aeronautics and Space Administration (NASA) to allow for a more effective assessment regarding the maturity of new technologies [31]. It builds on the eco-efficiency assessment, which combines Life cycle assessment (LCA) and Life cycle costing (LCC) and a methodology previously applied for the evaluation of algal-based biorefinery [32].

1.3 Contribution to Knowledge

The research is novel in that it develops a methodology for evaluating the environmental and economic performance of renewable energy technologies and a simplified numerical model for investigating the heat transfer processes in a wick heat pipe. This thesis makes the following knowledge contributions to the field of renewable energy technology:

¹ TRL refers to a categorization measure for the “functional maturity” of a particular technology

1. The developed and proposed methodology for evaluating the environmental and techno-economic performance of RETs which can provide a reference point for researchers, policymakers, and stakeholders with interest in developing new RETs that are sustainable and efficient. The research provided important information about key indicators which determines the cost drivers and metrics for overall cost reductions of RETs.
2. The developed environmental and techno-economic assessment framework which provides general indications to determine the Levelized cost of energy, energy payback time, global warming potential, and the energy return on investment.
3. The developed detailed 3-D CFD model of heat transfer and flow in the heat pipe with wick and information on operation and performance of such a device installed at different orientations.

1.4 Structure of the thesis

This thesis is organised in the following manner to provide a coherent framework:

1. Chapter 2 discusses the background and provides an overview of renewable energy technologies. It then discusses the Linear Fresnel Reflector and the Organic Rankine Cycle technologies, as well as their relationship. State of the art on R & D of heat pipes is also discussed to gather data on relevant physical phenomena during operation of heat pipes. Related and previously published works are discussed and briefly described.
2. Chapter 3 contains the methodology for assessing the RETs' life cycle and techno-economic impacts. Additionally, it introduces the integrated performance assessment framework, a novel concept for holistically assessing the sustainability of RETs using their Levelized Life Cycle Impact (environmental parameter) alongside its Levelised Cost of Energy (conventional techno-economic parameter).
3. Chapter 4 briefly describes the software and analytical tool used for the modelling process as well as the assumptions made for the life cycle assessment and techno-economic assessment. It also justifies the reason for numerically investigating the different heat pipes orientation and presents brief information on the locations for the different RETs.

4. Chapter 5 presents the results and analyses of the RETs case study scenarios. It begins by evaluating the capacities of the RETs, considering the design parameters and the environmental and techno-economic assumptions.
5. Chapter 6 introduces the computational fluid dynamics (CFD) techniques and the theories applied in the analysis of the heat pipe. The governing partial differential equations of conservation of mass, momentum, and energy for the heat pipe. In addition, the geometry, meshing and boundary conditions of the heat pipe is also described. ANSYS Fluent is used to perform numerical simulations to provide the liquid and vapour fraction, average temperature, and power of the evaporator and condenser zone of the heat pipe.
6. Chapter 7 discusses the numerical results obtained from numerical modelling of the operation of the heat pipe with different orientations. Additionally, it compares the numerical heat pipe model's output to published studies in the literature.
7. Chapter 8 collects the main conclusions of the research by comparing findings against the objectives and provides some guidance on possible future work.

Chapter 2 Background

This Chapter establishes the necessary background context for this study. The first section discusses energy and sustainable development, as well as providing an overview of renewable energy technologies. The second section provides an in-depth examination of recent developments in concentrated solar power (CSP), particularly linear Fresnel reflectors (LFR). The third section would describe the LFR and its other components. Section four presents a state-of-the-art LFR coupled with an organic Rankine cycle (ORC) for electrical and thermal applications. Section five discusses related and existing works, and section six concludes the Chapter.

2.1. Energy and sustainable development

Sustainable development can be broadly defined as meeting the current needs of the present without jeopardising future generations' ability to meet their own. In the twenty-first century, sustainable development has become a guiding principle for policymaking. The World Commission on Environment and Development's seminal 1987 report was instrumental in popularizing the concept of sustainable development. The word 'development' in an international context refers to simply improvement in the quality of life. Sustainable development's sole objective is to improve while preserving healthy ecosystems and ensuring the long-term persistence of the biodiversity upon which life depends.

Renewable energy can be defined as energy obtained from a naturally continuous flux of energy occurring in the immediate environment [33] and is also sometimes referred to as "sustainable energy" or "green energy", and non-renewable energy is called "finite supplies" or "brown energy". Unlike fossil-based energy resources, which require constant effort and exploration to make them available for use, the energy obtained through a naturally continuous flux of energy requires no human effort. When compared to non-renewable energy that has a negative environmental impact, the energy obtained from renewable energy sources (i.e., sun, wind, etc.) has been deemed compatible with sustainable development goals [33].

Solar, hydro, tidal, wind, wave, biomass, biofuels, and geothermal are all examples of renewable energy sources that have a low impact on the environment. Although they are naturally occurring energy sources, sites can have different environments and possibilities for harnessing renewable energy. Therefore, the energy delivered by their technologies is modelled based on the available natural resource (e.g., flat regions, such as Denmark, may benefit from wind power rather than hydropower). This characteristic is one of the primary barriers to the prevalent use of renewable energy, as practical energy systems must be compatible with the local environmental resource flows in a specific region. Energy storage systems, on the other hand, can help balance the variability of energy resources. There are energy storage technologies available for renewable energy applications, which will be discussed briefly in this thesis.

Renewable energy's share of global electricity production increased to nearly 28% in the first quarter of 2020, up from 26% in the first quarter of 2019. This increase came at the cost of gas and coal, representing up to 60% of the global electricity supply [34]. The Sun is one of the most prospective sources of renewable energy. There are mainly two ways of utilising solar energy. The first way is photovoltaic generation using solar cells. Photovoltaic cells do not need any moving parts to produce electricity directly from electromagnetic radiation, in this case, sunlight. The second method is solar energy generation, which utilises solar concentrators to convert direct normal irradiation (DNI) or 'beam radiation' into heat, which is then converted into electricity. This thesis focuses on the solar-thermal based energy system; thus, this section will concentrate on the background of concentrated solar power (CSP) plants. The CSP global capacity for sustainable development is shown in Figure 2.1 [35]. Over the decade, CSP has witnessed growth, and it offers promising energy options for a sustainable energy supply as they continue to spread to new markets. However, to attract additional investment, design policies will need to emphasise the value of the CSP storage [35].

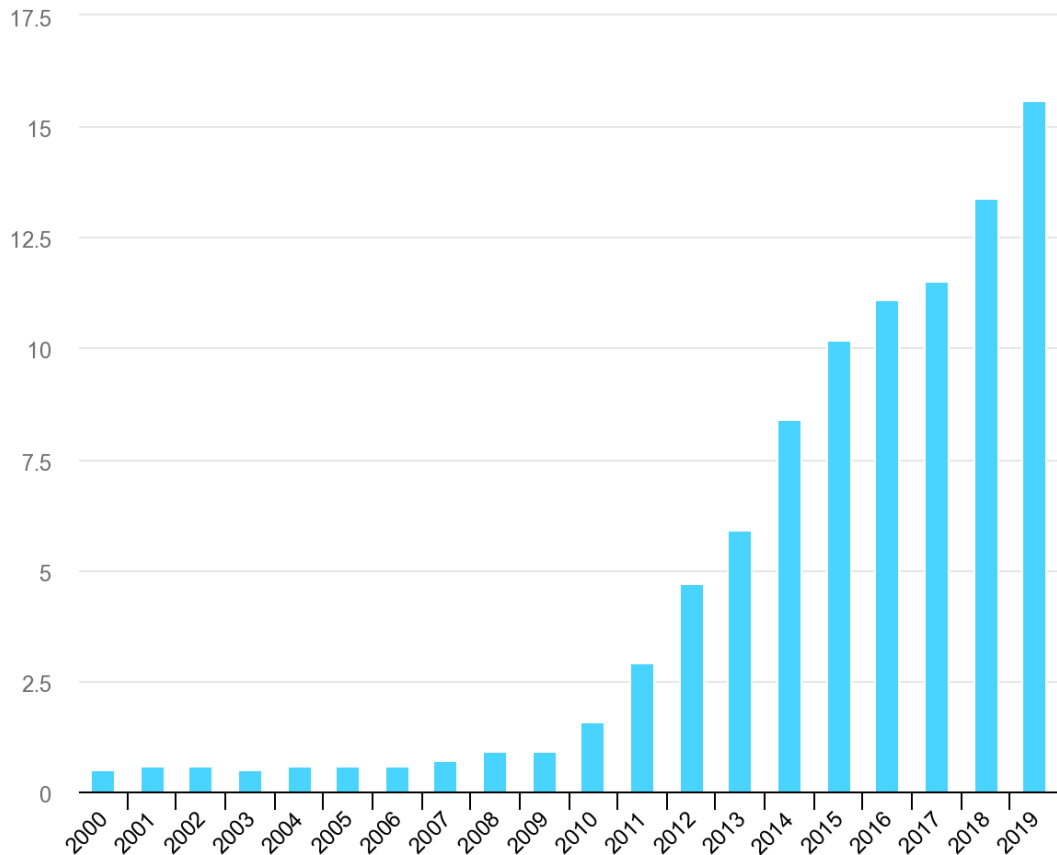


Figure 2.1: CSP global capacity (TWh)

2.2. Solar thermal concentrator types

Solar concentrator systems used to generate electricity are classified as power tower, parabolic trough, linear Fresnel, and Dish Stirling.

The power tower, parabolic trough, and line Fresnel are all technologies for Rankine or Brayton cycle-based CSP systems. The basic principle of solar thermal energy conversion to electric energy is depicted schematically in Figure 2.2.

Solar collectors are mechanical/optical devices that recuperate energy by concentrating, absorbing, and converting radiant solar energy. This energy can be stored and converted to meet thermal, electrical, or mechanical energy demands if necessary. In general, solar collectors are classified as concentrating or non-concentrating.

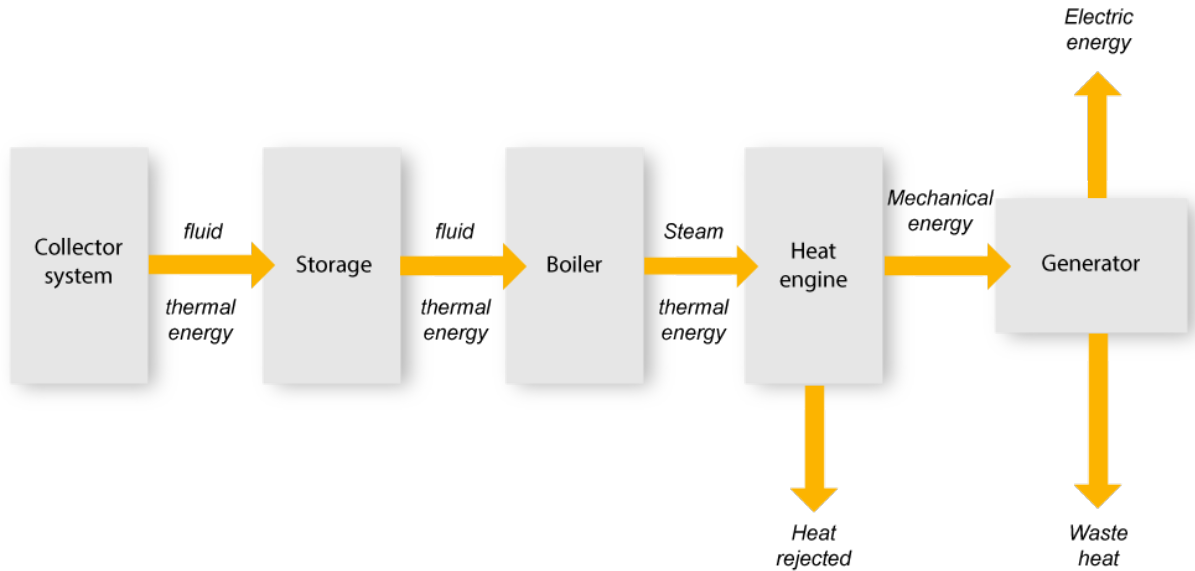


Figure 2.2: A generic CSP plant [36]

While CSP plants typically intercept and concentrate solar radiation into a small receiving area due to their concave reflecting surface, which increases the radiation, non-CSP plants intercept and absorb solar radiation using the same area made of flat mirrors.

2.2.1. Power Tower

The power tower, which is known to have a central receiver, was first proposed by Russian scientists in the mid-1950s in response to the 1973 oil crisis [37]. Typically, a large field of flat mirror heliostats is used to focus and concentrate sunlight onto a central receiver mounted at the top of a power tower. The diagram in Figure 2.3 depicts a power tower used to generate electricity. Due to the concentrated beam's high energy, any substance that passes through a heat exchanger at the top of the tower will melt or vaporise. Typically, molten salt or oil is used as a heat transfer fluid to produce steam in steam generators for conventional electricity generation by steam turbines. Additionally, heat transfer fluids such as oil or molten salt have been used as heat transfer fluids in thermal energy storage systems. The addition of thermal storage to the power tower system enables continuous electricity dispatch during cloudy weather or at night.

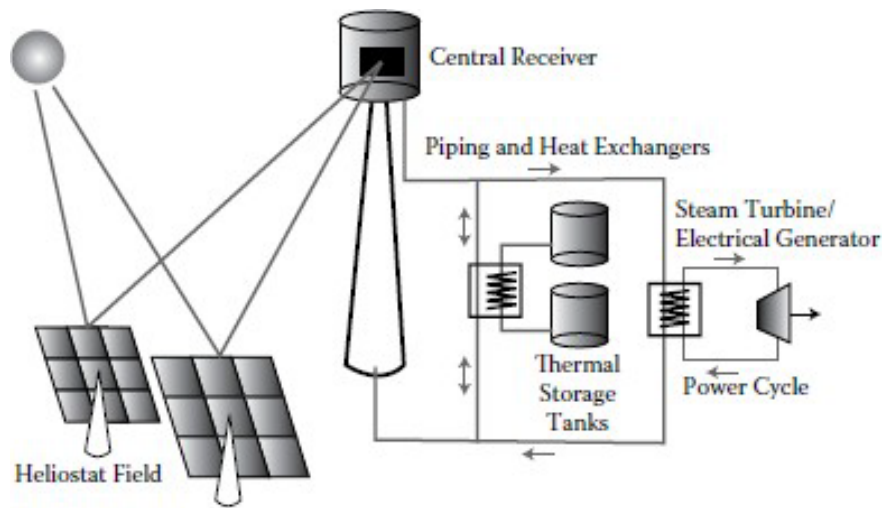


Figure 2.3: Power tower technology for generating electricity

The annual capacity factor of the majority of solar technologies without storage is 25%; however, when thermal storage is added, power towers can achieve annual capacity factors of up to 60% and as high as 80% during the summer.

2.2.2. Dish/Stirling

Dish/Stirling technology utilises a parabolic dish to focus sunlight on a thermal receiver located at the dish's focal point. Heat is received by a Stirling engine, the operation of which is based on the expansion and compression of a gaseous working fluid at various temperatures. The heated gas is used to move pistons and generate mechanical energy to power a generator. The dish/Stirling system is schematically depicted in Figure 2.4.

2.2.3. Parabolic Trough

The most mature CSP technology is a parabolic trough power plant. This is made of parabolic-cylindrical collectors made of reflective materials that focus solar rays on a receiver tube located in the focal line. The receiver tube absorbs the concentrated solar energy and heats the fluid inside. After being heated inside the absorber pipe, the heated fluid is pumped to the steam generator, which powers the steam turbine. To maximise efficiency, the troughs can track the Sun around a single axis, which is typically oriented north to south. The parabolic trough is schematically depicted in Figure 2.5.

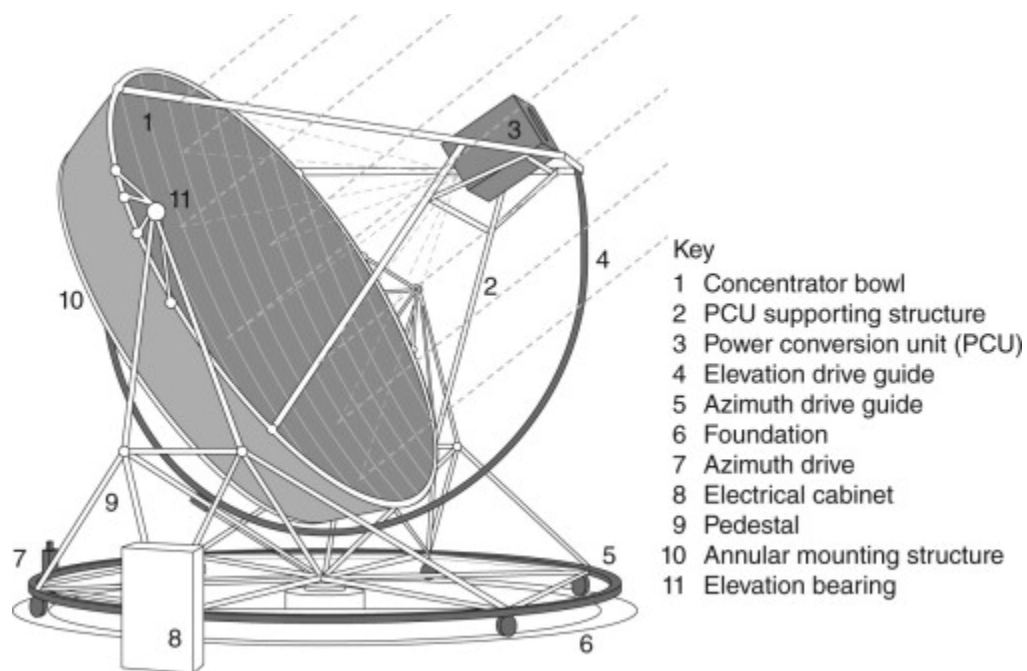


Figure 2.4: Dish-Stirling System [38]

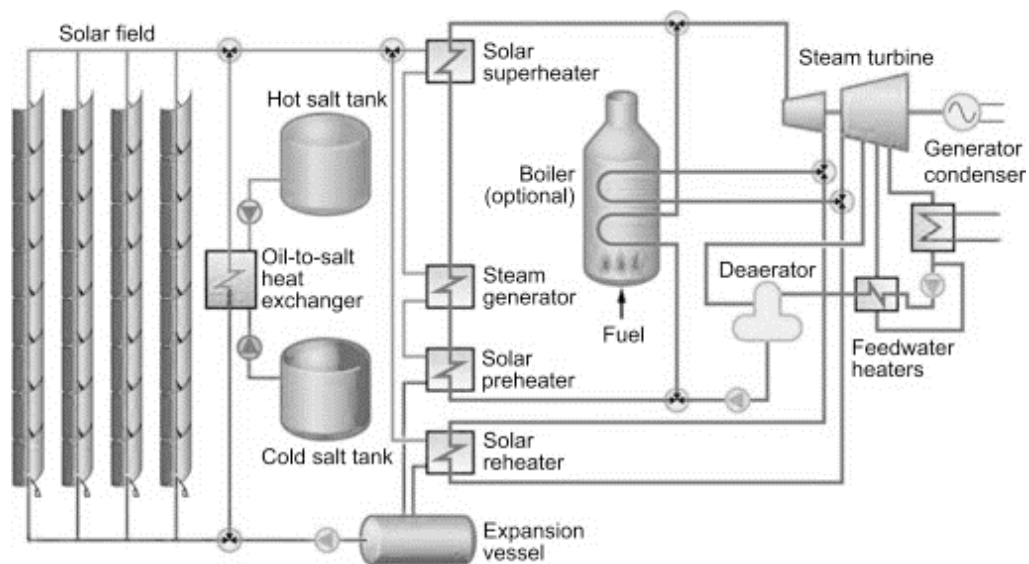


Figure 2.5: Simplified schematic of a parabolic trough power plant [39]

2.2.4. Linear Fresnel Reflector

The linear Fresnel reflectors are a series of long, narrow, shallow, slightly curved (or flat) mirrors used to focus beam radiation onto one or more linear absorbers several metres above the reflecting mirrors. These long, narrow, slightly curved (or flat) mirrors can be rotated around their long axes, which are oriented north-south to track the Sun. The linear Fresnel reflector, in general, aims to reduce overall system costs by allowing the aperture size of each absorbing element to be unconstrained by wind loads [40]. Figure 2.6 shows a diagram of the linear Fresnel reflector system. Due to the large curvature radius of the facets, it is possible to use inexpensive, flat glass that can be curved elastically. The stationary absorber above the reflecting mirror obviates the need for flexible fluid joints. The most common heat transfer fluid is synthetic oil heated to approximately 390 °C, which can also be used for thermal storage. Appropriate focusing of mirrors at different times of the day allow for a denser packing of mirrors on a limited amount of available land. However, because of the mirrors' flat arrangement, inherent additional optical (cosine) losses reduce annual optical output by between 20% and 30% when compared to the parabolic trough design. To make linear Fresnel systems a viable option, this loss of optical performance must be offset by lower investment costs.

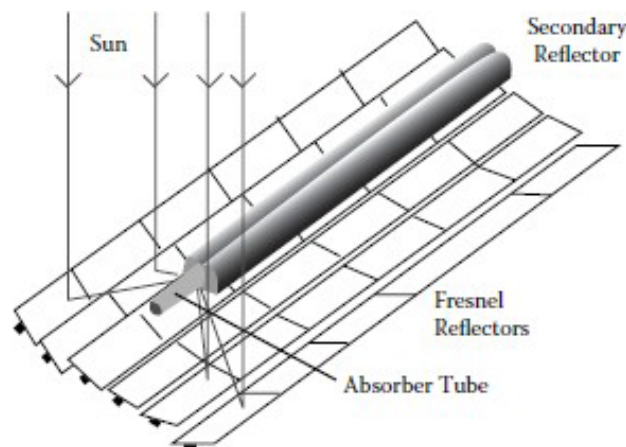


Figure 2.6: A linear Fresnel reflector system with a secondary reflector on top of the receiver [37]

The parabolic trough's higher optical efficiency is due to its rigid, rotational collector structure. While the entire concentrator structure for the parabolic trough system tracks the Sun, in the case of the Fresnel reflectors, only the small mirror facets are rotated. Since bearings, drives, and supporting structures should withstand lower loads, they are constructed leanly. Wind loads on the mirrors are extremely low due to the arrangement of the facets with small aperture width in a single horizontal plane near the ground. Because the optical concentrator movement is independent of the receiver tube in a linear Fresnel system, long rows with straight receiver tubes are easily realised.

2.2.5. The overall concept of CSP plant technologies

For the long operational hours of a solar plant, there is a need to use an energy storage system since sunlight is not available to meet energy demands during the night. Integrating energy storage systems with CSP technologies enables solar power plants to operate for longer periods of time. On cloudy days, energy production can be ensured using short-term thermal storage systems with a 1-hour capacity. Despite their obvious advantages, most of the demonstrational and commercial solar power plants appeared to lack substantial thermal storage, relying on thermal inertia. Due to economic constraints, battery storage technologies have not been investigated for large-scale power plant applications. In Table 2.1, the four major CSP technologies are compared, considering the possibility of storage integration, its benefits, and drawbacks.

The efficiency of power conversion in a heat engine is theoretically limited by Carnot's efficiency and is proportional to the energy quality, and thus temperature, of the thermal energy supply. Solar energy-based electricity generation systems require collectors to provide the required high-quality thermal energy. When the collector output temperature rises, energy losses (i.e., convective, reflection, heat transfer, glazing absorption, and thermal radiation) occur. These occur as a result of the collector's interaction with the local environment. While efficiency increases as the temperature of the hot reservoir increases, high temperatures can reduce the efficiency of solar collectors. To determine the power plant's optimal operating point, a trade-off analysis must be conducted.

Table 2.1: The comparison of the different CSP technologies

CSP Technology	Possibility of storage integration	Benefits	Drawbacks
Parabolic Trough	Possible	Installation costs are relatively low.	Inadequate thermodynamic efficiency because of the low operating temperature
		Mature technology, hence, there is significant experimental feedback	Area occupied is relatively large
Linear Fresnel reflectors	Possible	Installation costs are relatively low.	Inadequate thermodynamic efficiency because of the low operating temperature
Solar Tower	A distinct possibility with low storage cost	Increased thermodynamic efficiency because of the high operating temperature	Installation costs are relatively high, and there is also a significant heat loss
			Area occupied is large
Dish Stirling	Difficult	Area occupied is relatively small	Cost of installation is relatively high
		Increased thermodynamic efficiency because of the high operating temperature	Insufficient experimental feedback

Figure 2.7 illustrates the efficiency of the combined absorber and heat engine for various CSP technologies, which suggests that the global plant efficiency increases as the concentration ratio is increased. This increase results in a trade-off between the efficiencies of the absorber and heat engine, leading to the optimal operating temperatures. Figure 2.8 shows the efficiency for four different collectors for a typical summer day in Daggett, California.

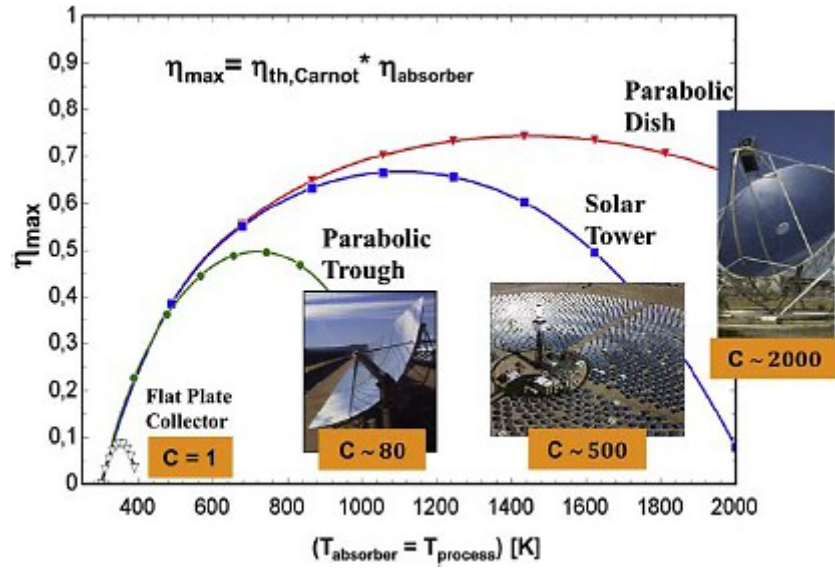


Figure 2.7: Thermal efficiency for different collector technologies [41]

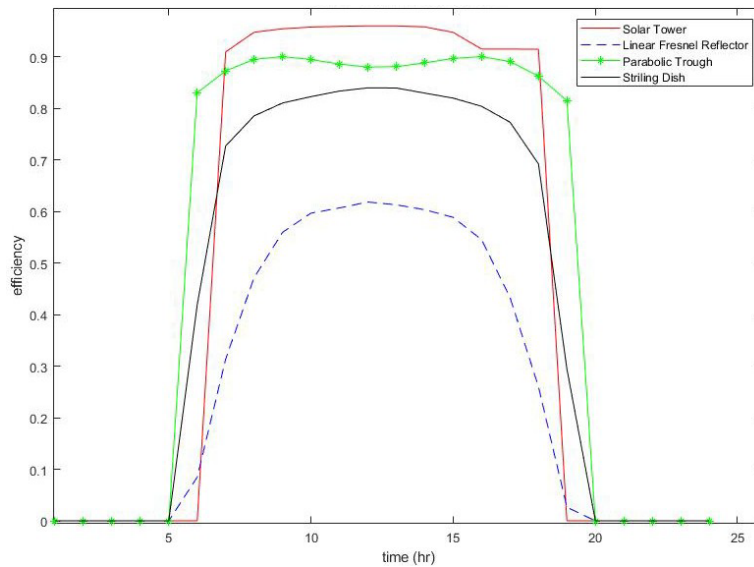


Figure 2.8: Solar collector efficiency for a typical summer day

While there are numerous technical alternatives for CSP, not all of them have reached commercial maturity. Some of them are merely concepts that are being developed in laboratories, through research and development, or through demonstration.

2.3. Organic Rankine Cycle

In comparison to the steam Rankine cycle's (SRC), the Kalina cycle's complex system structure with a superheating device, the Tilateral flash cycle's difficult two-phase expansion, the expensive material yet low efficiency thermoelectric generator, and the supercritical CO₂ cycle's high operating pressures – the organic Rankine cycle (ORC) has the advantages of having a simplistic structure. These are also easy to maintain, have high reliability, and low cost. The ORC technology has been demonstrated to be amongst other effective solution for utilising waste heat for reliably meeting electricity demand via distributed power generation. To put it differently, the ORC technology can take the energy that would have been wasted and convert it to useful energy. This energy can be in the range of a few kilowatts to Megawatts. While the ORC is like the SRC, it utilises organic compounds (i.e., refrigerants or hydrocarbons) that boil at a lower pressure and temperature than water. This enables the ORC to generate power from low to medium temperatures of around 60 °C up to 350 °C. When combined with renewables, the ORC offers unique advantages over the SRC, including low capital and maintenance costs, small size, simple structure, high reliability, and low environmental impact. As a result, the ORC technology has been rapidly deployed across the globe in recent years and has seen remarkable advancements as a result of extensive academic research [42].

The ORC is similar to the SRC in that it utilises all of the SRC's primary components, including the expansion device, pump, evaporator, and the condenser, with the exception that water is replaced by an organic compound. Indeed, the ORC technology is quite mature, possibly as old as the SRC. The first patent for an engine that uses ether as the working fluid dates all the way back to 1826 [43]. During the first half of the twentieth century, significant effort was made to primarily integrate solar and geothermal energy with the ORC technology for power generation [44-47]. During the 1970s and 1980s, the oil crisis and environmental concerns accelerated the development of ORC systems in several areas, including novel configurations such as cascaded cycles [48], alternative organic fluids such as zeotropic mixtures [49], and novel applications such as the use of ORC in vehicles [50]. This trend has continued at a rapid pace to the present day.

2.3.1. ORC configurations

The ORC layout is significantly simpler than the SRC layout because there is no requirement to connect a water-steam drum to the boiler, and a single heat exchanger can handle all three phases of the heating process, namely preheating, vaporisation, and superheating [51]. Figure 2.9 depicts a simplified organic Rankine cycle schematically. The following diagram depicts the flow process between the ORC components:

- 1–2: As the organic vapour fluid expands to lower pressure, its thermal energy is converted to mechanical energy by the expander.
- 2–3: Using a cooling medium, the vapour is then condensed in the condenser.
- 3–4: A pump is used to pressurise the low-pressure organic fluid.
- 4–1: With a low-grade waste heat source in use, the organic fluid is vaporized in the evaporator, and a new cycle begins.

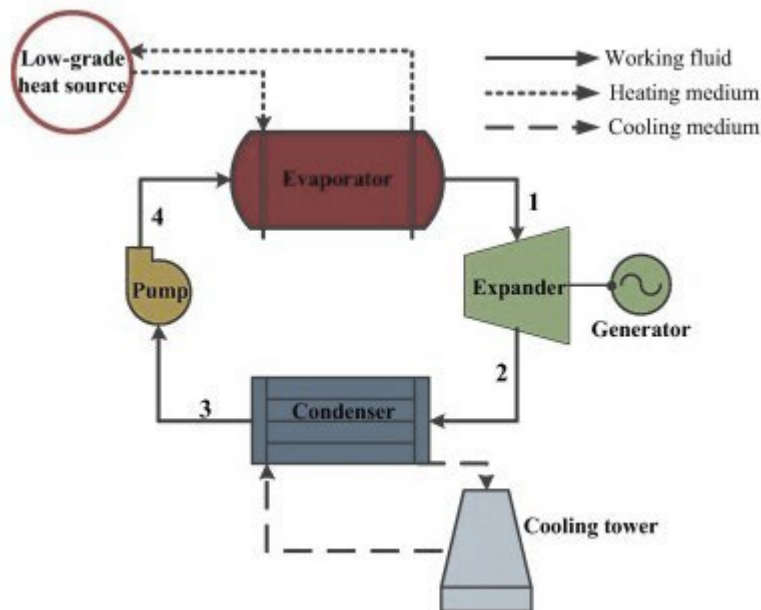


Figure 2.9: The schematic layout of a simple ORC system

Figure 2.10 shows the temperature-entropy diagram of the organic Rankine cycle.

If the temperature at the turbine exit is significantly higher than the temperature at the condenser inlet, the thermal efficiency of the simple ORC could be increased by including a recuperator between both the turbine exit and condenser inlet [52, 53]. The recuperator can be used to pre-heat the working fluid prior to its entry into the evaporator using the residual heat generated by the turbine. In other words, the average temperature of heat transfer to the cycle is greater than the average temperature of heat transfer to the environment (Figure 2.11 shows the recuperated ORC), while the average temperature of heat transfer to the environment is lower, resulting in a higher cycle thermal efficiency [54].

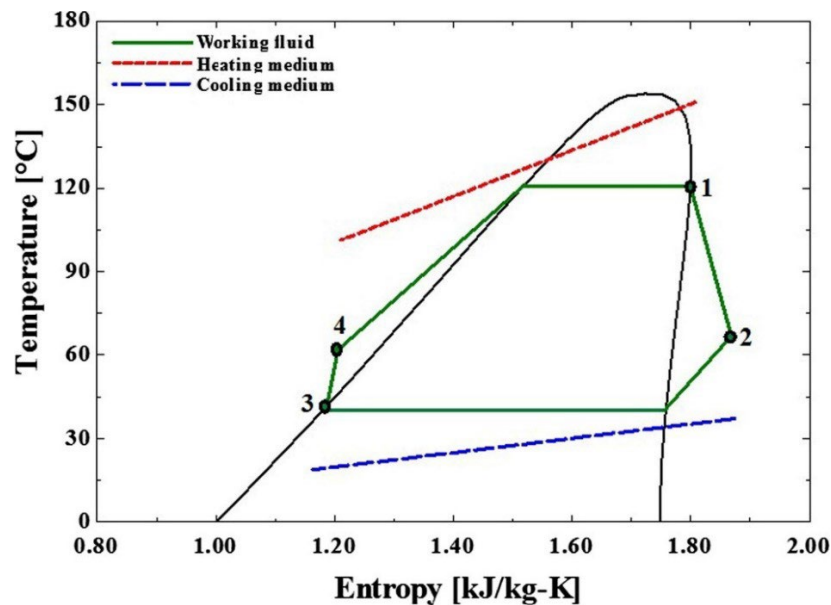


Figure 2.10: Temperature-entropy of the simple ORC

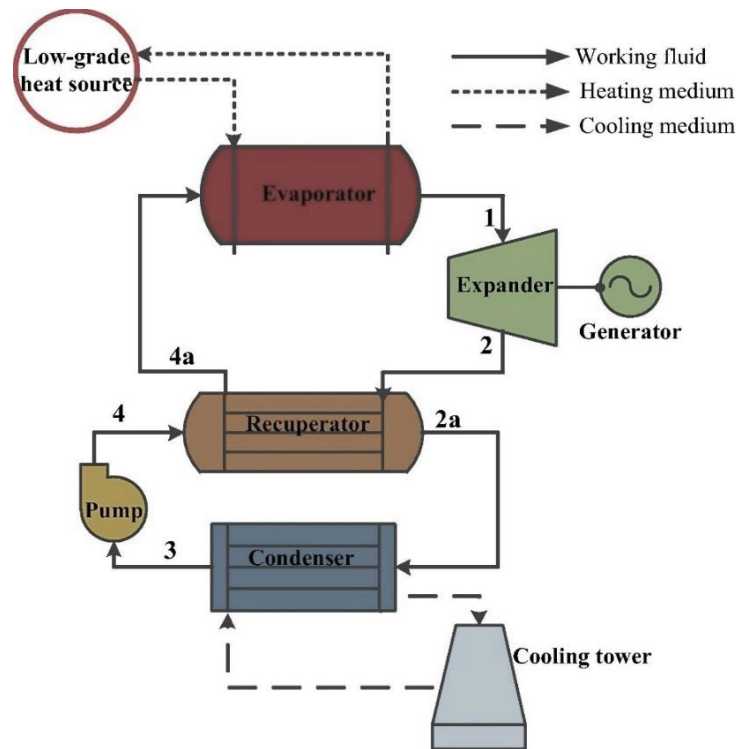


Figure 2.11: The schematic layout of the recuperated ORC

Figure 2.12 illustrates the temperature-entropy diagram for the recuperated ORC. Comparing Figure 2.10 with 2.12 demonstrates the advantage of using the recuperator, but at a higher initial capital cost and complexity.

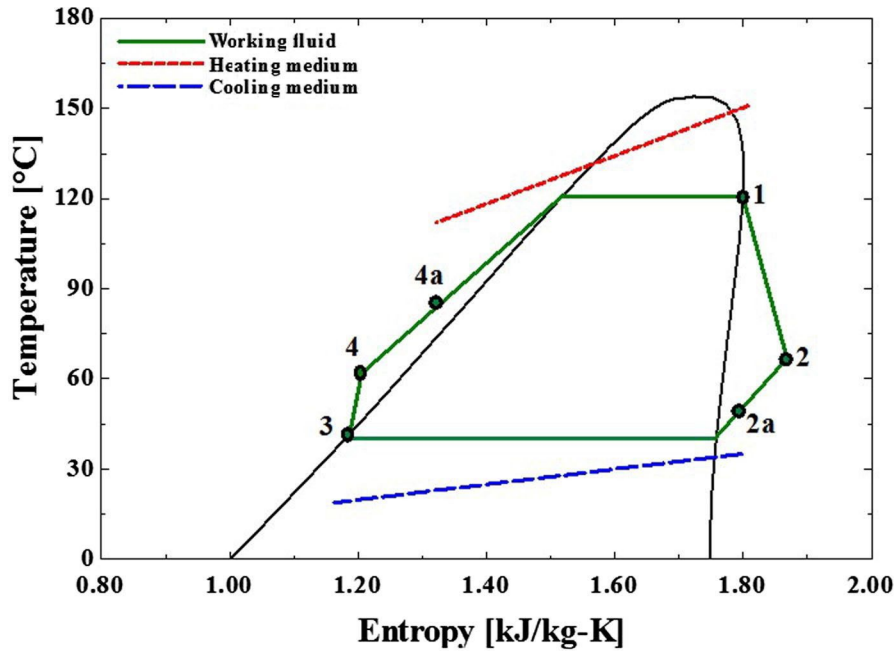


Figure 2.12: Temperature-entropy diagram of the recuperated ORC [42]

2.3.2. Selection of Organic working fluid

The selection of a working fluid is critical in ORC systems. The thermophysical properties of working fluids have a significant impact on the system's efficiency, component size, economic viability, safety, expander performance, system stability, and environmental concerns [55-57]. The choice of a working fluid is critical for achieving high cycle thermal efficiencies and optimising heat extraction from the hot stream. Organic fluids are frequently dense compounds with high molecular weights and low boiling and pressure points. They are classified as dry, isentropic, or wet fluids according to their slope of the saturation vapour diagram, which is positive, zero, or negative, as illustrated in Figure. 2.13. Due to the ORC's lower operating temperatures, dry and isentropic fluids are preferable to wet fluids such as water due to their superheated state following expansion. This eliminates the need for superheating equipment and the potential for damage caused by liquid droplets impinging on fluid path components. These characteristics allow for significant reductions in evaporator size and expander maintenance, lowering the system's capital and operating costs.

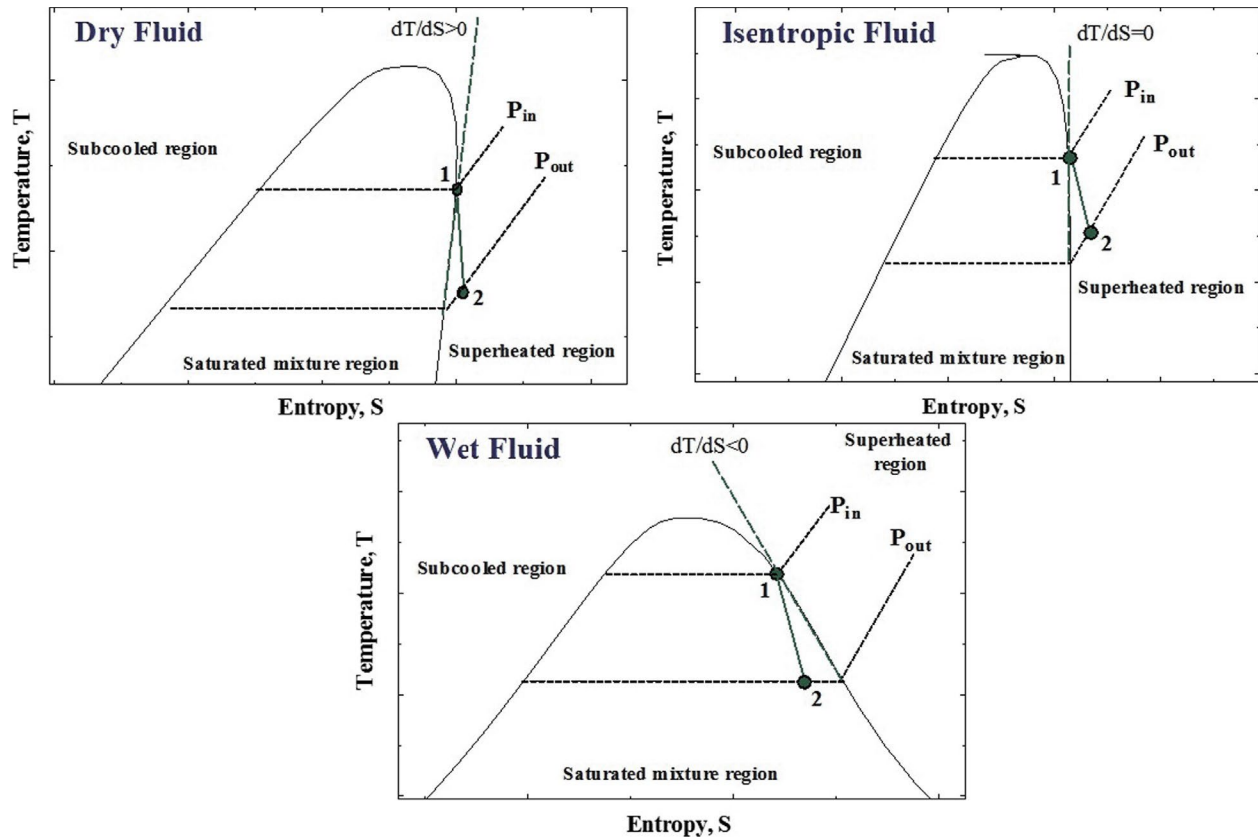


Figure 2.13: Temperature-entropy diagram of dry, isentropic, and wet fluids

The following sub-sections discuss additional critical thermophysical properties to consider when selecting an organic working fluid.

- **Latent heat of vapourisation:** Organic fluids with a low latent heat of vapourisation are preferred for use in ORC with low-grade waste heat sources as this enables heat transfer to occur primarily at the variable temperature in the evaporator [57]. As a result, the temperature profile of the working fluid in the evaporator more closely matches that of the heat source, thereby reducing irreversibility in the heat exchanger [58].
- **Thermal stability:** Organic fluids may decompose at elevated temperatures and pressures, resulting in corrosion and ignition. As a result, they must maintain thermal stability when exposed to high temperatures.

- **Specific volume:** Organic fluids have several significant advantages, one of which is their low specific volume (high vapour density). Low specific volume fluids result in lower volume flow rates, which translates into the smaller heat exchanger and expander sizes, significantly reducing size and cost. The vapour specific volume of several common organic fluids is shown in Figure 2.14 in comparison to water, emphasising the benefit of organic fluids.

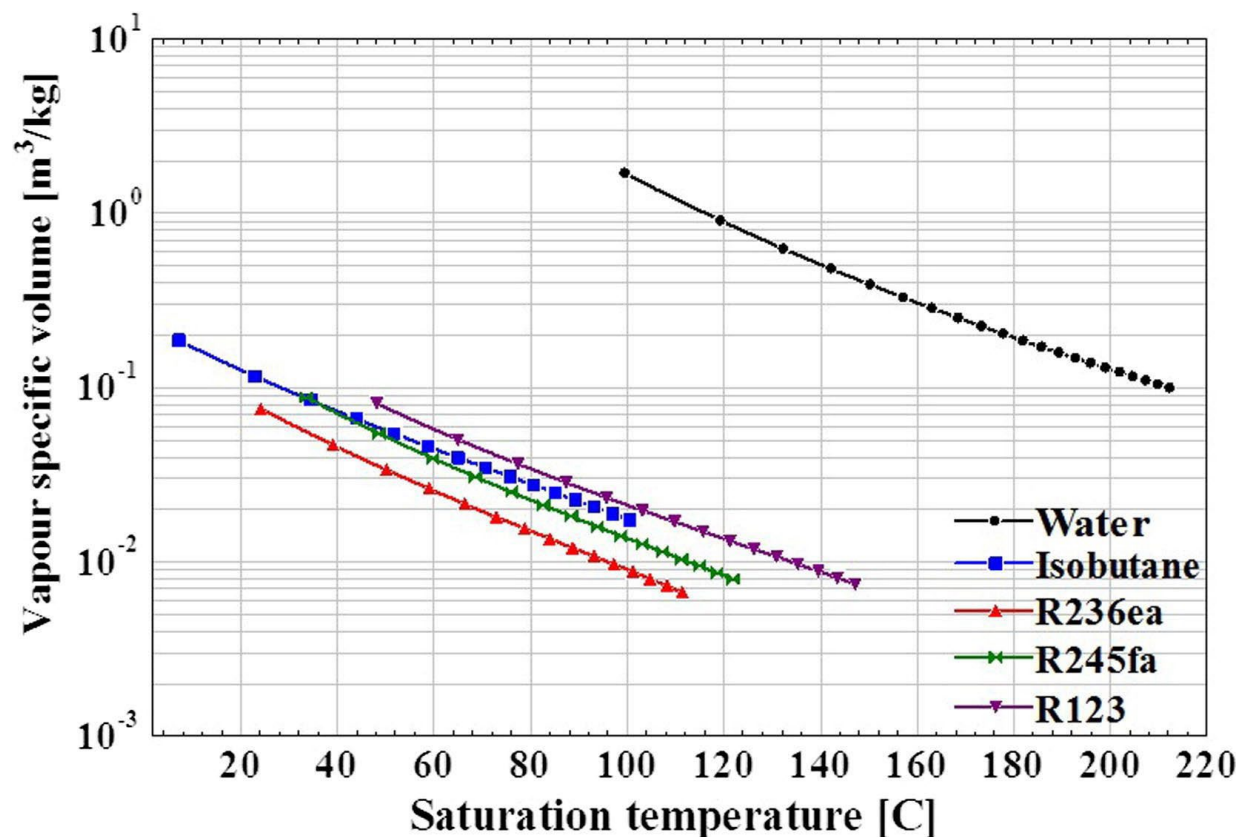


Figure 2.14: Saturated vapour specific volume plotted against saturated temperature for water as well as some common refrigerants

- **Critical temperature:** A high-efficiency cycle configuration is only possible with fluids whose critical temperature is close to the maximum temperature of the heat source [59].

Safety, environmental impacts, material compatibility, molecular weight, viscosity, cost, and availability are also critical properties to consider when selecting an organic working fluid. However, no organic fluid can meet all the above requirements simultaneously, and there is always a trade-off between various criteria based on their relative importance for each specific application.

2.4. Energy storage technologies

As previously stated, one of the difficulties confronting solar energy systems is their intermittent power supply because of inclement weather. Renewable energy systems can mitigate this challenge by utilising energy storage systems. This sub-section would briefly present an overview of various storage technologies and their capacity to balance the sporadic nature of renewable energy resources. Energy storage technologies can be classified into four main storage types, namely, chemical storage, electrical storage, mechanical storage, and thermal storage systems.

2.4.1. Chemical energy storage system

Chemical energy storage systems are by far the most prevalent type of energy storage. The lithium-ion (Li-ion), lead-acid, nickel-metal hydride (Ni-MH), nickel-cadmium (Ni-Cd), sodium sulphur (NaS), sodium-nickel chloride (ZEBRA), vanadium redox (VRB), and zinc bromide (ZnBr) are examples of the battery energy storage systems. They have an efficiency ranging from 60 to 90% and respond to changes to the electrical load. Additionally, NaS, ZEBRA, VRB and ZnBr are commonly referred to as high-energy batteries because of their high storage duration timescale and longer life span [60].

2.4.2. Electrical energy storage system

Capacitor energy storage, supercapacitor energy storage, and superconducting magnetic energy storage are all examples of electrical energy storage systems. Capacitors have the capability, at fast rates, directly store electrical energy. Compared to battery energy storage systems, they have significantly higher charge/discharge cycles [61]. The major shortcoming of this storage system is its low energy density. The super-capacitor energy storage system in terms of energy density and capacitance has better electrical properties than the capacitor storage. Their relatively larger surface area makes its electrical

properties thousands of times higher than the ordinary capacitor storage system. Compared to conventional capacitor storage, the super-capacitor energy storage system has higher power and energy density; its density is still lower than that of the lead-battery system. Therefore, in general, capacitors have shorter timescales, short discharge, and high self-discharge loss of around 20 - 40% per day, and these shortcomings limit their usage to electrical applications.

Superconducting magnetic energy storage systems accumulate energy in the form of magnetic fields and convert it to electrical energy only when it is required. Additionally, they have a high efficiency of approximately 98 percent and a rapid switching response [60]. Some of the major challenges associated with this energy storage technology are their high cost, short discharge time and the environmental issues of developing a strong magnetic field.

2.4.3. Mechanical storage system

Mechanical storage systems include flywheel energy storage, pumped-hydro storage, and compressed air energy storage systems.

The flywheel energy storage system is an electromechanical system that can store electrical energy as kinetic energy. It is typically made up of a cylinder that revolves on magnetic bearings connected to an electrical machine [60, 61]. This machine behaves like a generator when energy is discharging, and during the charging process, it operates as a motor.

Compressed air is used to store energy in dedicated underground chambers [62]. When demanded, the energy that is stored is later discharged through a conversion process that involves combustion. The heat developed during air compression (i.e., when the system is charged) is usually released to the atmosphere during discharge. The storage system has an efficiency of 85% and a life span ranging between 20 and 40 years [61].

The pumped-hydro storage is low-cost, well-developed and widely used for large-scale energy storage applications in power systems [63]. This storage is typically made up of a double interconnected reservoir, each having different heights, a pumping mechanism to store water to the upper reservoir and a turbine that produces electricity when water is let

out into the lower reservoir. This storage system has an efficiency of 70-80% and a life span ranging between 40 – 60 years [61, 62].

2.4.4. Thermal storage system

Thermal energy storage systems make use of materials that can be kept at elevated or lowered temperatures in specially designed insulators [63]. This storage system could be categorised into high temperature and low-temperature storage systems. However, these media storage systems are largely dependent on their operating temperature at room temperature. Thermal energy systems having a temperature of -18 °C are used for industrial cooling application [61]; those with temperatures ranging from 0 to 12 °C and 25 – 50 °C are for achieving cooling and heating, respectively. Thermal energy storage systems with temperatures greater than 175 °C are used for heat storage applications.

- ***Low-temperature thermal energy storage systems:*** This consist of two types - aquiferous (ATES) and cryogenic (CES). The ATES is frequently associated with the refrigeration process of cooling or ice water. When users require cooling, this process may be advantageous [60]. The CES is a term that refers to the process of boiling cryogen (liquid nitrogen) with ambient heat. The cryogen is heated and then used to generate electricity via cryogenic heat engine configurations. The CES system has a 20–40-year life expectancy, a self-discharge loss of 0.5–1% per day, and a round-trip efficiency of 40–50% [60].
- ***High-temperature thermal energy storage:*** This type of plant stores heat energy in two molten salt tanks. Apart from molten salt, other materials suitable for high-temperature TES include concrete, phase change materials (PCMs), saturated steam, and ultrapure graphite [60]. The high-temperature TES has a life expectancy of five to fifteen years and self-discharge losses of between 0.05 and 1% per day. The Solana Generating Station in the United States is an example of a solar thermal power plant. It has a capacity of 280 MW and stores energy in molten salt for six hours [64]. Pumped heat storage is another type of high-temperature TES that is still in development. It is expected to have a round-trip efficiency of 75–80% [60, 63].

Additionally, its design enables more scalable and cost-effective storage configurations than the pumped hydro system. Additionally, it will have a lower environmental impact than pumped hydro technology.

2.5. Heat pipe

Following many years of intensive exploration into modern thermal management systems, heat pipes (HPs) are used as a passive capillary-driven heat transfer device capable of transporting significant amounts of energy with minimal loss [65]. Due to the higher effective thermal conductivities of heat pipe, they can transfer heat loads of several degrees; having a thermal conductivity exceeding that of any known metal. Gaugler [66], of General Motors Corporation in 1944 was the first to patent a lightweight "heat transfer device" which is basically the present-day heat pipe. The heat pipe concept was then forgotten for two decades until it was rediscovered in 1962 [67] by Trefethen and then by Wyatt in 1963 in form of a patent application in connection with the space programme. At the Los Alamos Scientific Laboratory in 1963, independent work of Grover et al. [68] inverted the concept and built prototypes. Ever since, the impetus was provided for heat pipes, which has caused the steady growth and popularity throughout the world for a variety of applications, spanning nearly the entire temperature range encountered in heat transfer processes. The heat pipe technology is used for thermal management in a variety of applications, including thermal control, spacecrafts (aerospace engineering), as well as cooling electronic components. Heat pipes were the first capillary two-phase flow devices, inspiring subsequent inventions, and innovative designs such as loop heat pipes (LHPs) and capillary pumped loops (CPLs). Heat pipe recovery systems presents a market which is continuously growing. The demand for alternative energy sources has led to innovations in the application of the heat pipe technology in solar storage systems.

As shown in Figure 2.15, a conventional heat pipe is a hermetically sealed tube that typically contains a wick structure and a working fluid in both the liquid and vapour phases, with the liquid saturating the wick structure. In general, the heat pipe is divided into the following sections: the evaporator region, the adiabatic region (or transport), and the condenser region.

When the tube's evaporator region is heated, the liquid evaporates, absorbing the latent heat of vaporisation in the process. As a result of the pressure gradient created in the vapour channel, the vapour flows through the adiabatic region of the tube to the cooler end (condenser region), where it condenses and rejects the absorbed latent heat.

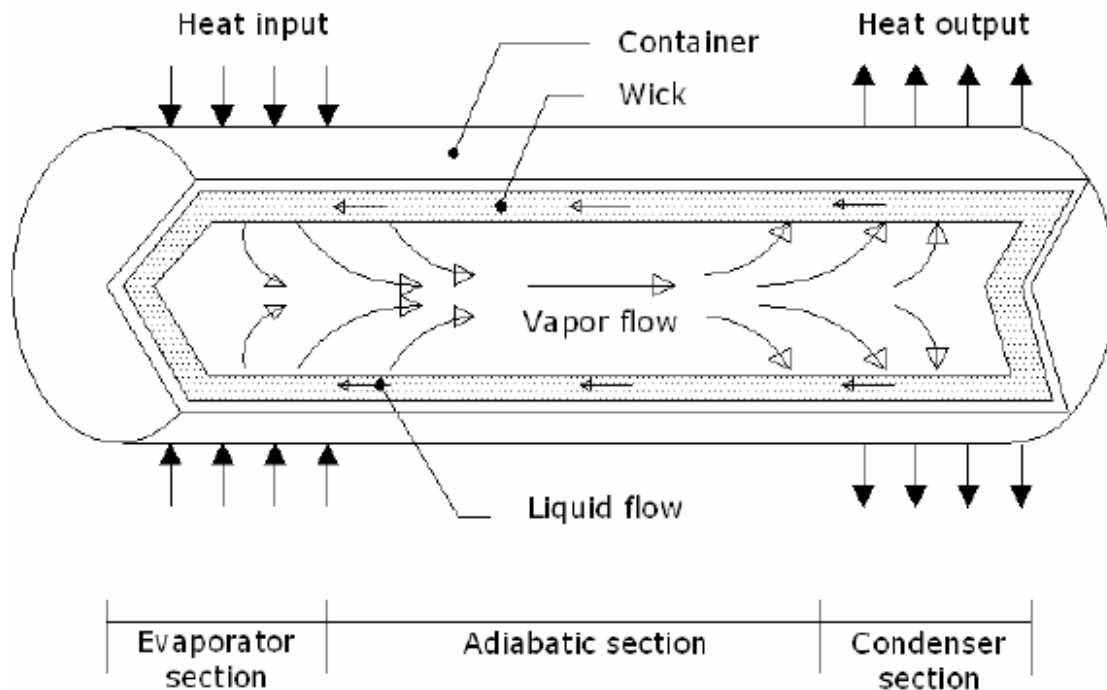


Figure 2.15: Typical operation of steady-state heat pipe

The difference in capillary radii between the evaporator and condenser ends r_{ce} and r_{cc} of the wick structure, as illustrated in Figure 2.16, results in a net pressure difference in the liquid-saturated wick. This pressure differential propels the liquid from the condenser to the evaporator section via the wick structure. The process is repeated if sufficient capillary pressure exists to allow the liquid to return to the evaporator [69].

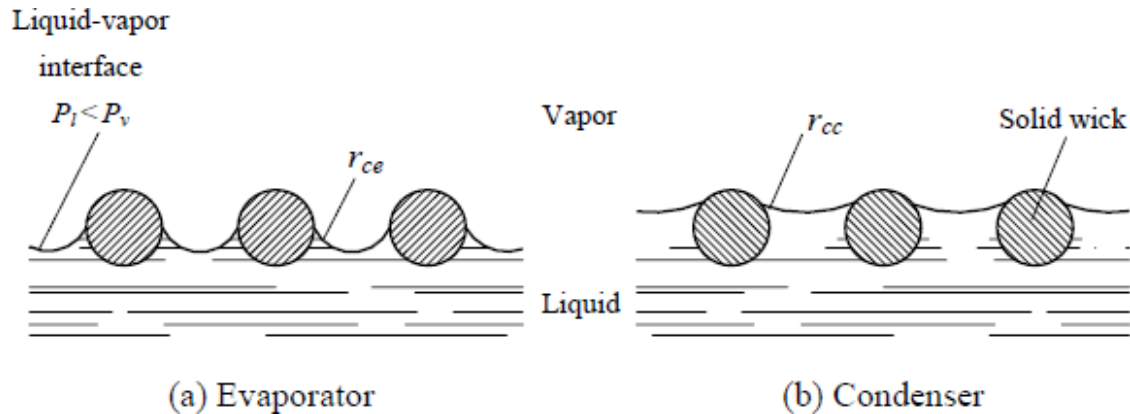


Figure 2.16: Liquid-Vapour radii curvature in the (a) evaporator and (b) condenser sections

As a result of the high latent heat of vaporisation, heat pipes are highly efficient devices for transporting large amounts of energy over moderately short distances with a small temperature difference at their surface [70].

Two-phase flow characteristics of the working fluid made it possible for heat pipes to have additional features including:

1. Providing variable heat fluxes at near-isothermal temperatures without the use of external pumping power.
2. Making a structure that is subject to isothermal temperature fluctuations.
3. Changing the rate of heat transfer between a hot and cold source located on very different surfaces.

Additionally, heat pipes can be classified according to the working fluids they contain, their geometry, and their intended applications [65]. APPENDIX A contains further literature on geometry designs, wick structures, the general design characteristics and steady-state performance of a room temperature heat pipe, operating temperature range, working fluids and heat transport limitations of a typical heat pipe.

Numerous steady-state and transient models have been developed in response to widespread interest in heat pipes. The latter part of Section 2.6 will present a review of the literature on transient heat pipe testing and modelling efforts, with a particular emphasis on low temperature heat pipes. This review summarises experimental and theoretical work on transient low temperature heat pipes and serves as a foundation for future research.

2.6. Review of related works

Numerous studies have been published on the integration of PTC and ORC, but there are few on the integration of LFR with all RC ORC to generate power. This section discusses various research projects that have been conducted to investigate and improve the performance of solar concentrators, ORCs, and various working fluids. These solar collector systems and ORC for multiple applications are then reviewed and briefly discussed.

In a numerical simulation study of the linear Fresnel reflector system used to generate steam for a power plant, Ghodbane et al. (2019) obtained optical and thermal efficiencies of 53.7 percent and 37.5 percent, respectively [71]. The authors reported that the steam power plant could generate more than 2000 MWh of electricity annually, encouraging investment in desert areas with abundant solar energy. Ghodbane et al., [72] examined the use of distilled water, system stability, and thermophysical analysis to improve the LFR system's performance. They discovered that as the volume fractions of the nanofluids are increased, their thermal conductivity increased as well. Additionally, they recorded a system efficiency of 33.81 percent when using nanofluid. Said et al., [73] demonstrated a direct correlation between the concentration of reflective mirrors and optical performance by experimentally examining the LFR. They reported that optical efficiency increases relative to the total number of reflective mirrors and that the collector performed optimally at 42.65 percent with 11 mirrors in their case. Additionally, a study reported by Barbón et al., (2019) on the effect of longitudinal tilt angles on LFR performance established that the energy absorbed by the LFR system, and the associated primary cost are significant and positively related to the longitudinal tilt angle

increase [74]. Bayón-Cueli et al.,(2020) [75] demonstrated that their 5-step method for determining the optimal geometrical distribution and parameters for a small-scale LFR on flat roofs for urban buildings could extract the most energy output from the LFR system. Another study by Bellos and Tzivanidis (2018) [76] presented an analytical expression for an LFR's incident angle modifiers. They concluded that a geometric analysis-based equation produced reliable data with mean deviations of up to 5%.

Additionally, their analytical model could be used to quickly calculate the LFR's optical performance. Bellos et al., (2018) [77] optimised the secondary concentrator using Bezier polynomial parametrization and reported an increase in the optical and thermal performance by 20% and 30%, respectively, for the LFR system. Combined heating and power and combined cooling, heating and power systems are other way solar applications are used. A CHP system coupled with PTC is proposed by Marefati et al.,(2019) [78] for Tehran weather conditions. Their hybrid system, with the PTC producing a fraction of the thermal load, had electrical and overall exergy efficiencies of 37.68 percent and 71.29 percent, respectively.

Zamzamian et al. (2014) highlighted in their experimental study [79] that the major challenges for commercialising solar thermal systems are simplicity, productivity and cost. To overcome these challenges, Bijarniya et al. (2016), in a CSP technology review [80], pointed out that solar thermal systems can be combined with other thermal cycles. The advantages of the ORC include low implementation and maintenance costs [81], the ability to use various working fluids, the availability of a plethora of inlet temperatures and the usage of ORC as distributed generation systems have recently attracted the attention of researchers [82, 83]. The working fluid and temperature range selected for an ORC system are critical to the system's overall performance [84]. Thus far, there have been efforts to improve and optimise the efficiency of the solar thermal based ORC system, which plays a part in reducing greenhouse gas emissions. Solar parabolic trough collectors (PTCs) coupled with an Organic Rankine Cycle (ORC) was studied by Bellos et al. [85]. Al_2O_3 , CuO , TiO_2 and Cu were the four nanoparticles examined in the base fluid (Syltherm 800), and the pure thermal oil was assessed as a working fluid. It is noteworthy to highlight that the ORC system examined was a regenerative cycle, and the

four organic fluids were also tested (toluene, MDM, cyclohexane, and n-pentane). This combination led to electricity production of 167.05 kW and systems efficiency of 20.11%. The design and simulation of a small scale solar plant coupled with an ORC have been discussed in [83]. The innovation consists of solar thermal collectors with an aperture area of 73.5 m² and a small ORC that produces electric and low-temperature heat simultaneously. Using diathermic oil as the base fluid, they found out that the ORC had an average efficiency of 10%. However, they obtained an efficiency of over 50% for the solar collector in summer and down to 20% in winter. After performing a thermo-economic analysis of the system, they concluded that the system was economically feasible for most Mediterranean areas and unsatisfactory for sites in Central-Europe. Although this study evaluated for different climatic conditions, the energy and economic performance of the solar CHP system, it did not consider the environmental implications of such an integrated system. Another study by [86] investigated the implementation and performance of a combined system. This combined system consists of PTC, ORC, and ejector refrigeration. In such combined systems, the cooling and power produced depend on the intensity of the solar radiation, ejector geometrical aspects and turbine extraction ratio. It was found that the power generated, the COP, and the entrainment ratio depended on the used refrigerant. Out of all the refrigerants used, R601a had the highest values of entrainment ratio and COP. Entrainment ratio defined as the ratio of the secondary mass flow rate fluid (low pressure steam) to the mass flow rate of the primary fluid (high pressure steam). The higher entrainment ratio leads to enhanced carrying capacity of high-pressure steam and improved pumping performance. Table 2.2 below shows the thermophysical properties and environmental performance of refrigerants for an organic Rankine Cycle application [87, 88].

Table 2.2: Thermophysical properties and environmental performance of some refrigerants for an organic Rankine Cycle application

	T_{crit} (°C)	P_{crit} (MPa)	NBP (°C)	ODP	GWP₁₀₀
R245fa	154.1	3.651	14.9	0	1030
R600a	134.7	3.629	-11.7	0	3
R601a	187.2	3.378	27.83	0	~20
R1233zd(E)	166.5	3.623	19	0	4.7-7
R1234ze(Z)	150.1	3.53	9.8	~ 0	6

They concluded that the entrainment ratio increased by 13% as the ejector area ratio was decreased by 12%. The authors in [89] investigated a small scale ORC and presented the influence of key factors on system performance. These factors are the product cost rate and systems exergy efficiency performance. The effective parameters included the temperature and pressure of the turbine inlet. The results obtained such that the system reached an efficiency of 22.7%, with a cost rate of about 2.66 million dollars per year. A PRC with a linear V-Shape cavity receiver coupled with an ORC was studied by [90]. They found that with an increase in solar radiation and temperature and a decrease in the flow rate of the solar working fluid, the exergy gains and efficiency of the solar system generally improved. They reported that the lowest levelized cost of electricity and payback period of the system was € 0.0716 per kWh and 8.79 years, respectively. In an environmental and energy assessment in [91] for a small-scale ORC trigeneration system coupled with compound Parabolic collectors, the authors investigated the performance of the system while varying three class of parameters. They concluded that the life cycle assessment parameter plays a key role in selecting the system components specifications and operating conditions. They further highlighted a decrease in the environmental impact when the area of the solar field is increased. In another study in [92], the author investigated the performance of a small scale LRC-ORC hybrid system with an integrated PCM storage system. The plant is intended for residential applications and was to be built and tested. They found that the modelled ORC unit operated for more than 3100 h a year while achieving suitable power performance by producing about 5100 kWh_e per year. However, the plant demonstrated a levelized cost of electricity at 4.6 €/kWh, which, when compared to other technologies, is extremely high. The performance of a small-scale LFR system was investigated in Morocco by [93]. Nine working fluids

were tested to assess the performance of the ORC system. Results showed that the optical efficiency of the LFR changes during the year, reaching 47.51% and achieving an annual power production of 7.12 kW. They also reported that the system best performed using neopentane as the working fluid. However, their study did not include an economic assessment or systems implementation costings. A review of ORC system application for solar energy is present by Mahlia et al., [94]. This paper performed a methodical search and analysis of patent landscape on ORC systems coupled with different solar thermal collectors. They concluded that the ORC system has the potential to advance in renewables while easing reliance on fossil fuel. Their study, however, did not provide data on the performance of the system. In another study Cau and Cocco [95], the performance of medium-sized PRC and LFR based ORC systems are compared. Thermal oil is the heat transfer fluid used by these plants. They found that the LFR system led to higher electrical energy production per unit area of occupied land. In terms of the unit area of solar collector, the PTC gives a better energy production value owing to their better optical efficiency. This study does not perform a techno-economic or life cycle analysis for the technologies, neither does it provide any information on the modelling of the ORC system. In a techno-economic analysis study in [96], the author evaluates the performance of a 55 MW_e combined-cycle CSP coupled with a thermal storage system in Spain. The study used EES, SAM, TRNSYS and MATLAB to design and simulate technological implementation, capital, and operational cost. For a case design of one year, the goal was to determine the plants trade-off among conflicting factors. As the key indicators to measure the performance of the system are levelized cost of electricity (LCoE), efficiency factor and capital expenditure; the proposed combine-cycle technology had an efficiency of 0.49 and an LCoE of 196 \$/MW_e. The study was concluded by introducing two improved CSP plant schemes because of a sensitivity analysis study performed. In another study [97], a techno-economic assessment of a CSP plant driven by an ORC was evaluated. The purpose of the study was to identify the factors that contribute to the reduction of the cost per kWh_e. These factors include the selection of the appropriate of solar multiple, storage hours and working fluid. They concluded that using sensitivity analysis, they were able to test the effect of the solar multiple and storage hours on the plant. Furthermore, they opted for 8 hours of storage time and a solar multiple of 1.85

with a levelized cost of 23.95 ¢/kWh. Seven different LFR system configuration were evaluated in a comparative design-environmental and economic study in [98]. The study used the system advisor model (SAM) software to perform sensitivity analysis to optimize the thermal energy storage capacity, solar multiple of the solar field and fossil fuel backup system. Results showed that inexact system optimisation and wrong selection of plant's components led to an increase in the cost of electricity generated. Another paper on the techno-economic assessment of LFR plant has been published [99]. The study attempts to compare in selected locations, various solar radiation data sources which include diffuse irradiation, global horizontal irradiation, the monthly average daily direct normal irradiation and other meteorological parameters to visualise the feasibility of the CSP system. Using two different software PVsyst and SAM, a 50 MW LFR based CSP systems performance was investigated in terms of LCoE and total electricity generation. It was concluded that for the same 50 MW LFR system, total electricity and LCoE varied for both software: with SAM producing higher values for total electricity generation and lower LCoE.

The contributions of these existing studies are useful to understand solar thermal based ORC systems. However, from the review, most of the research did not consider the environmental and techno-economic implications for a LFR-ORC system. In this study, the concepts of life cycle assessment (LCA) and techno-economic analysis (TEA) are combined in a methodology (see Chapter 3) and applied to compare the environmental impacts and economic implications (i.e., NPV, LCoE, Payback time) for the LFR-ORC. This methodology is used to comparatively assess various renewable energy technologies with the objective to develop a decision-making framework to help identify the influence of different critical indicators on performance. The result from this study is expected to add value to the existing body of knowledge.

The literature search was also conducted in the field of heat pipes. There are three fundamental modes of heat pipe start-up identified in [100]. Figure 2.17 is an illustration of the temperature profile or the different fundamental modes, where the abscissa

represents the length of the heat pipe from the evaporator ($x = 0$) to the condenser ($x = L$).

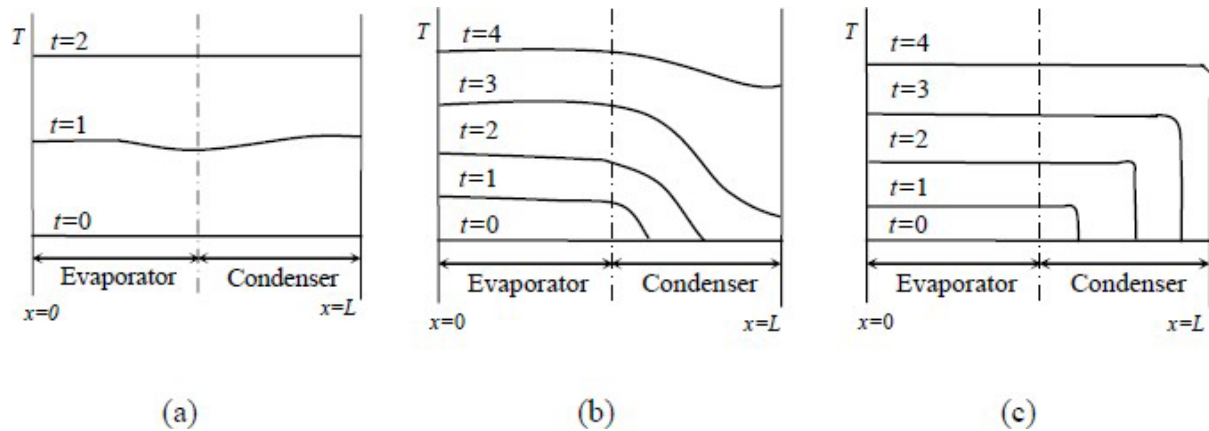


Figure 2.17: Heat pipe transient start-up profiles (a) Uniform (b) Frontal, and (c) Non-condensable gas with Frontal [100]

The temperature is represented by the ordinate axis, while the time elapsed from the start-up is indicated by the numbers labelled on the curves. These various modes of the start-up are associated with low initial vapour density at ambient temperature (Figure 2.17a) or high initial vapour density at ambient temperature (Figure 2.17b), as well as the presence of non-condensable gas (Figure 2.17c). Generally, low-temperature heat pipes exhibit uniform start-up under normal transient conditions when the vapour is in continuum flow, and the wick is saturated with liquid. Uniform start-ups can be accomplished rapidly and without failure [69].

While the working fluids such as water and ammonia would not freeze during the normal start-up, for space applications, most studies have focused on the frozen start-up temperatures between 122 - 550 K [101]

There are very few experiments on the "fully thawed" start-up of low temperature heat pipes. Two distinct approaches to the transient response of heat pipes are applied in the conclusive experiments. The first approach focused on temperature and pressure, with are thermodynamic variables, whereas the second approach focused on the transient

liquid flow characteristics into the wick structure. Without knowledge of the liquid flow dynamics, the heat transported, and subsequent dry-out conditions could be predicted using experimental data on internal heat pipe thermodynamic variables. For an 80 cm long Freon (R11) stainless-steel heat pipe, a series of tests under normal and supercritical start-up conditions were conducted in [102]. Screen layers were used to construct the capillary structure (100 and 40 mesh). The authors measured the transient vapour and wick temperature profiles, and model predictions were made for a normal start-up from an initial low temperature below the working fluid's critical temperature. The author's conclusions are as follows [102]:

- Under higher thermal loads, the wick structure was partially dried out and rewetted in the evaporator section. Temperatures in the wetted region were nearly uniform, and vapour pressure values smoothly achieved constant values in the steady-state regime.
- Heat pipes made of screened wick exhibited a quasi-steady behaviour. They rapidly adjusted to operation without experiencing dry-out for thermal loads up to the maximum capillary heat transport capacity.
- High overall resistance and dry-out of the entire liquid in the evaporator section were observed at extremely high thermal loadings, as well as with large pressure and temperature gradients.
- For low thermal loads, the heat pipe "adapts smoothly" to changes in heat input, cooling rates and reaches the steady-state operation.

Ambrose et al. [103] addressed the problems with the operating characteristics through pulsed start-up tests using a copper water heat pipe that is screen-wicked. When heat loads exceed the maximum capillary transport, it was observed that (i) full dry-out in the evaporator region would be experienced for heat pipes lacking thermal energy storage and (ii) heat pipes equipped with thermal energy storage will behave as described in [102].

The transient response of a typical 600 mm-long horizontal copper water heat pipe was investigated by [104]. A double-layered, 150 mesh copper screen was used to create the wick structure. The vapour temperature was determined along the heat pipe's centreline using a special probe comprised of a thin-walled brass tube instrumented with eleven

evenly spaced thermocouples. Additionally, the eleven evenly spaced thermocouples were affixed to the wall surface of the heat pipe. Uniform heat was applied to the heat pipe electrically and cooled convectively via a cooling water jacket. As a result of the axial conduction near the evaporator end region and condenser entrance region, uniform vapour temperatures as a function of time were observed, while wall temperatures at each heat pipe region were nearly identical. The time constants for effective power transport and water-vapour temperature during the evaporation and condensation processes were determined by the heat load input and the cooling jacket's water flow rate. In 1990, Jang [105] investigated the axial variations of a 1-m long axially grooved copper water heat pipe's wall temperature subjected to varying heat loads from the ambient to steady-state operational conditions. When the heat pipe operated at higher temperatures within its range of operation and with the same power-step increase, greater amounts of energy were transported. Evaporator dry-out was observed when there is a rapid temperature increase in at the end cap of the evaporator while the temperatures in the adiabatic and condenser sections remained constant.

The most efficient method of rewetting the evaporator was to angle the condenser section upward. Without gravitational effects, even with the power turned off, rewetting was difficult unless the heat pipe was kept at isothermal temperatures for an extended period. The effect of inclination angle on the transient response of a gravity-assisted heat pipe was investigated in [106]. The investigations were conducted as the heat input had varying cooling rates. The results indicate that the angle at which the heat pipe is inclined has a negligible effect on the transient response when the condenser is elevated. The difference between the electrical heat input (575 W) and the power transported (443W) at the steady-state condition was approximately equal to the heat loss from the evaporator to the ambient via natural convection. The effective power transported, the vapour temperature and the wall temperatures all agreed well with the predictions of the heat pipe transient analysis model.

A general method for determining the transient behaviour of a heat pipe during a heat-up by combining wall temperature measurements with simulations of internal vapour temperatures was developed in [107]. They installed a water heat pipe between two

source tanks and monitored each temperature change. One tank was initially filled with hot water, while the cold source–tank was initially filled with cold water. A thermographic camera was also used to take temperature readings at the evaporator and condenser ends. Apart from the experiment, authors in [107] created a three-dimensional model of a heat pipe using the ANSYS® software. They omitted the heat and fluid effects within the wick for the mass effects of liquid evaporation and condensation for the Hertz-Knudsen model. After adjusting the evaporation coefficients, they obtained a good agreement of temperature profiles between the simulated results and the experimental data. The simulations were then used to determine the transient effective thermal conductivity.

The effect of heat source size on the heat transfer characteristics of flat heat pipe using experimental and numerical analysis was investigated in [108] and [109] and used a thermal resistance model to investigate the thermal performance of flat heat pipes. The evaporator and condenser resistances were the most significant determinants of the cooling system's total resistance. A computational fluid dynamics (CFD) multiphase technique was used in [110] to investigate the two-phase flow and simultaneous condensation and evaporation processes inside a thermosyphon. The authors reported a high degree of agreement when CFD predicted results were compared to experimental data.

2.7. Chapter summary

This Chapter demonstrated that in the first quarter of 2020, the share of renewable energy production jumped to 28% from 26% in the first quarter of 2019. Furthermore, the chapter provided a brief background on types of solar thermal concentrators, organic Rankine cycle, the thermal energy storage system, and heat pipes. Further information on geometry designs, wick structures, the general design characteristics and steady-state performance of a room temperature heat pipe, operating temperature range, working fluids and heat transport limitations of a typical heat pipe is provided in APPENDIX A.

This chapter also reviewed some existing related research. Analysis shows that most of the published research did not consider the environmental and techno-economic implications in designing and implementing innovative LFR-ORC systems, which is critical for developing viable energy systems for remote communities. The literature search also indicates a significant gap in providing information on principles and details of CFD modelling of heat pipes operation.

Chapter 3 Methodology

This Chapter presents the framework for the comparison between mainstream and emerging solar-thermal renewable energy technologies (RETs) using an integrated environmental and techno-economic assessment methodology. Their overall sustainability potential is quantified in terms of a novel environmental and techno-economic index (ETEI), combining the Levelised Life Cycle Impact (LLCI) with the Levelised Cost of Energy (LCOE). A summary concludes the Chapter.

3.1. Integrated performance assessment framework

The evaluation of existing as well as new energy technologies creates the necessity for a framework with the inclusion of assessment levels for the different stages of technological maturity. In comparative studies, where the aim is to analyse different technologies on the same criterion, the choice of design parameters can have a substantial impact on the conclusions, which could lead to technology bias under certain conditions. The LCA, according to the ISO 14040 [111] and ISO 14044 [112], is divided in four steps: i) definition of goal and scope; ii) inventory analysis; iii) impact assessment and; iv) interpretation. Applying the environmental LCC as a first step, an environmental and techno-economic assessment (ETEA) framework is devised, combining life cycle analysis (LCA) with conventional techno-economic models to conduct an integrated sustainability performance evaluation of RETs (Figure 3.1). Additionally, an impact assessment is included in the LCC analysis to identify cost stressors. In contrast to previous studies [9, 113-116], integrating these models as one methodology allows for direct evaluation of the relationship and trade-offs between the identified processes of the RETs, assessing their overall sustainability (ETEI, formulated in Section 3.7). Electrical output and plant cost are key system design features that could be used to compare different RETs. For consistency in the estimation of ETEI, a TRL level of five (i.e. with proven feasibility in industrially relevant environment) is assumed for each RET, corresponding to a demonstration of technological feasibility with limited data availability [31].

Figure 3.1 shows the three-step sequential progression of the integrated ETEA framework – Step 1 deals with the environmental impacts of production, operation, and end-of-life decommissioning of these RETs (e.g., mass flow, emissions, energy consumption). Step 2 focuses on the techno-economic assessment of the RETs (i.e., energy output, Levelised Cost of Energy-LCOE, Net Present Value-NPV). Step 3 is the trade-off and assessment optimisation phase, which evaluates the benefits of such integration for plausible scenarios for technological improvement. Quantitation of the relevant parameters to achieve the integrated assessment are described in the following sections.

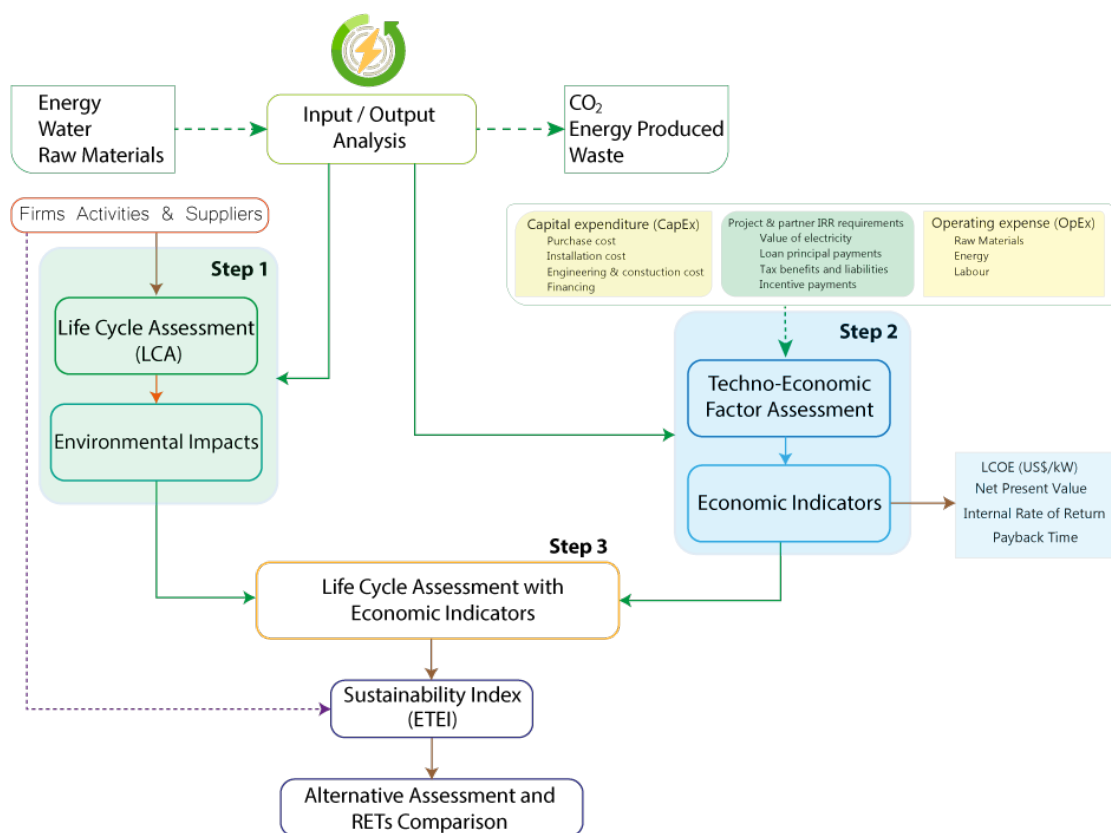


Figure 3.1: Schematic of the proposed integrated assessment framework

3.2. Life cycle assessment (LCA)

LCA is defined as an assessment tool to evaluate the inputs, outputs and potential environmental impacts of any processes or products through their complete life cycles.

3.2.1. Goal and scope definition

The goal and scope of the LCA study are critical. This step is critical for the interpretation of results and the study's overall outcomes [117]. Additionally, they must be formally specified as a required component of the LCA procedure in the ISO standard methods [118]. This section establishes the purpose of the simulated LCA model, as well as the boundaries of the products or process systems and the functional unit. It is important to define the same functional unit for the processes or products under consideration, to establish a reliable basis for comparing alternative options [117].

This study set out to evaluate and compare the environmental and economic performance of six renewable energy technologies. The scope of the assessment included the performance evaluation of the RETs. A common functional unit of 2 MWh was used in the study for evaluation of different RETs, ensuring the assessments to be comparable [30].

3.2.2. Inventory analysis

This is also referred to as a life cycle inventory (LCI). At this phase, all inputs and outputs of energy and material are collected and considered. The collected inputs and outputs are generally within the boundaries and systems previously defined [119]. The ways of gathering this data could be directly from the plant or from simulations based on a reliable process model. Additionally, this step should consider all critical factors in each process (i.e., the composition of the feedstock), the details of the technologies used in each scenario, and residue management [117].

3.2.3. Impact assessment

In this step, all the data collected in the preceding step is used to calculate the environmental impact categories. There are currently numerous impact assessment methods available, including ReCiPe Endpoint, ILCD 2011 Midpoint+, and IMPACT 2002+. Each of these methods generates a unique set of impact categories, though some categories, such as global warming potential (GWP) and greenhouse gas (GHG)

emissions, are identical. This step is also referred to as life cycle impact assessment (LCIA) [120].

3.2.4. Interpretation

The final step is to interpret the results of the inventory analysis and impact assessment to identify the most critical issues. Additionally, an uncertainty and sensitivity analysis are performed to determine the model's robustness [117]. Finally, the LCA model's output is summarised with some recommendations, depending on the type of LCA application, for example, policy formulation or product development [121].

Figure 3.2 shows the basic LCA process flows and the system boundaries for the scoped RETs. The life cycle considered in the study consists of the extraction of raw materials, manufacture as well as transportation for the construction and use phase. The models assume impacts from plant operation to be negligible.

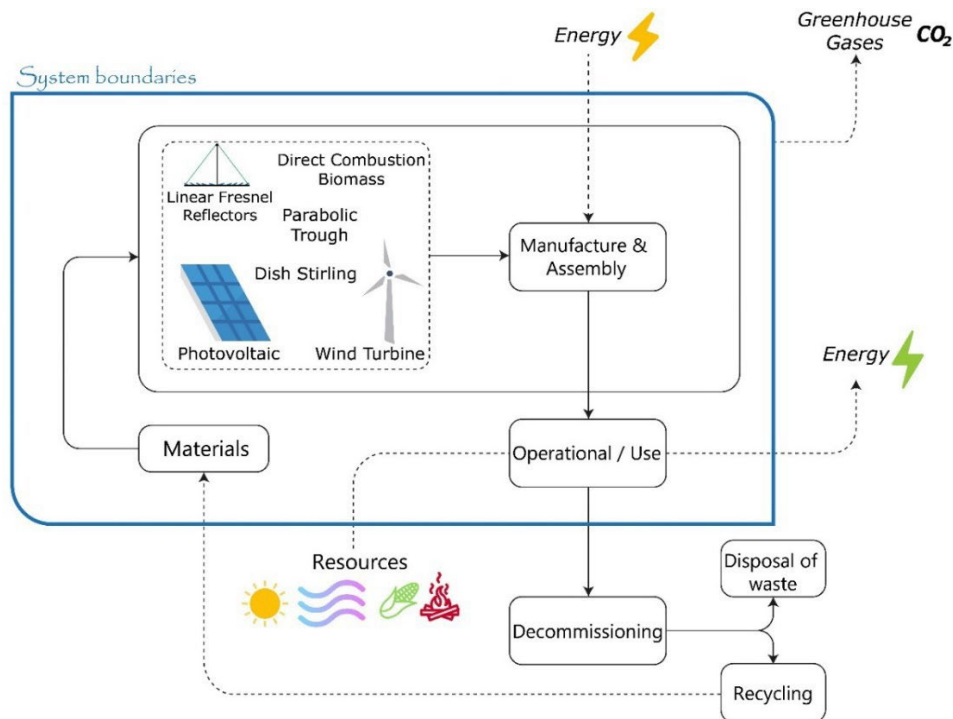


Figure 3.2: Life cycle boundary of the scoped RETs

For the environmental impact assessment, a process based LCA was used. The Umberto software developed by ifu Hamburg [122], Germany, and the Eco invent® database [123] was used to perform the LCA analysis. One of the predicted outcomes from LCA studies of energy technologies is that the main impacts originate from the production (manufacturing and assembly) and transportation of the technological components [16].

This study also adopts the eco-efficiency analysis, which is aimed at reducing the environmental impact while improving the economic value of a technological system or enterprise, by measuring the environmental impact attributed to each monetary unit earned [124]. Eco-efficiency can be expressed mathematically, as shown in equation (3.1).

$$Eco\ efficiency = \frac{environmental\ impact}{financial\ performance} \quad (3.1)$$

Eco-efficiency characterises reducing ecological damage to a minimum while at the same time maximizing efficiency.

In Equation (3.1) the **environmental impact** can be pollution emissions, resource-used (water or energy used) and the cost associated with an environmental burden, while **financial performance** can be value added or benefit, unit of product or service and cost associated with an environmental burden (traffic congestion costs).

The eco-efficiency is composed of a set of indicators rather than being a single index of economic performance. Therefore, a good eco efficiency quantity would be one that enhances the quality on a product or service while reduction environmental impacts.

3.2.5. Impact assessment (Environmental)

The characterization of results based on the impact category, normalisation and weighting of processes are part of the phases in the environmental impact assessment in an LCA [125]. The evaluation of novel and emerging technologies indicates the need for a broader environmental perspective; hence, a deliberate assessment of all relevant impact categories is included in the study. The impact assessment method used in the study is

the comprehensive International Reference Life Cycle Data System (ILCD). **Table 3.1** shows the impact category in the ILCD method. According to ISO 14040/14044, normalization and weighting are not obligatory in ranking the impacts of a system [111, 112].

Kicherer et al. [126] discuss the necessity to be able to compare the different environmental impact categories because of the difference in each unit and how under eco-efficiency consideration, decision-making becomes easier when the impacts are normalized. As next steps, the normalised values are combined via a weighting scheme. In a comparative analysis intended to be disclosed to the public, such as in this study, the ISO 14045 [127] regulates that weighting shall not be used. Nevertheless, this study tried to weight the environmental indicators in a relatively objective and transparent way to present a solution to the uncertainty and sensitivity analysis of the results.

Table 3.1: ILCD impact assessment method

Impact category indicators	Units
Acidification	mole H ⁺ eq.
Climate change	kg CO ₂ eq.
Freshwater ecotoxicity	CTU _e
Freshwater eutrophication	kg P eq.
Human toxicity, carcinogenics	CTU _h
Human toxicity, non-carcinogenics	CTU _h
Ionizing radiation, ecosystem	CTU _e
Ionizing radiation, human health	kg U-235 eq.
Land use	kg SOC
Marine eutrophication	kg N eq.
Ozone depletion	kg CFC-11 eq.
Particulate matter	kg PM _{2.5} eq.
Photochemical ozone formation	kg C ₂ H ₄ eq.
Resource depletion – mineral, fossil & renewable	kg Sb eq.
Resource depletion – water	m ³
Terrestrial eutrophication	mole N eq.

The weighting method aggregates all impact category indicators into an environmental score index, making it possible to calculate the ratio of the impacts. Although there is a lack of scientific basis for weighting results from LCA analysis [111], to render results generally compatible and applicable for the European Union member states, this study applies a recommended equal weight of 0.066 by the Joint Research Centre of the European Commission (EC-JRC) [128].

In this study, the LCA results are expressed in terms of CO₂-eq. emissions for assessing greenhouse gas (GHG) emissions of RET systems. This means that CO₂ and other GHGs, such as N₂O and CH₄, have been included in the assessment; GHG emissions (kg CO₂-eq./kWh) are estimated based on the amount of energy generated or stored (in the case of storage tanks or batteries) by each RET. Although other GHGs have different effects on the climate and atmospheric life span, each GHG is converted to an equivalent of CO₂ and is added to the assessment inventory to consider these differences. For example, relative to a gram of CO₂, a gram of CH₄ and N₂O has a global warming potential of 21 and 310, respectively, over a 100-year period [129].

3.3. Life cycle costing (LCC)

The LCC analysis is applied for economic impact assessment, which uses the same system boundaries as that of the life cycle assessment. To better align the economic information with the environmental impact data, two categories will be considered to answer how the cost will be structured in an LCC analysis and how the time factor and final cost will be presented.

Cost definition for LCC – ISO 2017 [130] defines LCC as “a technique which enables comparative cost assessments to be made over a specified period of time, taking into account all relevant economic factors both in terms of initial costs and future operating costs”. Given the diversity of LCC methods, there exist guides and standards for conducting LCC for different contexts [130, 131]. However, this costing generally covers and estimate stage by stage costs and risk/sensitivity analysis. According to Miah et al.

[132], the interpreted LCC results are largely dependent on the selection of the LCC equation.

The investor and supply-chain actor perspectives are two distinct approaches to LCC decision making. Investors take a conventional LCC approach, whereas supply chain actors take an environmental LCC approach. In general, the LCC analysis provides critical economic information that enables decision-makers to comprehend the short- to long-term costs and benefits. The conventional LCC includes the following cost categories: operation and maintenance, capital expenditures, disposal, and external costs; each of these cost categories contributes to the total cost category [132]. The environmental LCC method includes the revenue and cost for each life cycle stage (with the exclusion of external cost) across the life cycle. It is important to highlight that after cost categories have been identified, the estimation costs can be calculated. The total conventional LCC and environmental LCC costs are shown in Equation (3.2) and (3.3).

$$T_{CLCC} = \sum_{Operation} c_n x_n + \sum_{Maintenance} c_n x_n + \sum_{Investment} c_n x_n + \sum_D c_n x_n + \sum_E c_n x_n \quad (3.2)$$

$$T_{ELCC} = \sum_{Raw\ materials} c_n x_n + \sum_{Manufacture} c_n x_n + \sum_{Use} c_n x_n + \sum_D c_n x_n + \sum_E c_n x_n \quad (3.3)$$

where, c is the cost factor, x is the cost element of n . D is the disposal, E is the external cost factor in the life cycle stage.

The final cost for the LCC analysis can be expressed in various ways (See **Table 3.2** for 5 approaches). Other approaches such as “Global cost” was mentioned by Moschetti et al. [133], “Net LCC” by Menikpura et al. [134], “Resale Value” by Minne and Crittenden [135] and others are mentioned by Miah et al. [132].

Table 3.2: Life Cycle cost approaches

LCC impact				
Value	categories	LCC formula	Long time span cost	Source
I	Net Present-Value	$NPV = \sum_{t=0}^n \frac{C_t}{(1+r)^t}$	Yes	[136]
II	Savings Investment Ratio	$SIR = \frac{\sum_{t=0}^n \frac{S_t}{(1+r)^t}}{\sum_{t=0}^n \frac{I_t}{(1+r)^t}}$	Yes	[136]
III	Payback Period	$PBP = \frac{\Delta initial price}{Original price}$	Yes	[137]
IV	Static State Cost	–	No	[138]
V	Normalised Cost	–	It depends	[139]

In addition, to evaluate how costs changes in the future and across different cost categories, a sensitivity analysis could be performed.

3.4. Techno-economic analysis

There are some studies [9, 113-116] developed on the techno-economic assessment of PV, solar-thermal, bioenergy, wind, and hybrid systems. Typical techno-economic analysis (TEA) relevant to the energy industry includes the following parameters affecting a technology's feasibility: Annual Energy Generation (AEG), Levelised Cost of Electricity (LCOE), Net Present Value (NPV) and Internal Rate of Return (IRR). To date, LCOE has been the most widely applied metrics for assessments of the techno-economic performance of RETs [140-142] since it allows for comparison of RET costs at different scales of plant operation and investment time horizons [143].

For the latter, the NPV, IRR and payback periods are some of the common indicators used in [144-146]. The LCOE, IRR and NPV are more appropriate indicators signifying the current value of an investment at any given time [147]. The LCOE is essential as it determines how much money is made per unit of electricity to recover the systems lifetime cost. These costs include the initial capital investment, operation and maintenance costs, any fuel cost for the system and the discount rate [148]. The IRR allows for comparison

across regions and technologies such that it considers all cost and benefits over a given project period. On the other hand, the NPV analysis allows for an intuitive assessment of the value of specific projects, as well as a comparison of different projects [149].

In this study, the LCOE (in \$/kWh) for all power generating systems have been calculated via the IRR and NPV cash-flow model as follows [150]:

$$LCOE = \frac{\left(\sum_{t=0}^n \frac{I_t + M_t + F_t}{(1+r)^t} \right)}{\left(\sum_{t=1}^n \frac{E_t (1-d)^t}{(1+r)^t} \right)} \quad (3.4)$$

where, t : time horizon, I_t : is the cost of investment, M_t : cost for operations and maintenance; F_t : fuel cost; r : discount rate, d : degradation factor, n : system's total lifespan, E_t : electricity discounted value.

Although LCOE alone might be an insufficient measure in an assessment when returns are essential, the combination of IRR and NPV would enable investors to make well-informed decisions founded upon the feasibility of the project potentials.

3.5. Integrated performance index

The overall performance sustainability of each RET is estimated in terms of its integrated environmental and techno-economic index (ETEI), weighing the environmental impacts, alongside the techno-economics by the contribution analysis for identifying dominating factors. Sensitivity and uncertainly analysis were conducted to investigate the robustness of the eco-efficiency performance and ETEI indicator. The eco-efficiency performance can be calculated using the following equation:

$$EE = \frac{LCC}{\text{Life cycle environmental impacts}} \quad (3.5)$$

The eco-efficiency performance of the RETs considered was interpreted through a two-dimensional graph. The relative LCC index in saving cost is presented in Equation (3.6) as the Y-axis of the graph, while the relative LCA index is expressed in Equation (3.7) as the X-axis of the graph.

In **Figure 3.3**, Zone 1 represents a region of lower environmental impact and cost (fully eco-efficient); Zone 2 represents higher environmental impact and low cost; Zone 3 represents lower environmental impact, higher cost; and Zone 4 depicts a region of higher environmental impact and cost (non-eco-efficient). The environmental and economic index score can be calculated using the following equations:

$$Environmental\ score = \frac{(LCA_{alternative} - LCA_{original})}{LCA_{original}} \times 100\% \quad (3.6)$$

$$Economic\ score = \frac{(Cost_{alternative} - Cost_{original})}{Cost_{original}} \times 100\% \quad (3.7)$$

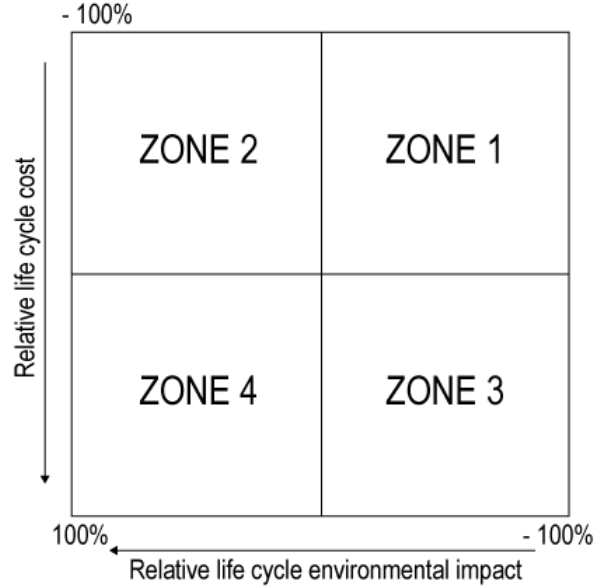


Figure 3.3: Eco-efficiency performance indicator graph

$$ETEI = Environmental\ score * LCOE \quad (3.8)$$

where, *LCOE* is the Levelised cost of energy (\$/kWh) for the different RETs, acquired using the methods described earlier. It is noteworthy that the lower ETEI scores represent greater performance sustainability.

3.6. Heat pipe deployment justification

The Innova MicroSolar (Innovative Micro Solar Heat and Power System for Domestic and Small Business Residential Buildings) is a European Commission-funded research and innovation project supported by the HORIZON 2020 Framework Programme. The Innova MicroSolar project's objective is to expand the use of solar thermal energy for power and heat generation in the residential and small business sectors. The coordinator for this project is Professor Khamid Mahkamov in the Department of Mechanical and Construction Engineering at Northumbria University.

The overall goal of the Innova MicroSolar project proposal is to develop an innovative, high-performance, and cost-effective 2-kWe/18-kWth solar heat and power system for use in individual dwellings and small business residential buildings for on-site electricity and heat generation using solar thermal energy at temperatures between 250 and 280 °C. The proposed technology is based on a novel flat Fresnel mirror solar concentrator and a micro–Organic Rankine Cycle (ORC) plant, as well as advanced Phase Change Material (PCM) thermal storage with reversible heat pipes for rapid charging and discharging. The heat pipes are an essential component of the thermal storage system. The task was to develop a detailed CFD model to be used in the designing process.

Amongst those mentioned, this study focuses on determining the environmental and techno-economic impacts associated with the deployment of various types of renewable energy systems, for which a life cycle and economic assessment of the renewable energy products. Furthermore, the reversible heat pipes for rapid charging and discharging for thermal storage application was also included in this study.

3.7. Chapter summary

In this Chapter, the framework for the comparison between mainstream and emerging solar-thermal renewable energy technologies (RETs) using an integrated environmental and techno-economic assessment methodology has been presented. The methodologies for calculating the life cycle cost (LCC), life cycle impact (LCI), and the Levelised Cost of Energy (LCOE), which are used to estimate the proposed system's economic and environmental performance, have also been discussed. This chapter also briefly gives reasons for the numerical modelling of heat pipes for application in solar thermal plants. In the next Chapter, the software and analytical tools used for the modelling process as well as the assumptions made for the life cycle assessment and techno-economic assessment are discussed.

Chapter 4 Software and analytical tools

This Chapter briefly describes the software and analytical tool used for the modelling process as well as the assumptions made for the life cycle assessment and techno-economic assessment. Furthermore, brief information on the locations for the different RETs, such as their geographical characteristics, is presented. A summary is presented at the end to conclude the Chapter.

4.1 Umberto Software

Umberto is an eco-efficiency software for material flow analysis and life cycle assessment, and is developed by ifu Hamburg [151], Germany, and utilises the Eco invent® database [123]. The Umberto product family consist of two tools, namely, Umberto Efficiency+ and Umberto LCA+. The Umberto Efficiency+ is used to analyse material flows to improve energy and material efficiency, perform cost accounting to determine potential production cost savings, calculate the true cost of material losses, and track CO₂ balances to meet set climate targets. On the other hand, the Umberto LCA+ performs all of the functions of the Umberto Efficiency+ but also calculates the life cycle of all environmental impacts throughout the product's life cycle, combining life cycle costing with an integrated ecological evaluation to enable eco-efficient decision-making. [122]. In this study, the Umberto LCA+ is used for the environmental, cost accounting and climate impacts for the different renewable energy technologies.

4.2 System Advisor Model (SAM)

The System Advisor Model (SAM) is a renewable energy systems modelling software developed by the US National Renewable Energy Laboratory (NREL) [152]. The SAM's database allows appropriate technology selection and system configuration, providing both financial models and annual energy production for economic analysis. The input parameters needed by the SAM software are the energy resource data, technological configuration and performance data, financing data, and system cost. In this study, SAM

is used to assess the energy outputs, levelized cost of energy, net present value and the simple payback time of the different renewable energy technologies. The energy outputs for the scoped RETs are estimated using established formulations from the literature; all the RETs have been normalised to a nominal capacity of 2 MW and Technological Readiness Level of five, avoiding any bias in the comparison. The combination of an Organic Rankine Cycle for the two solar-thermal RETs is meant to enhance their techno-economic performance through additional energy recovery, enabling their suitability for low-to-medium temperature applications. The energy analysis accounts for electricity generation from all the RETs and the additional thermal outputs from the solar-thermal systems.

4.3 ANSYS

ANSYS is a software package for modelling real-world problems digitally. It solves physics problems numerically using computer-based techniques. [153]. ANSYS solves problems across the entire spectrum of physics, accurately simulating the structural, stress, fluid flow, heat transfer, and electromagnetic properties of any product or process. In this study, the ANSYS software is used for modelling three different heat pipe orientations to evaluate the most efficient heat transfer heat model based on their orientation, geometry, and thermal properties.

4.4 Matrix Laboratory (MATLAB)

MATLAB is a high-level language for scientific and engineering computing. It integrates visualization, computation, and programming, making it easy to use and express problems and solutions in a familiar mathematical notation [154]. In this study, MATLAB is used for data analysis to evaluate the cost calculations, the life cycle impacts of the RETs, the techno-economic performance of the RETs and analysis of the mass flow rate and the heat transfer rate in the different heat pipe orientations and generating plots to show corresponding results.

4.5 Life cycle assessment assumptions

The overall goal of this study is to evaluate the environmental performance of manufacturing different renewable energy technologies in view of future developments, comparing some of the mature mainstream RETs with emerging solar-thermal systems. **Figure 3.2** (in Chapter 3) shows the basic LCA process flows and the system boundaries for the scoped RETs, including extraction of raw materials, manufacture as well as transportation for construction and use phase. The models assume impacts from plant operation to be negligible.

The ReCiPe method, which combines Eco-indicator 99 and CML indicators [41], is used to analyse the impact of the RETs on the environment. The nominal capacities for the scoped RETs are obtained from various literature [7, 9, 10], which have been scaled to a 2 MW plant capacity to harmonise the analysis. All the technology-specific primary data for the RETs have been sourced from the relevant literature (wind power, biomass, PV [15], linear Fresnel and parabolic trough [16], dish Stirling [10]). Generic secondary data (materials, energy supply chain and transport processes) and cost databases are sourced from Umberto [151], which utilises the Eco invent® database [123]. This enabled the creation of different cost and environmental scenarios with regards to the market, technological, price, legal and demand trends. Recycling of any material components is not considered within the scope of assessment. For each RET, the electricity generation functional unit is kept at 2 MWh; all the components are assumed to be transported from the factory to the installation site within a maximum distance of 2000 km.

4.6 Techno-economic assessment assumptions

The following common financing input parameters have been applied to all the benchmark RETs - real discount: 5.5%; inflation rate: 2.5%; tax investor IRR target: 10%; IRR target years: 11; and analysis period: 25 years. The default data of the renewable technologies provided in SAM is used, except for the capital and O&M costs for the considered technologies (obtained from the Annual Technology Baseline [155]). The cost input data from SAM (i.e., capital, fixed and variable cost) are then compared with values from the transparent cost database of the Open Energy Information (OpenEI) [156]. The default input parameters value for costings of the different RETs in SAM is obtained from the

literature [157, 158]. The CSP technology-specific design parameters are shown in **Table 4.1**. The irradiation design point is set to 950 W/m² for all three CSP technologies.

Table 4.1: CSP technology-specific design parameters

	<i>UNITS</i>	PT-ORC	LFR-ORC
Cycle efficiency (2MW)	%	18	18
Boiler Pressure	<i>Bar</i>	20	20
Outlet temperature	°C	490	490

4.6.1. Wind turbine system

The wind turbine modelled is a direct-wind drive turbine rated at 2 MW with the following specifications: rotor diameter 96 m, hub height 80 m, shear coefficient 0.14. The power generated from the wind turbine is estimated following [159], as below:

$$P_{WT} = \frac{1}{2} \rho A V^3 \quad (4.1)$$

where, V is wind speed in m/s, ρ is the air density in kg/m³ and A is the rotor area to the direction of flow in m².

Wake effect losses are not considered in this calculation. The wind profile is modelled using the Weibull probability distribution, as follows:

$$f(V) = \frac{k}{\lambda^k} \times (V)^{k-1} \times e^{-(V/\lambda)^k} \quad (4.2)$$

where, $f(V)$ is the Weibull probability wind speed distribution function, k is the dimensionless shape parameter, the scale parameter in m/s is represented by λ , and V is the wind speed in m/s.

SAM automatically estimates the balance of system costs directly from the NREL financial model database after the input properties have been inserted [160]. **Table 4.2** presents cost data for land-based utility-scale turbine (capacity: 1 MW or greater).

Table 4.2: Wind Turbine system cost

VARIABLE	VALUE
Turbine cost	1,209 \$/kW
Balance of system cost	330 \$/kW
Operation & Maintenance	51 \$/kW-yr

4.6.2. Photovoltaic system

The PV system configuration modelled comprises a field of non-tracking SunPower SPR-E19-310-COM mono-crystalline silicon modules, an inverter unit, and a Lithium-Ion² battery storage unit. The power produced by PV modules calculated as below:

$$P_{pv} = IA_{pv}\eta_{pv} \quad (4.3)$$

here, I represents the solar irradiance, A_{pv} represents the PV module area, η_{pv} is the overall efficiency of the PV unit. The inverter unit acts as an interface between the AC load, solar modules, and the battery storage. In this system configuration, the batteries store the electrical energy supplied by the solar modules in electrochemical form. The charge controller distributes the power to the battery for charging, or the load, depending on the quantity of the DC power generated by the solar modules. **Tables 4.3, 4.4, and 4.5** respectively show the battery specifications properties, the system configuration, and the economic parameters used for the PV system analysis in this study [12].

² The Lithium Ion: Lithium Iron Phosphate (LFP) is a battery storage used in this study.

Table 4.3: Power-wall Specifications for PV system [12]

VARIABLE	VALUE
Price	\$3000
Capacity	7 kWh
Power	2.0 kW continuous, 3.3 kW peak
Efficiency	92%
Voltage	350 – 450 V
Current	5.8 A nominal, 8.6 A peak
Weight	100 kg
Dimensions	1300 mm x 860 mm x 180 mm

Table 4.4: PV system configuration

PARAMETER	VALUE
PV system size	2 MW DC
Inverter size	1.54 MW
Storage power capacity	1 MW AC
Storage energy capacity	4 hours (4 MWh AC)
Storage efficiency	85 % (AC-AC)

Table 4.5: PV system costs [12]

VARIABLE	VALUE
Module cost	0.64 \$/Wdc
Inverter cost	0.10 \$/Wdc
Battery cost	300 \$/kWh Lithium Ion
Balance of system equipment	0.24 \$/Wdc
Installation labour	0.15 \$/Wdc
Installer margin & overhead	0.16 \$/Wdc
Permitting	0.06 \$/Wdc
Operation & Maintenance	20 \$/kW-yr

4.6.3. Biomass system

Generally, two methods exist for converting biomass into useful energy - biochemical and thermo-chemical processes. This study modelled the direct combustion process, which is the simplest way of biomass conversion using a combustion device, such as industrial boilers or furnaces [161]. The biomass system consists of a grate stoker furnace combustion system with boiler parameters having a temperature of 510 deg. C and a steam pressure of 83 bar. This biomass system appears to a steam Rankine cycle with a nameplate capacity of 2 MW. The cost parameters used in the model are shown in **Table 4.6**.

Table 4.6: Biomass system costs [162]

VARIABLE	VALUE
Boiler cost	750 \$/kW
Turbine and generator capacity	510 \$/kW
Fuel Handling equipment	330 \$/kW
Dryer capacity	140 \$/kW
Other equipment cost	270 \$/kW
Balance of plant	480 \$/kW
Fixed cost	184 \$/kW-yr
Variable cost	201.8 \$/MWh

4.6.4. Concentrated Solar Power (CSP) system

All the CSP systems modelled have a nameplate capacity of 2 MW and includes thermal energy recovery. The CSP system concentrates the direct normal insolation onto a receiver to raise the heat transfer fluid temperature between 150 to 1200 degrees Celsius, which produces electricity by driving steam turbines and generators [163].

The Dish Stirling system consists of the field layout of 5 collectors surfacing North-South and 20 collectors facing East-West. The LFR and the PT systems both consist of solar reflectors/collectors which are then coupled to an ORC power block and thermal energy storage. The solar field for the PT-ORC has a solar multiple field of 2. The solar field collects thermal energy with the use of Therminol 59 as the heat transfer fluid. The

Solargenix SGX-1 solar collector and the 2008 Schott PTR70 Vacuum receiver at a HTF temperature of 275°C [164] are used in this study. The thermal energy storage system comprises of a two-tank configuration, which has a full load equivalent of 4 hours.

The cost parameters for the CSPs modelled are shown in **Table 4.7**. It is noteworthy that there is a lack of linear Fresnel solar field cost details in the SAM modelling software and the broader published literature. Thus, the Fresnel solar field cost was set to be equal to the solar field cost of the parabolic trough. For mature linear Fresnel system design, this is assumed to be an upper limit because the linear Fresnel systems, when compared with the parabolic troughs, generally have a lower capital cost [158].

Table 4.7: System costs for the modelled CSPs [155, 156, 158]

VARIABLE	PT-ST	PT-ORC	LFR-ORC
Site improvement	25 \$/m ²	25 \$/m ²	25 \$/m ²
Solar field	150 \$/m ²	150 \$/m ²	150 \$/m ²
HTF system	60 \$/m ²	60 \$/m ²	60 \$/m ²
Storage	65 \$/kWht	65 \$/kWht	65 \$/kWht
Power plant	1200 \$/kWe	1250 \$/kWe	1150 \$/kWe
Balance of plant	120 \$/kWe	120 \$/kWe	120 \$/kWe
Fixed cost	75 \$/kW-yr	66 \$/kW-yr	66 \$/kW-yr
Variable cost	4 \$/MWh	4 \$/MWh	4 \$/MWh

4.7. Location

Seville (37.3891° N, 5.9845° W), the capital of southern Spain's Andalusia region, was chosen for the deployment of solar-based RETs, as it has global solar radiation of 4.86 kWh/m²day [165]; Malaga (36.7213° N, 4.4213° W), the coastal city in Southern Spain, is selected as a suitable site for deployment of wind turbines due to higher wind speeds in that region. Different locations for solar and wind resource were selected to assess each renewable energy technologies for optimal energy production. The location specific hourly values for wind speed and solar radiation were procured from typical meteorological year

(TMY3) data obtained from the EnergyPlus weather datasets [166] and the European Commission website [167].

Concentrating solar power (CSP) systems, like most renewable energy applications, must cope with variable and unpredictable operating conditions. Each CSP plant is designed around a nominal set of operating conditions – the so-called design point – but the goal of every CSP system is to produce the maximum amount of electricity or process heat under varying conditions over an entire year of operation. The systems are hence designed to accommodate their locations' geographical and meteorological properties without compromising the manufacturability of CSP system components. The design point generally consists of a set of operating conditions and the resulting system output. For the collector field of a CSP plant, the direct normal irradiance (DNI) and the sun's incidence angle at the system aperture are the most relevant operating conditions, as they determine the amount of solar power incident on the CSP system [168].

In this study, the irradiation design point for the concentration solar plants is assumed to be 950 W/m^2 to reflect Seville's global solar radiation of $4.86 \text{ kWh/m}^2\text{day}$.



Figure 4.1: Map of Spain

4.8. Chapter summary

This Chapter has presented a brief description of the software tools used in this study and stated the assumptions made for performing the environmental and techno-economic assessment of the RETs. Also, a brief geographical characteristic based on the available energy resources in Spain was presented. In the next chapter, the results and analysis are discussed. In addition, two other location scenarios are added to perform the comparison of the different technologies.

Chapter 5 ETEA Results and Discussions

The Chapter presents the results and analyses of the RETs case study scenarios. It begins by evaluating the capacities of the RETs, considering the design parameters and the environmental and techno-economic assumptions discussed in Chapter 4. The results of three different scenarios are presented. The first scenario serves as a baseline; with a focus on the climatic condition in Spain. While scenario 2 focuses on the climatic condition in the United States.

Each scenario is examined in five stages. The first stage presents results and analysis for the annual heat and electric outputs of the RETs. The second stage deals with the interpretation of the LCA result for the RETs. The third stage deals with the results for the capacity factors, LCOE, NPV, simple payback time and while part four presents the results for the integrated environmental and techno-economic impact assessment. The fifth stage presents the eco-efficiency index. A summary concludes the Chapter.

5.1. Case study

A hypothetical 2-MW power plant is modelled and demonstrated for all renewable technologies, namely Photovoltaic (PV), Wind Turbine (WT) and Bioenergy (direct combustion), with several emerging solar-thermal RETs, including Parabolic Trough (using steam turbines), Parabolic Trough- and Linear Fresnel Reflectors with Organic Rankine Cycle turbine (PT-ORC and LFR-ORC, respectively) using SAM. This case study would be presented in two scenarios which are location depended. Scenario 1 serves as a baseline as highlighted in section 4.7 is Spain while scenario 2 focuses on the climatic condition in the United States. **Figures 5.1** and **5.2** below show the different wind speeds, temperatures, and solar potential in Spain while **Figures 5.3** and **5.4** show the different wind speeds, temperatures, and solar potential in the United States. The electric demand used in this study (for both scenarios) is shown in **Figure 5.5**. Literature suggests that a day-based period in the dry season is usually used to determine the effectiveness of solar technologies (PV and CSP) [129]. However, to assess the reliability and make informed decision on the performance of the energy technologies, a detailed analysis that considers all seasons during a year should be evaluated.

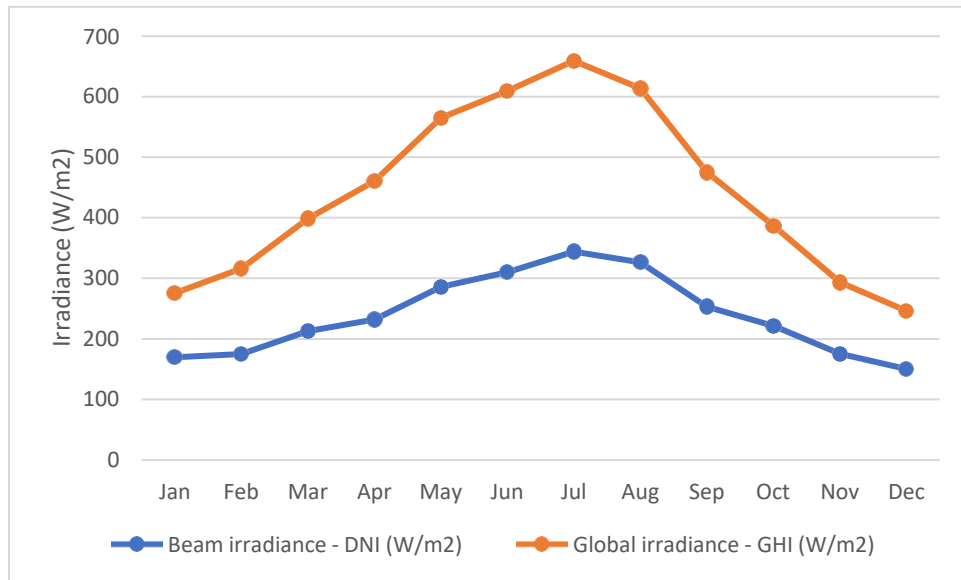


Figure 5.1: Global and beam irradiance for Spain

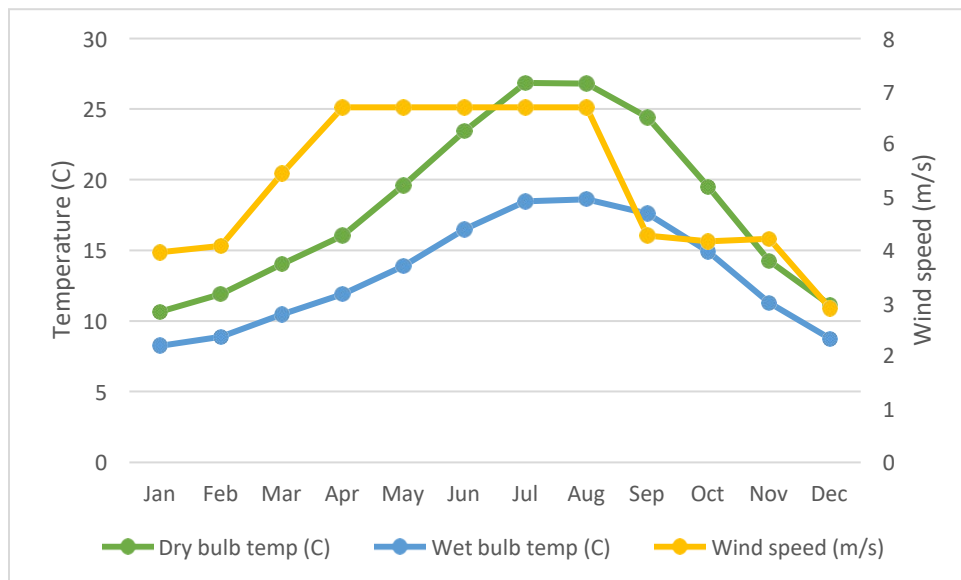


Figure 5.2: A plot showing the resource for wind speed, wet and dry temperatures in Spain

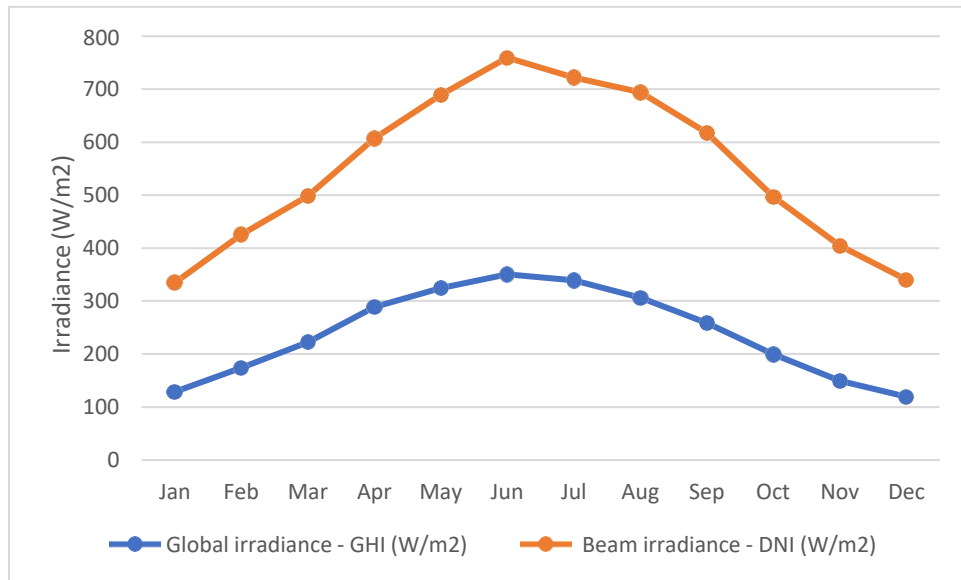


Figure 5.3: Global and beam irradiance for the United States

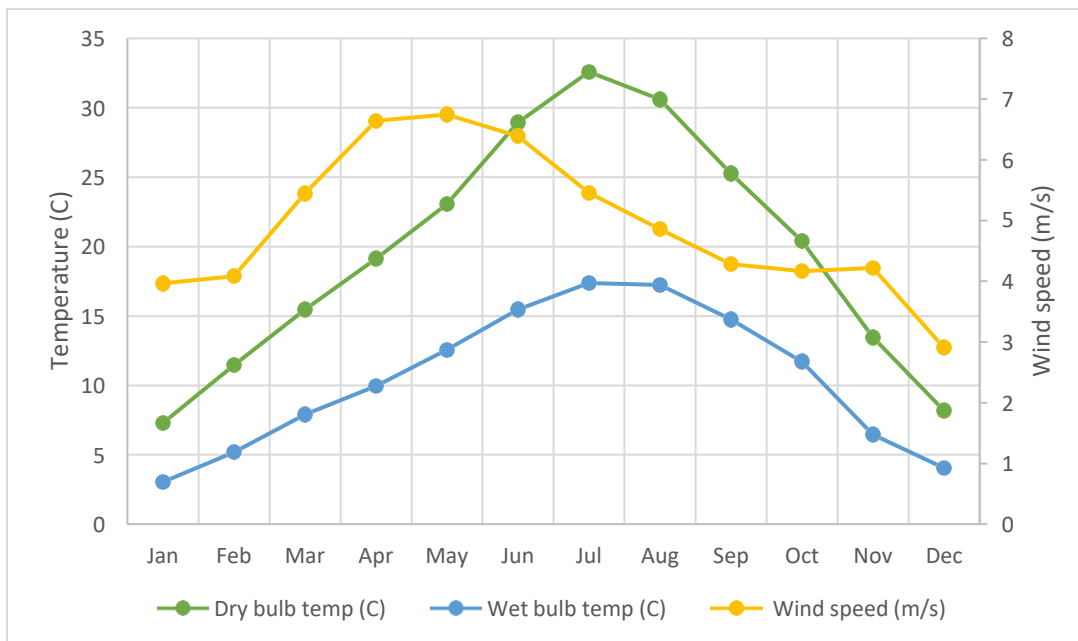


Figure 5.4: A plot showing the resource for wind speed, wet and dry temperatures in the United States

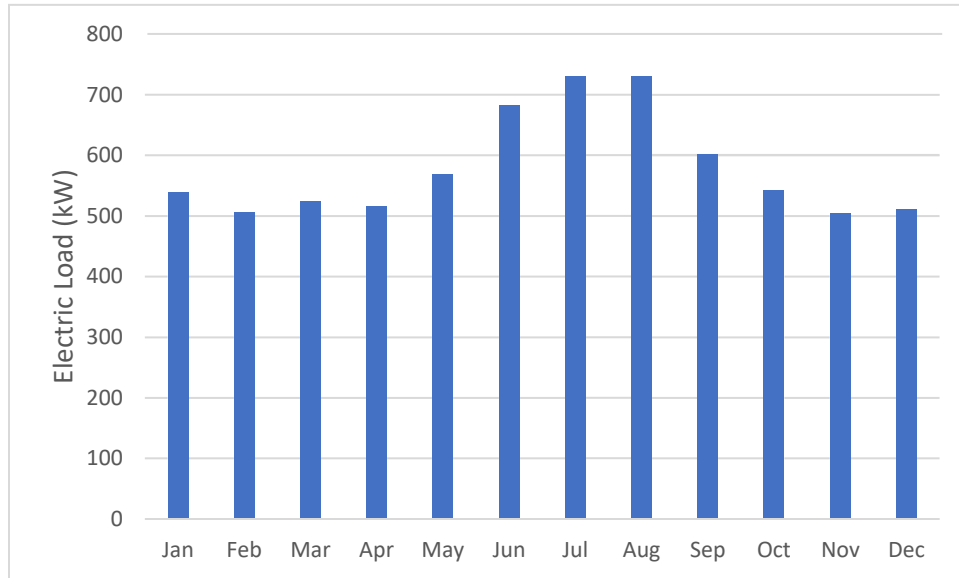


Figure 5.5: User demand profile used for the simulation of RETs

5.1.1. Scenario 1 (Spain)

The annual energy output from the 2 MW capacity plants for the different RETs evaluation for Spain are plotted and compared in Figure 5.6. Spain was selected for the baseline case study because, in 2017, the total renewable energy capacity was 47,989 MW [169]. This implies that the country is feasible for the deployment of RETs. In addition, Spain has the third highest renewable energy generating capacity in Europe after Italy and Germany [169].

The Biomass system shows the highest annual electricity generation potential, followed by the Wind turbine system and the steam-driven Parabolic trough (PT-ST) system, respectively, approximately 13200 MWhe, 4800 MWhe and 4400 MWhe. On the other hand, the electricity output from the PT-ORC, LFR-ORC and PV respectively yielding approximately 4100 MWhe, 3500 MWhe and 3400 MWhe. It is noteworthy, the electricity outputs from both the LFR-ORC and PT-ORC are competitive to the PV system, which can be mainly attributed to better use of the primary energy via the waste heat recovery potential of the ORC and its subsequent conversion into electricity.

However, incorporating the additional thermal energy output from the PT-ST, PT-ORC and LFR-ORC systems, respectively estimated as approximately 17000 MWh, 32700

MWh and 21300 MWh, make their annual total energy outputs significantly higher than the mainstream RETs (shown on the right y-axis). This shows the added energy recovery potential of the solar thermal RETs combining an ORC and stream driven turbine (for the case of the PT-ST) system; the relatively higher thermal energy output from the PT-ORC can be attributed mainly to the maturity of this technology.

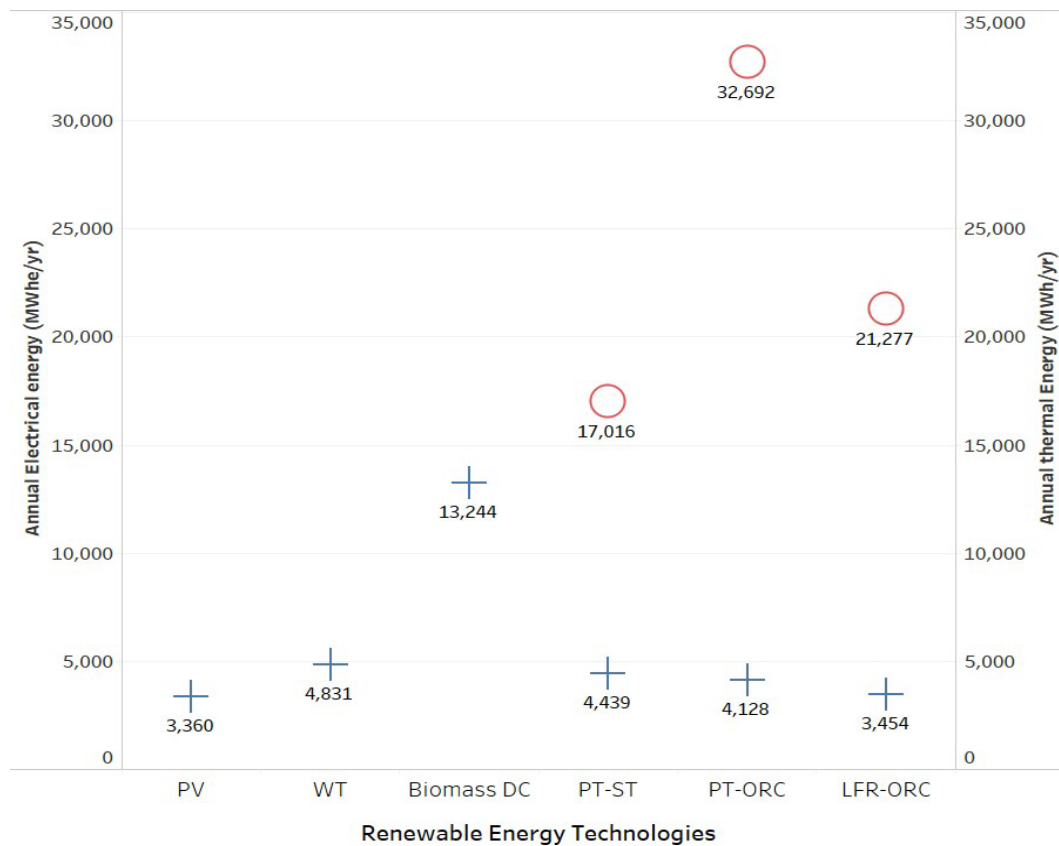


Figure 5.6: Annual energy output from different RETs (Note: left y-axis - Electrical energy only; right y-axis – Total energy, i.e. electrical and thermal combined, respectively shown as + and O) in Spain

Environmental impact for each RET is evaluated in terms of individual impact categories and the normalised LLCI values (lower values implying more favourable). The individual environmental impacts for the hypothetical 2 MW power plant, based on the literature data for the corresponding RETs, are shown in **Table 5.1**. The impact categories differ by size and type of technology; the impacts are presented as kg per kWh for different RETs.

However, from the results obtained, no RET emerges as the most preferred option in terms of life cycle impact. The climate change indicator for the various RETs was normalised using the total electricity output to obtain the Levelised life cycle impact (LLCI, shown in **Figure 5.6** on a logarithmic scale).

Interestingly, the LLCI of the conventional RETs is found to be higher, with LFR-ORC having the lowest score (**Figure 5.7, left y-axis**). The high LLCI in terms of kg/kWh of electricity is the WT system and can be attributed to the use of gearless synchronous generators, requiring permanent magnets incorporating neodymium and dysprosium, which are rare earth metals and hence contributing to higher environmental impacts [170].

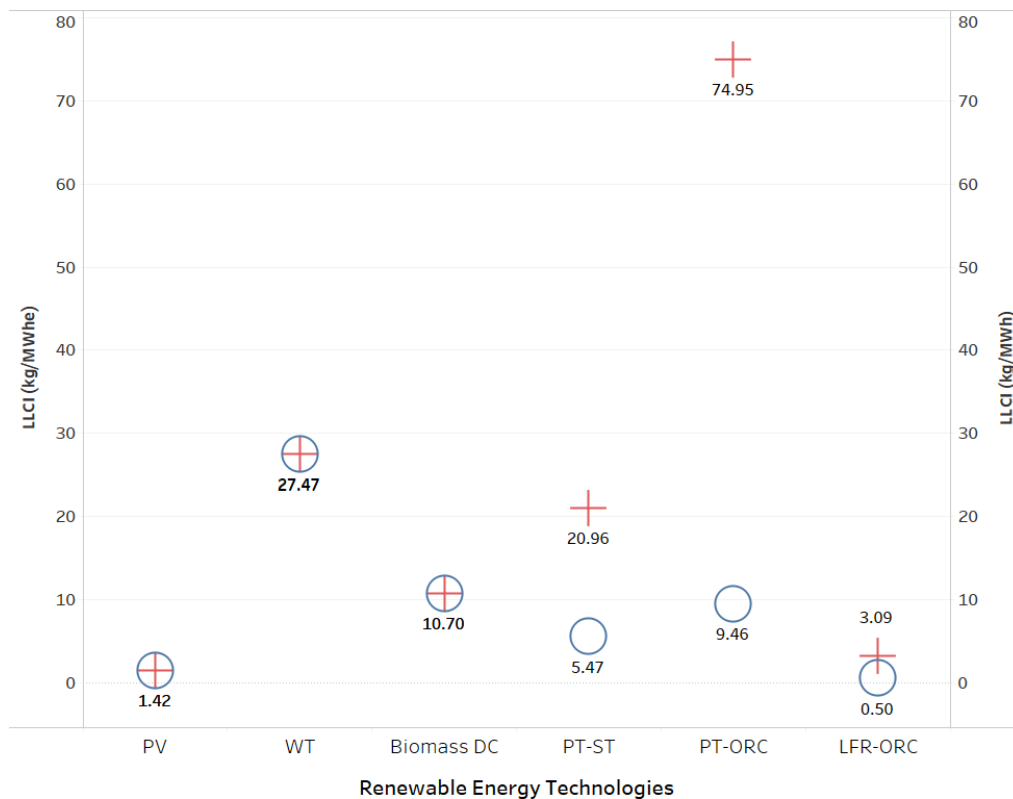


Figure 5.7: Levelised life cycle impact of the RETs (Note: left y-axis – accounting for Electrical energy only; right y-axis – accounting for Total energy, i.e., electrical, and thermal combined, respectively shown as O and +) in Spain

Further, PT-ORC exhibited the highest LLCI score after WT when the thermal output is considered, which can be attributed to the use of steel in component manufacturing and the use of synthetic oil as heat transfer fluid [16].

Table 5.1: Life cycle impacts of the scoped renewable energy technologies (kg/kWh)

Impact Category	Reference unit	Photovoltaic	Wind turbine	Biomass	PT-ST	PT-ORC	LFR-ORC
<i>Terrestrial acidification</i>	kg SO ₂ . Eq	1470.9	15319.68	24,007.70	2,372.17	29185.11	27.29
<i>Photochemical oxidant formation</i>	kg NMVOC	0.98	339.02	188.53	3.43	3084.32	0.02
<i>Freshwater eutrophication</i>	kg P. Eq	2.31E-03	7.96	4.2	0.05	56.66	4.29E-05
<i>Climate change</i>	kg CO ₂ . Eq	4770	132690.14	141,650.56	93045.38	309,393.15	10,656.86
<i>Particulate matter formation</i>	KG PM10. Eq	192.28	2341.34	3,315.18	311.99	6014.61	3.35
<i>Fossil depletion</i>	kg oil. Eq	7.47E+03	33250.45	21,584.70	603.19	213049.28	15.1

Table 5.2: Comparison of actual/simulated published data and simulated data from this research

Description	Unit	Actual/Simulated Published data						Simulated data from this work					
		PV	WT	BIOMAS S DC	PT-ST	PT-ORC	LFR-ORC	PV	WT	BIOMAS S DC	PT-ST	PT-ORC	LFR-ORC
Location		Aizawl India	Southeastern Colorado					Spain	Spain	Spain	Spain	Spain	Spain
Plant size	MW	2	2					2	2	2	2	2	2
Annual energy	MWh e	3928	326,218					3360	4831	13244	4439	4128	4831
Capacity factor	%	20.1	37.2					19.2	27.6	86.6	25.4	23.6	18.9
LCOE	\$/kW h	0.049	0.073					0.014	0.030	0.109	0.054	0.064	0.055
Payback time	years	8.6	-					2.4	5.0	6.5	8.0	7.0	8.0
NPV	\$	8.66	36,632,000					7,340,318	2,959,251	445,864	738,526	1,622,910	420,482

However, accounting for the thermal energy makes the LLCI of the PT-ORC comparable to WT and Biomass systems (**Figure 5.6, right y-axis**). Overall, the LFR-ORC outperformed the mainstream RETs studied, attributed to their lower environmental impacts (approximately 100% lower LLCI on average). For every 1 kW of electricity generation, the PV system respectively has the lowest and the highest GHG emissions (contribution to global warming potential – climate change, **Table 5.1**). The higher emissions from PT-ORC is attributed to the utilisation of synthetic oil as the heat transfer fluid (HTF). Moreover, possible leakages and the periodic replacement of thermal oil during plant operation and maintenance activities can be associated with additional ecological impact.

All the mainstream RETs show relatively lower LCOE, typically ranging between 0.01 and 0.10 \$/kWh (attributed mainly to their higher electricity outputs and low operation and maintenance costs); all the solar-thermal technologies show relatively higher LCOE, typically ranging between 0.05 and 0.06 \$/kWh. While PV shows the lowest LCOE of 0.014 \$/kWh, Biomass and PT-ORC systems are found to have the highest LCOE among all the 2 MW RETs, approximately corresponding to 0.11 and 0.06 \$/kWh, respectively (Figure 5.8). Thus, comparing solely on the techno-economic basis, the mainstream RETs are found to be more favourable than their solar-thermal counterparts, with up to 200% lower LCOE on average. It should be noted, however, this study considered only the cost of energy generated, with no adjustments for the time of delivery or power dispatch. A previous study comparing solar-based ORC with PV [171] concluded that the addition of energy storage favours the ORC system to the PV system in terms of Capacity Utilization Factor and LCOE for a decentralised plant capacity level of 50 kW_e. The energy cost seems to be justified when the electrical and thermal power outputs are both utilised from the solar-thermal system.

Nevertheless, for the LFR-ORC system to be competitive with other solar RETs (mainly PV system), it needs radical technological optimisation for its better performance and cheaper LCOE.

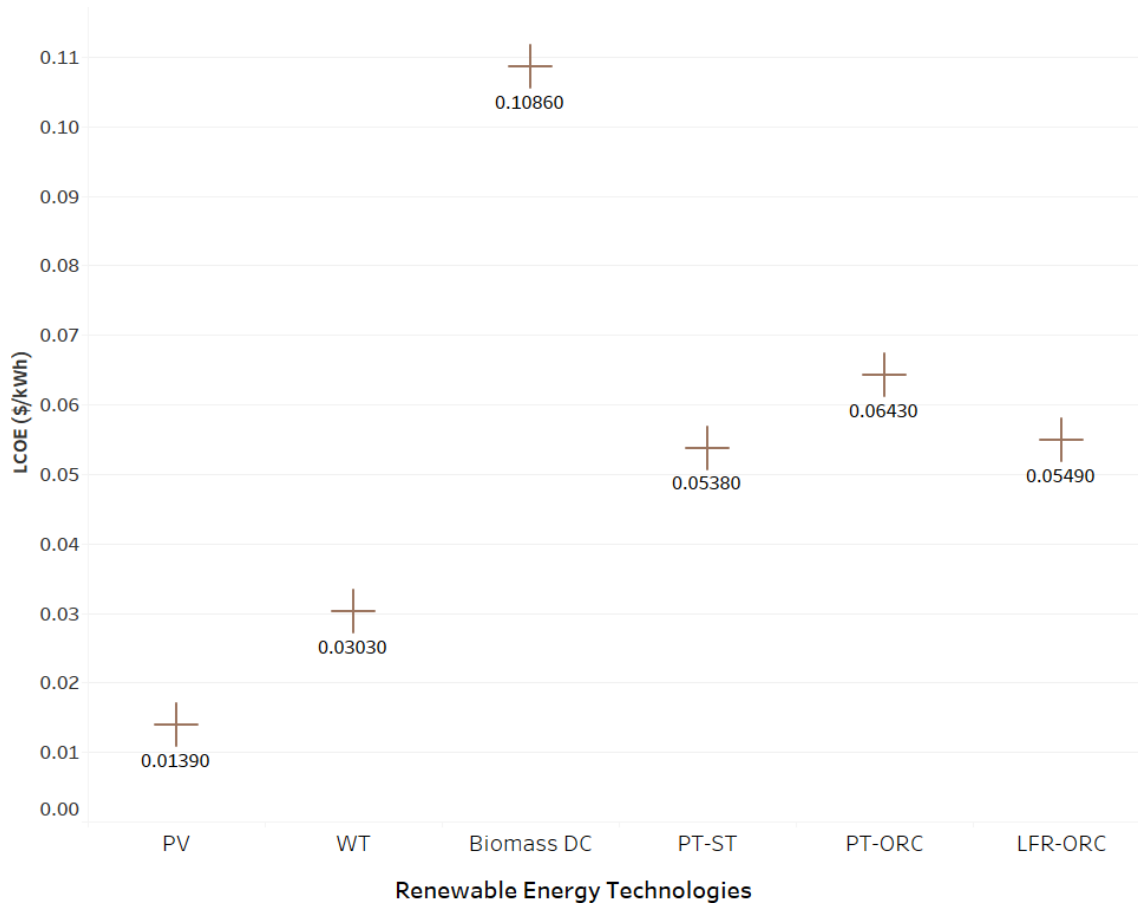


Figure 5.8: Levelised cost of energy for the scoped 2 MW RETs in Spain

Table 5.3 presents results for carbon saving potential (tCO_2/MWh) from electricity generation, net capital cost, NPV (in US\$), capacity factor, and simple payback time of the different renewable energy technologies. The greenhouse gases emitted for the production or usage of a certain amount of electricity is defined by the emission factor. Thus, the annual carbon savings $S_{fuel}(tCO_2yr^{-1})$ is calculated by multiplying the annual electricity output, $e_{out}(MWh\ yr^{-1})$ by the emission factor, $E_{fuel}(tCO_2MWh^{-1})$ [172]. It can be observed that PV has the highest NPV cost upon project completion. The LFR-ORC system has compatible carbon saving as the PT-ORC and PV system, whereas those for the Biomass system is the most dominant, followed by the WT system, indicating their levels of carbon savings over the 25-year operational life. Additional, the Biomass and WT systems show higher capacity factor. It can be observed that PV has a

payback time

of 2.4 years which is the lowest of all the RETs. Since the NPV takes into account the time factor of money, this is a useful indicator of project feasibility from an investment perspective. The LFR-ORC appear to have the lowest NPV, while the PT-ORC has the highest net capital cost of about 13.5 million US dollars.

Table 5.3: Economic indicators of renewable energy technologies in Spain

Renewable Energy Technology	Capacity Factor (%)	Simple payback time (years)	tCO₂/MWh Savings	NPV (\$)	Net Capital cost (\$)
PV	19.2	2.4	1545.672	7,340,318	4,139,802
WT	27.6	5	2222.313	2,959,251	3,078,000
Biomass DC	86.6	6.5	6092.338	445,864	8,228,155
PT-ST	25.4	8	2041.935	738,526	11,283,964
PT-ORC	23.6	7	1898.859	1,622,910	13,537,489
LFR-ORC	18.9	8	1588.787	420,482	11,482,173

Based on Eq. (3.2) and (3.3), the life cycle cost and life cycle environmental impact are translated into the relative life cycle cost and relative life cycle environmental impact, respectively. The individual environmental impacts indicator for the hypothetical 2 MW power plant, based on the literature data for the corresponding RETs, are shown in Table 5.1. The 6 impact categories differ by type of technology. However, from the results obtained, no RET emerges as the most preferred option in terms of life cycle impact. Figure 5.7 shows the relative life cycle environmental score for all renewable energy systems. From an eco-efficiency perspective, RETs system located in Zone 1 is considered economically feasible and environmental friendly; in this case, all the RETs were located in Zone 1. The closest to centre of the graph technology (PV) turns out to be the cheapest and the most environmentally friendly technology. Although the LRF-ORC system is environmental friendly, it is costly in term of its net capital cost (see table 5.2); the PT-ORC system is the most environmentally unfriendly in comparison to the other RETs followed by the WT system. The scores of the LCA and LCC for the PT-ORC could be attributed to the utilisation of synthetic oil as the heat transfer fluid (HTF).

Moreover, possible leakages and the periodic replacement of thermal oil during plant operation and maintenance activities can be associated with additional ecological impact. For every 1 kWh of electricity generation, the PV and LFR-ORC technologies have the lowest environmental and economic burdens.

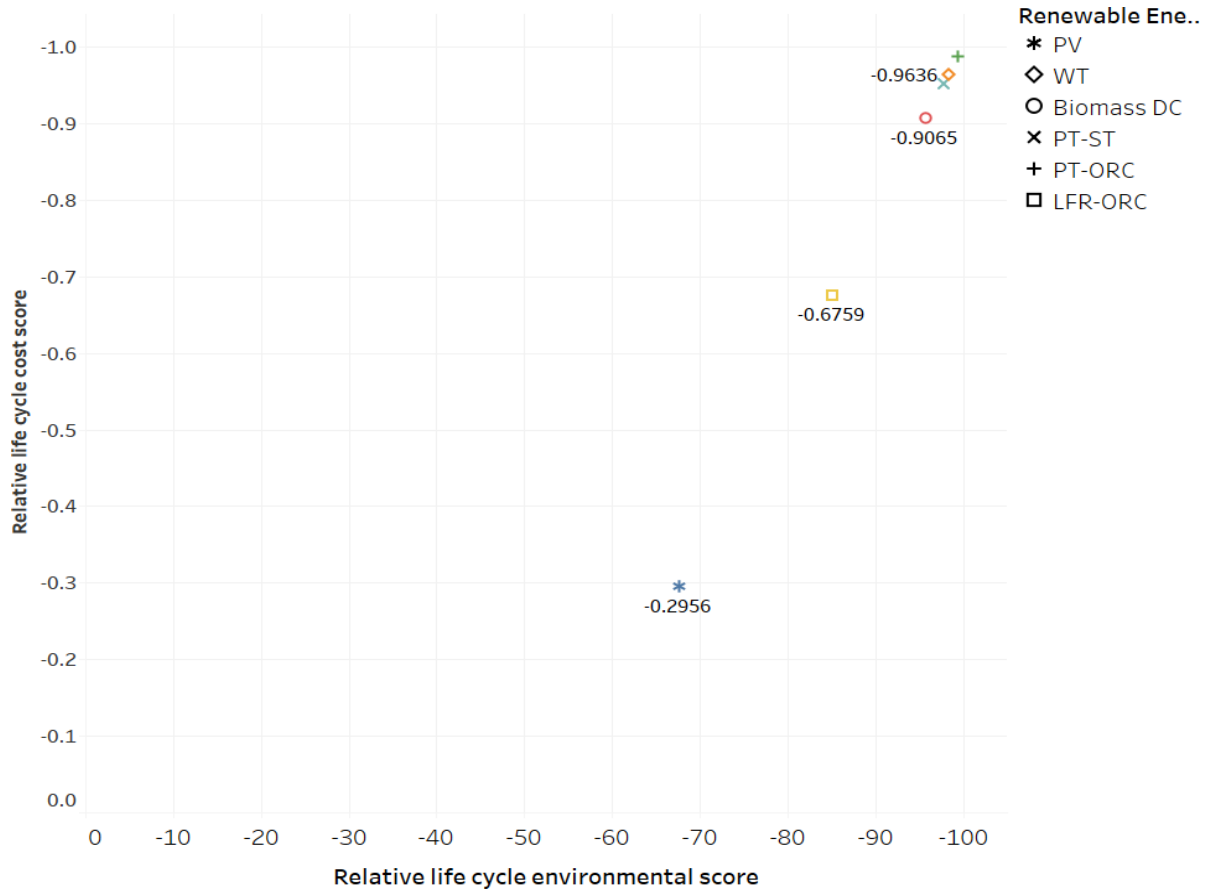


Figure 5.9: Eco-efficiency index scores

The lower score for the LFR-ORC system can be attributed to the following factors: 1) the use of fixed receiver not connected to any moving parts – which means that fewer material resources are used in the manufacturing process; 2) use of environmentally sustainable heat transfer fluid; 3) use of flat mirrors, which allows the reduction in cost, and the alignment of the reflectors in one plane, with the advantage of reduced wind loads (hence, lower replacement costs); 4) use of simple absorber tubes, skipping the need for expensive vacuum technology and metal-glass sealing (hence, lower ecological impacts).

The result indicates that different RET innovations have the potential to improve eco-efficiency. Innovations are essential for reducing the recycling cost while improving product quality. The use of a variety of tools provides the decision-maker with flexibility. For instance, the decision-maker may prefer to optimise economic and environmental outputs using weighting criteria rather than employing mathematical optimization techniques.

5.1.2. Scenario 2 (United States)

For the second scenario, Daggett within the state of California in the US with coordinates of 34° 51'48 N, 116°53'17W is selected for the deployment of the solar based RETs. It has a global resource of 5.86 kWh/m²/day, and Amarillo in Texas, having an average wind speed of 5.9 m/s, was selected as a suitable location for the deployment of wind turbines.

Figure 5.10 shows the annual energy output for the different RETs. The US site shows the highest power outputs for the majority of the RETs, except for power outputs from biomass energy, which are higher in Spain. PV had the lowest annual electrical power output followed by LFR-ORC corresponding approximately to 3800 MWhe and 4600 MWhe, respectively. The Biomass power plant and PT-ORC had the highest electrical output, corresponding to approximately 13200 MWhe and 5400 MWhe, respectively. In general, the annual electricity and thermal energy output for the RETs in the US is higher than the energy output in Spain. Furthermore, the differences in the amounts of energy produced are because of the disparities in the resource potential and the intermittent nature of the energy source. The performance analysis results for the RETs shows that the system can support users demand while allowing the excess energy output to be stored. It is worth mentioning that in this study, the WT is the only technology that does not include any form of stored energy and yet has the third-highest annual electrical energy output.

Despite identical technological configurations, these RETs shows a strong dependence on the availability of the local resource (i.e., wind speed, feedstock, temperature, and irradiance). For example, Figure 5.11 shows the lower LCOE in the US site across the RETs (apart from the Biomass power plant – which remained the same in both locations),

mainly attributed to the bountiful availability of resources and low project installation costs. While the scope of these power plants' individual cost of electricity extends across various price points, the graph illustrates the competitiveness of the various RETs. The LCOE for the US sites typically range from 0.01 \$/kWh to 0.11 \$/kWh.

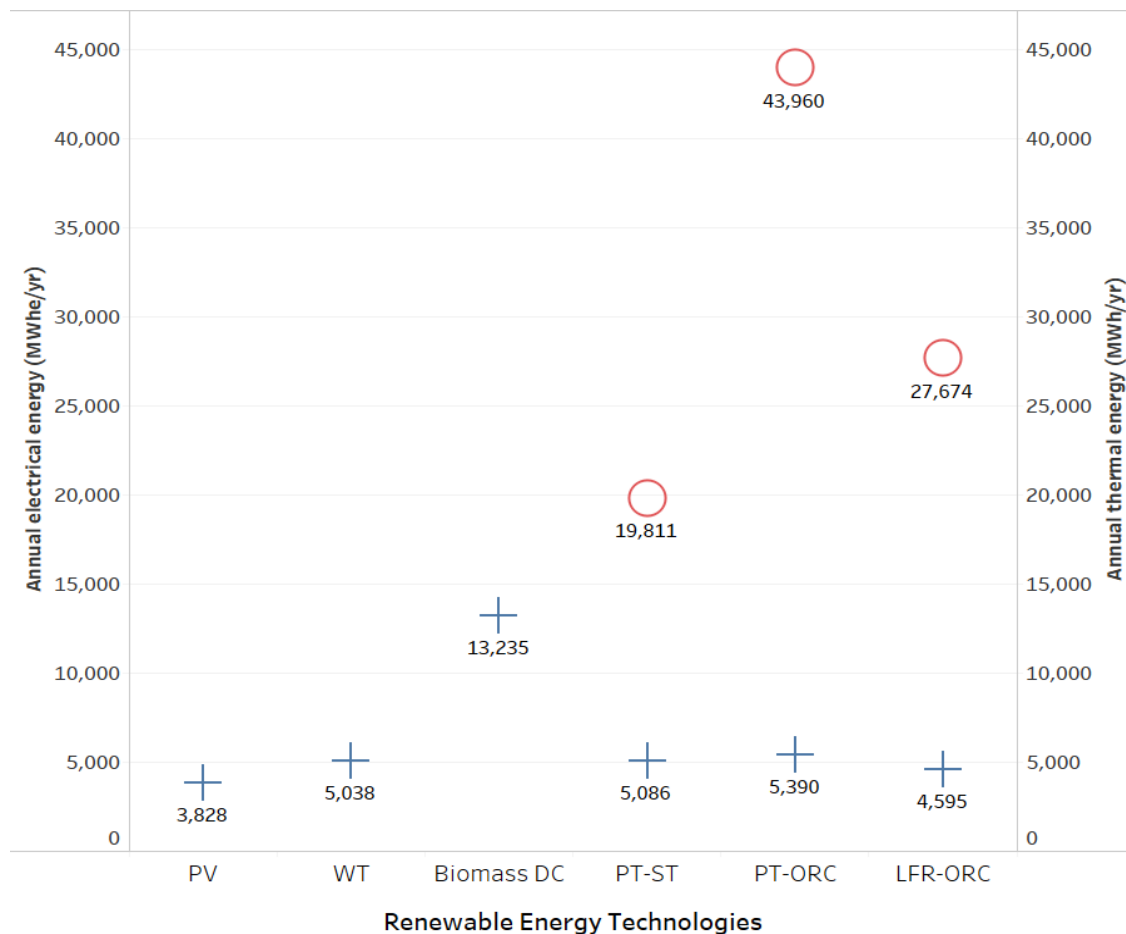


Figure 5.10: Annual energy output from different RETs (Note: left y-axis - Electrical energy only; right y-axis – Total energy, i.e., electrical, and thermal combined, respectively shown as + and O) in the U.S

In the utilization of the LFR-ORC plant, although the LCOE in this study was suggested to be amongst the highest when compared to PV and WT power plants, the energy cost seemed to be justified when the electrical and thermal power outputs are both utilized.

It should be noted that while solar energy is competitive when compared with other renewable sources (i.e., wind energy), the LFR and PT coupled with the organic Rankine cycle still need more technological optimization for better performance and cheaper LCOE.

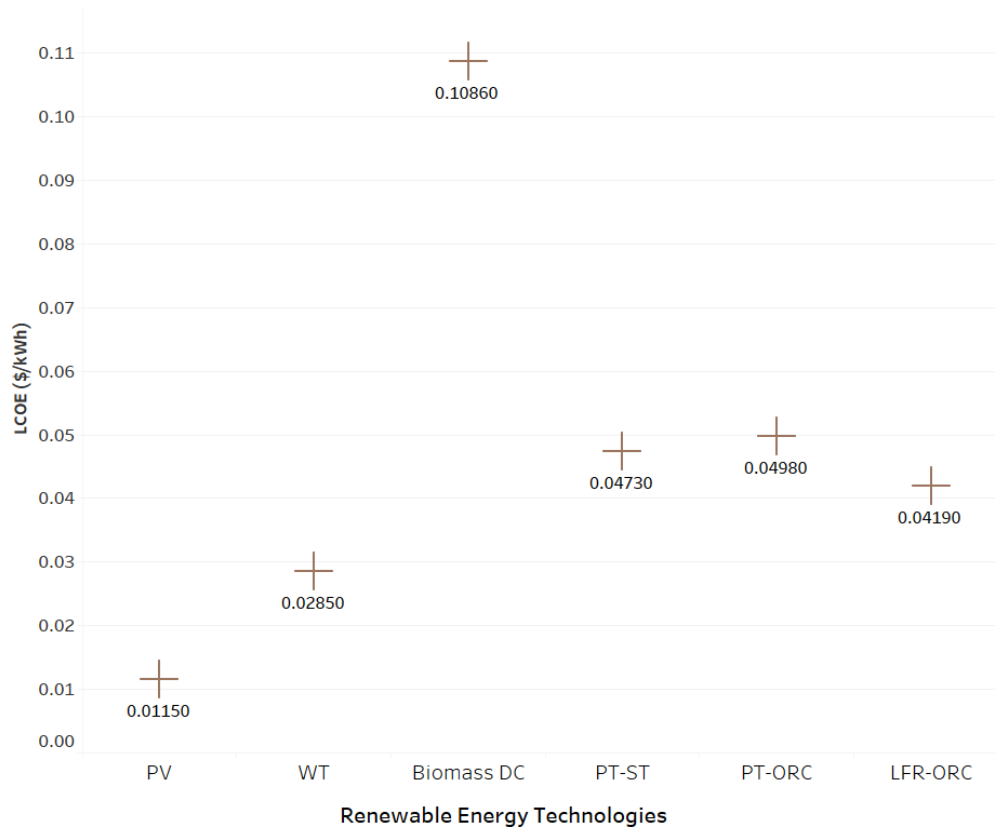


Figure 5.11: Levelised cost of energy for the scoped 2 MW RETs in the U.S

The table below shows the results obtained for other indicator metrics for the RETs, which includes the simple payback time, capacity factor, carbon savings, NPV and the net capital cost.

Table 5.4: Economic indicators of renewable energy technologies in the U.S.

RENEWABLE ENERGY TECHNOLOGY	CAPACITY FACTOR (%)	SIMPLE PAYBACK TIME (YEARS)	TCO2/MWH SAVINGS	NPV (\$)	NET CAPITAL COST (\$)
PV	21.8	1.7	2335.179	13,803,676	4,139,802
WT	28.8	4.8	3073.032	3,213,570	3,078,000
BIOMASS DC	86.5	6	8073.415	445,867	8,228,134
PT-ST	29.1	6.9	3102.484	510,430	11,283,964
PT-ORC	30.8	6.5	3288.072	1,027,819	13,537,489
LFR-ORC	25.1	7	2802.899	151,304	11,482,173

The LFR-ORC system has the highest payback time of 7 years, the lowest NPV of about \$151,304, and the second-highest net capital cost after PT-ORC, which could discourage investors. For the LFR-ORC to be competitive and be an alternative to other renewable energy technologies, there would have to be a technological optimization.

5.1.3. Validation

The simulation results obtained in this research work for the reference RETs plants are compared and validated with both actual and simulated data published by [173, 174].

Table 5.2 shows a comparison of results obtained from this work as well as other published work. Results suggest acceptable variations and confirm that the SAM software is reliable in yielding realistic outputs for the various renewable energy technologies. The SAM model results are likely to be rather conservative, this might be because of the uncertainties with the SAM model inputs.

5.2. Chapter summary

This Chapter has presented the location dependence scenario, results, and analyses of the RETs with user demand. In addition, analysis for the RETs energy output, LCOE, NPV, simple payback time and capacity factor was performed. An environmental perspective on the performance of the RETs was also presented, along with their potential carbon saving per kWh of energy produced. The chapter demonstrated that the choice of RETs site deployment is vital to the performance of the technologies. Overall, the result clearly showed that the RETs deployed in the US had a better techno-economic performance than in Spain. Eco-efficiency assessment provides useful resources for guiding decision towards the consideration of the economic and environmental aspects of a system at the same time. It is noteworthy that this study only considered the conventional ORC system for thermal energy recovery, which warrants further research on more efficient material resource provision and optimisation of the component manufacturing process for thermal energy recovery and storage. New research is also needed to explore innovative measures for end-of-life recovery and reuse of the component materials, which would further improve the environmental performance of the RETs in future.

Chapter 6 Computational fluid dynamics

This Chapter describes principles of computational fluid dynamics (CFD) techniques and the theories applied in the analysis of the heat pipe developed for the application in the solar thermal plant. This chapter contains the governing partial differential equations of conservation of mass, momentum, and energy for the heat pipe. ANSYS Fluent software is used to perform numerical simulations of the operation of the heat pipe. Information on the geometry, meshing and boundary conditions applied are presented in this chapter. Results of the numerical simulation in terms of variations in the liquid and vapour fraction, average temperature, power and mass flow rate of the evaporator and condenser zone of the heat pipe are described. A summary concludes this Chapter.

6.1. Introduction

Computational fluid dynamics (CFD) is the field of science dedicated to the development of numerical solution techniques for a broad range of fluid dynamic problems. CFD also qualitatively and quantitatively predicts the flow of fluid by means of a mathematical model, numerical methods, and software tools [175]. The fluid (liquid and/or gas) flow phenomena can be described by partial differential equations (PDE) representing the law of conservation for mass, momentum, and energy [176]. It provides efficient ways of simulating real fluid flows by replacing PDE systems with a set of algebraic equations, which can be solved using a digital computer, as illustrated in Figure 6.1. The prediction obtained through CFD usually occurs under certain conditions defining the physical properties of the fluid, the geometry, and the boundary and initial conditions of the flow field. In general, the predictions for CFD as a set of values for the flow variable include temperature, pressure, or velocity at any chosen location in the domain. Although CFD is used in a wide range of scientific and engineering applications in various fields of study, it is often used alongside analytical or experimental results [175]. Numerical methods developed to simulate fluid flow include finite element, finite volume, finite difference, and spectral methods [176]. Even though there are significant enhancements in the predictive accuracy and computational time of CFD simulations, common errors such as inaccurate

input data, improper modelling and incorrect boundary condition definition does not allow for exact predictions. In performing meaningful CFD simulations, it is essential to understand the applicability and limitations of the CFD tools as well as the need for assumptions and approximations.

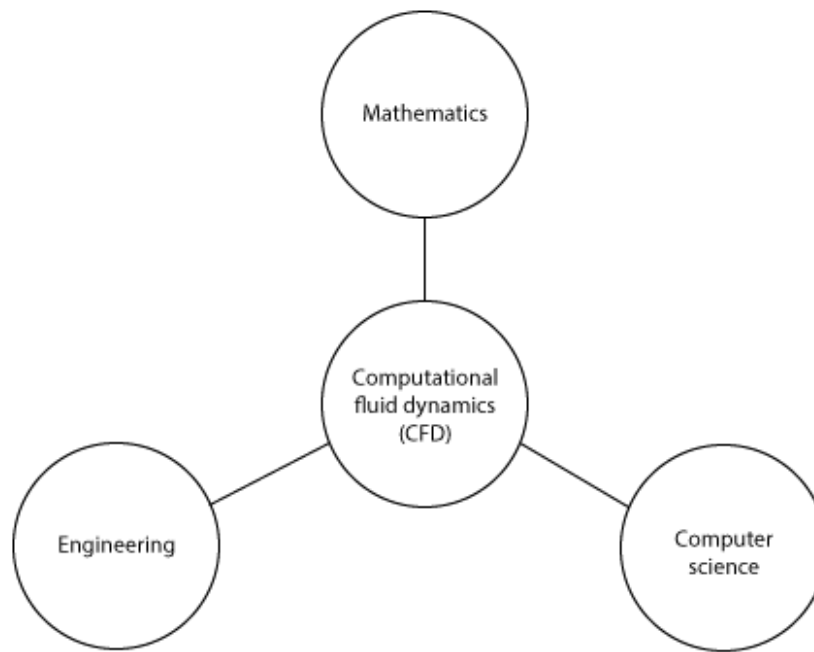


Figure 6.1: The disciplines within CFD

CFD as a research tool is often used for numerical validation of physical processes and in technology designing. The advantages of CFD performing investigations include the following:

- It can permit changes to the input parameters, which otherwise usually lead to time-consuming and expensive physical experimental investigations [177].
- With enough training, the results can be produced inexpensively. However, it is necessary to have some experience interpreting the results.

The accuracy of results obtained by CFD investigations can be limited by numerical errors inherent to digital computations such as truncation error and round-off error. See

[178-180] for more information about CFD. In this study, three different heat pipe orientations are modelled with ANSYS Fluent and validated using scientifically published data.

6.2. Numerical Model description

ANSYS Fluent 2019 R1 software with the built-in volume of fluid (VOF) method has been applied to model the heat pipes with three orientations, namely vertical, horizontal and one inclined at the angle of 45 degrees. The Euler-Lagrange and the Euler-Euler are the two main approaches for numerically calculating multiphase flows. The Euler-Lagrange approach treats the fluid phase, which is the first phase as a continuum and the dispersed phase, such as droplets or bubbles, as the second phase, in which 10% of the volume fraction is not exceeded [181]. Figure 6.2 below describes the process for performing simulation on ANSYS Fluent.

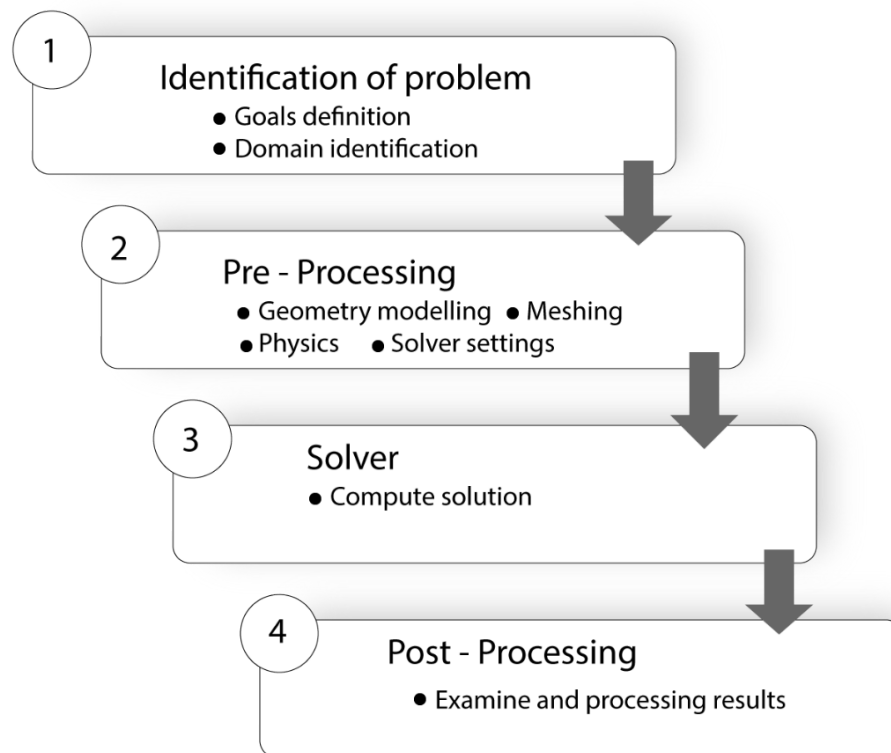


Figure 6.2: Fluent process for performing simulations

6.2.1. Governing equations

The fundamental governing equations of fluid flow are mathematical expressions of physics' conservation laws [182]:

- The fluid mass is conserved.
- Newton's second law states that the rate of change of momentum equals the sum of the forces acting on a fluid particle.
- The first law of thermodynamics states that the rate at which energy changes is equal to the sum of the rate at which heat is added and the rate at which work is done on a fluid particle.

The above conservation laws are applied to the fluid element depicted in Figure 6.3. The six faces are top, bottom, north, south, east, and west, which are denoted by T, B, N, S, E, and W, respectively. The element's centre is located at the position (x, y, z) . The fluid flow equations are derived from the variations in the mass, momentum, and energy of the fluid element caused by fluid flow across its boundaries. Because all fluid properties are functions of space and time, densities, pressures, temperatures, and velocity vectors must be written as, $\rho(x, y, z, t)$, $T(x, y, z, t)$, and $u(x, y, z, t)$ [182].

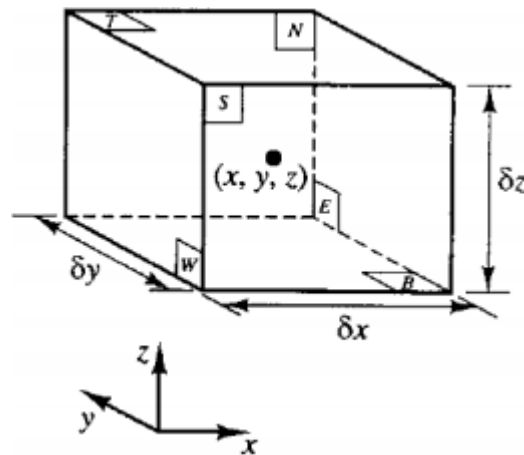


Figure 6.3: The fluid element for demonstration of conservation laws [182]

6.2.1.1. *Continuity or mass conservation equation*

The law of mass conservation states that the mass of fluid in a controlled volume will be determined by operating conditions and the mass of fluid entering and leaving the volume. The controlled system is capable of morphing but not of being destroyed. Continuity partial differential equation in its general form can be written as follows:

$$\frac{\partial \rho}{\partial t} + \nabla \cdot (\rho \vec{v}) = S_m \quad (6.1)$$

where:

$$\nabla = \frac{\partial}{\partial x} + \frac{\partial}{\partial y} + \frac{\partial}{\partial z} \quad (6.2)$$

In equation 6.1, S_m is the source and it denotes the mass added to the continuous phases by the water-liquid phases and any other sources defined by the user (via User Defined Functions UDFs).

6.2.1.2. *Momentum conservation equation*

Newton's second law states that the rate at which a fluid particle's momentum changes equals the sum of the forces acting on it. There are two types of forces that act on fluid particles, in this case: body forces (gravitational, centrifugal, and electromagnetic) and surface forces (pressure, viscous, shear and normal). The rate of increase of a fluid particle's (x, y, z) momentum per unit volume is given by:

$$\rho \frac{Du}{Dt}, \quad \rho \frac{Dv}{Dt}, \quad \rho \frac{Dw}{Dt}$$

The overall effect of the body forces is determined by the source terms S_{Mx} , S_{My} , and S_{Mz} of the momentum equation's x , y , and z – components. The momentum conservation equation can be written as follows based on this principle [182].

By setting the rate of change of x-momentum of the fluid particle equal to the total force in the x-direction on the element, the x-component can be found due to surface stress. Equation 6.3 is the formulation for the rate of increase of x-momentum.

$$\rho \frac{Du}{Dt} = -\frac{\partial p}{\partial x} + \frac{\partial \tau_{xx}}{\partial x} + \frac{\partial \tau_{yx}}{\partial y} + \frac{\partial \tau_{zx}}{\partial z} + S_{Mx} \quad (6.3)$$

The formulation of the momentum equation for the y-component is given in equation 6.4.

$$\rho \frac{Dv}{Dt} = -\frac{\partial p}{\partial y} + \frac{\partial \tau_{xy}}{\partial x} + \frac{\partial \tau_{yy}}{\partial y} + \frac{\partial \tau_{zy}}{\partial z} + S_{My} \quad (6.4)$$

Similarly, the z-component of the momentum equation is given in equation 6.5.

$$\rho \frac{Dw}{Dt} = -\frac{\partial p}{\partial z} + \frac{\partial \tau_{xz}}{\partial x} + \frac{\partial \tau_{yz}}{\partial y} + \frac{\partial \tau_{zz}}{\partial z} + S_{Mz} \quad (6.5)$$

6.2.1.3. Energy equation

The energy equation is derived from Newton's first law, which states that the rate at which energy changes inside a fluid element is equal to the rate at which heat is added to it and the work done on it [183]. The energy equation is as follows:

$$\frac{\partial}{\partial t}(\rho E) + [\vec{v}(\rho E + p)] = \nabla \left[k_{eff} \nabla T - \sum_j h_j \vec{J}_j + (\overline{\tau_{eff}} \times \vec{v}) \right] + S_h \quad (6.6)$$

Here k_{eff} represents the effective conductivity, S_h represents the volumetric heat sources and the heat chemical reaction the are defined by the user and \vec{J}_j represents the diffused heat flux of species j .

$$E = h - \frac{p}{\rho} + \frac{v^2}{2} \quad (6.7)$$

The sensible enthalpy h for an ideal gas is defined by

$$h = \sum_j Y_j h_j \quad (6.8)$$

For incompressible gas flow as:

$$h = \sum_j Y_j h_j + \frac{p}{\rho} \quad (6.9)$$

6.2.2. Multiphase model

In multiphase flows, a phase can be defined as a distinct class of material that exhibits a distinct inertial response to and interaction with the flow and potential field in which it exists. Multiphase liquid-vapour flows are frequently described as a bubbly, slug, stratified, annular, or stratified wavy [183]. Figure 6.4 illustrates the flow regimes.

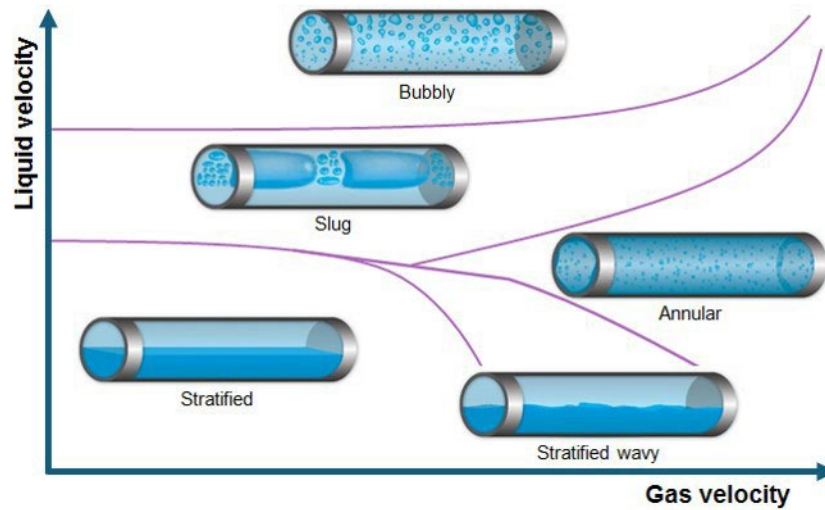


Figure 6.4: Illustration of flow regimes [184]

For multiphase flows, numerical solutions based on the finite volume modelling approach are more complex than single-phase flows. The complexity of multiphase flow arises from the fact that the interfaces between phases are not constant, and physical properties such as viscosity and density change at the interfaces between the vapour and liquid phases, necessitating extensive computation. Since the volume of a phase cannot be occupied by other phases, the concept of phasic volume was introduced. It was assumed that phasic volumes were continuous functions of space and time with a sum of one. The three methods available in the Euler-Euler model are the Volume of Fluid (VOF), the Mixture method, and the Eulerian method. The Eulerian multiphase model was omitted due to problematic convergence behaviour limiting the complexity of a solution.

6.2.3. Volume of Fluid (VOF) model

The volume of fluid (VOF) method is used to compute possible solutions to this problem by evaluating the motion of all the phases and indirectly determining the motion of the interfaces from the results. The VOF technique is used to model two immiscible fluids with a clearly defined interface between the phases. It is also used to perform surface tracking on a fixed mesh. The VOF model solves a single set of Navier–Stokes’s equations across the computational domain and uses the volume fraction of each phase to track the motion of the different phases [185]. The VOF model is based on the fact that each cell in the domain is occupied by either one or both phases. In other words, if α_v is a vapour volume fraction and α_L is a liquid volume fraction, the following three conditions are possible:

- $\alpha_L = 0$: Vapour fully occupies the cell
- $\alpha_L = 1$: Liquid fully occupies the cell
- $0 < \alpha_L < 1$: The cell interface is between the vapour and liquid phases

6.2.4. Mass and heat transfer during the evaporation and condensation processes

The mass transfer mechanism for phase interaction between vapour and liquid species

was investigated using the evaporation-condensation mechanism based on fluid saturation properties as well as a user-defined function (UDF). The evaporation-condensation model is a systematic model [186] with a physical foundation that solves mass transfer problems using the temperature regimes.

The Lee model [187] is a simplified saturation model for condensation and evaporation processes. The intensity of the phase change is proportional to the temperature difference between the saturation temperature (T_{sat}) and temperature inside the domain. The model assumes that the volumetric mass transfer is expressed by the following patterns [188].

Lee model during evaporation

$$If \quad T_{mix} > T_{sat} \quad \dot{m}_{e \rightarrow v} = coeff \times \alpha_l \rho_l + \left(\frac{T_{mix} - T_{sat}}{T_{sat}} \right) \quad (6.14)$$

Lee model during condensation

$$If \quad T_{mix} < T_{sat} \quad \dot{m}_{e \rightarrow v} = coeff \times \alpha_v \rho_v + \left(\frac{T_{mix} - T_{sat}}{T_{sat}} \right) \quad (6.15)$$

The rate of mass transfer from liquid to vapour phase is represented by $\dot{m}_{e \rightarrow v}$, where α and ρ are the volume fraction phase and density, $coeff$ is a coefficient that needs to be fine-tuned and can be interpreted as a relaxation time and T_{mix} and T_{sat} are mixture and saturation temperatures, respectively.

Equations 6.14 and 6.15 are basic Lee model equations, but it takes into account the change in the intensity of the phase transition and prevents the dryout phenomenon by correcting the relaxation coefficient $coeff$

The UDF is primarily used to “calculate mass and heat transfer between the water-liquid and water-vapour phases during the evaporation and condensation processes, as determined by the source terms in the governing equations”, most notably the continuity and energy equations. Furthermore, temperature T_{mix} introduced in Equations 6.14 and

6.15 is the mixture temperature rather than a water-liquid or water-vapour temperature. As previously stated, the VOF model associates certain variables such as temperature and velocity with the mixture phase rather than with a particular phase.

6.2.5. Turbulence model

The standard $k-\epsilon$ transport model [189] was used to define the turbulence kinetic energy and flow dissipation rate within the model [190]. The standard $k-\epsilon$ transport model has been used previously on cylindrical pipe flows [191, 192], as has the approach of integrating Eulerian-Eulerian multiphase simulations alongside [193]. The kinetic energy k of turbulence, and its rate of dissipation, ϵ , are calculated using the following transport equations, formulated in equations 6.16 and 6.17.

$$\frac{\partial}{\partial t}(\rho k) + \frac{\partial}{\partial x_i}(\rho k u_i) = \frac{\partial}{\partial x_j} \left[\left(\mu + \frac{\mu_t}{\sigma_k} \right) \frac{\partial k}{\partial x_j} \right] + G_k + G_b - \rho \epsilon - Y_M + S_k \quad (6.16)$$

$$\frac{\partial}{\partial t}(\rho \epsilon) + \frac{\partial}{\partial x_i}(\rho \epsilon u_i) = \frac{\partial}{\partial x_j} \left[\left(\mu + \frac{\mu_t}{\sigma_\epsilon} \right) \frac{\partial \epsilon}{\partial x_j} \right] + C_{1\epsilon} \frac{\epsilon}{k} (G_k + C_{3\epsilon} G_b) - C_{2\epsilon} \rho \frac{\epsilon^2}{k} + S_\epsilon \quad (6.17)$$

where G_k is the turbulence kinetic energy generation as a result of mean velocity gradients, the turbulence kinetic energy generation due to buoyancy is given by G_b . σ_ϵ and σ_k are turbulent Prandtl numbers for ϵ and k . $C_{1\epsilon}$, $C_{2\epsilon}$ and $C_{3\epsilon}$ are constants. The user defined source terms are S_ϵ and S_k .

6.3. The example of the Computation Domain creation

The custom-designed heat pipe geometry was created to enable both numerical simulations and experimental validation. Figure 6.5 below shows its geometric parameters.

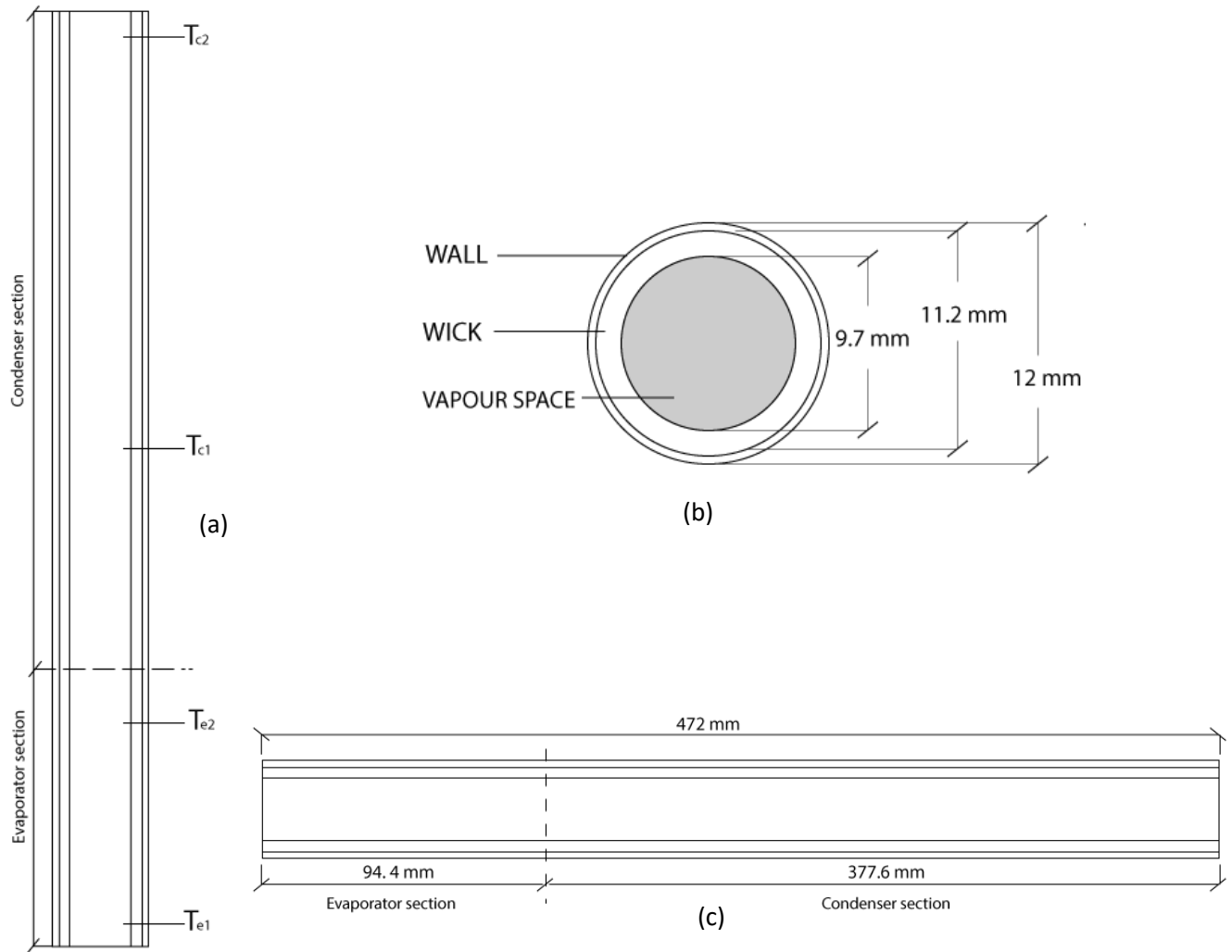


Figure 6.5: Heat pipe geometry (a) Average temperature recorder sections (b) diameter of different parts (c) length of evaporator and condenser section

To simulate the two-phase flow and heat transfer phenomena in the heat pipe, a three-dimensional model was developed. The closed tube copper heat pipe geometry has a total length of 472 mm with an outer diameter (wall) of 12 mm, the porous wick diameter is 11.2 mm, and the vapour space diameter is 9.7 mm, as illustrated in Figure 6.5 (b) and (c). The heat pipe is divided into the evaporator and condenser sections with lengths of 94.4 mm and 377.6 mm, respectively. The average temperature distribution along the heat pipe's outer wall was monitored at four locations, as shown in Figure 6.5 (a). T_{e1} and T_{e2} are used to measure the average temperature distribution in the evaporator section,

and T_{c1} and T_{c2} are used to measure the average temperature distribution in the condenser section.

6.4. Mesh generation

Mesh generation is a critical process during CFD simulation. The mesh quality has a significant impact on the accuracy and stability of the solution. A mesh or grid is a representation of an object's continuous physical surface and volume using discrete x, y, and z coordinates. Each cell constitutes a control volume, and a group of all cells make up the physical/computational domain. A cell's boundary is referred to as a face, whereas a face's boundary is referred to as an edge. Figure 6.6 illustrates common terminologies associated with two- and three-dimensional computational domains.

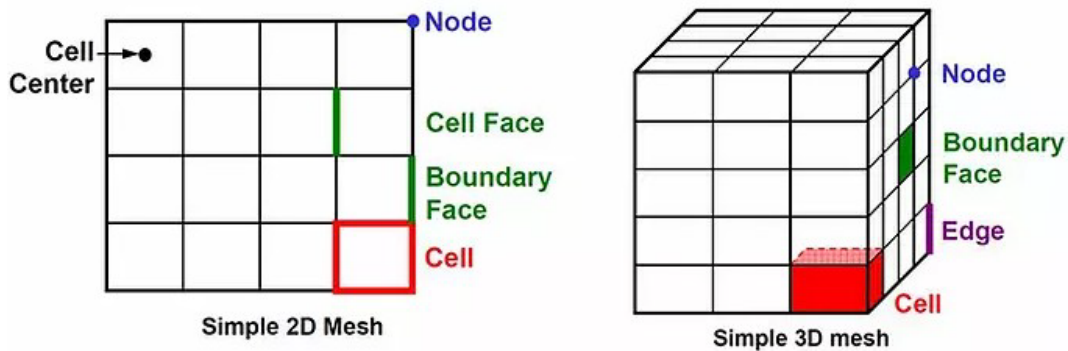


Figure 6.6: 2D and 3D computational domain general terminologies

Unstructured meshes are not required to have an equal number of adjacent elements at each interior vertex and thus allow any number of elements to meet at a single vertex.

The mesh was generated on the basis of the geometry in Figure 6.5. All dimensions were kept as in reality as developed by Thermacore. The mesh was created using ANSYS [153]. As a result of time constraints, independent studies on the different heat pipe orientations were not performed. Thus, a mesh having an aspect ratio of 1 was used. The generated mesh (Figures 6.7 and 6.8) comprises of 403,627 nodes and 388,620 hexahedral elements.

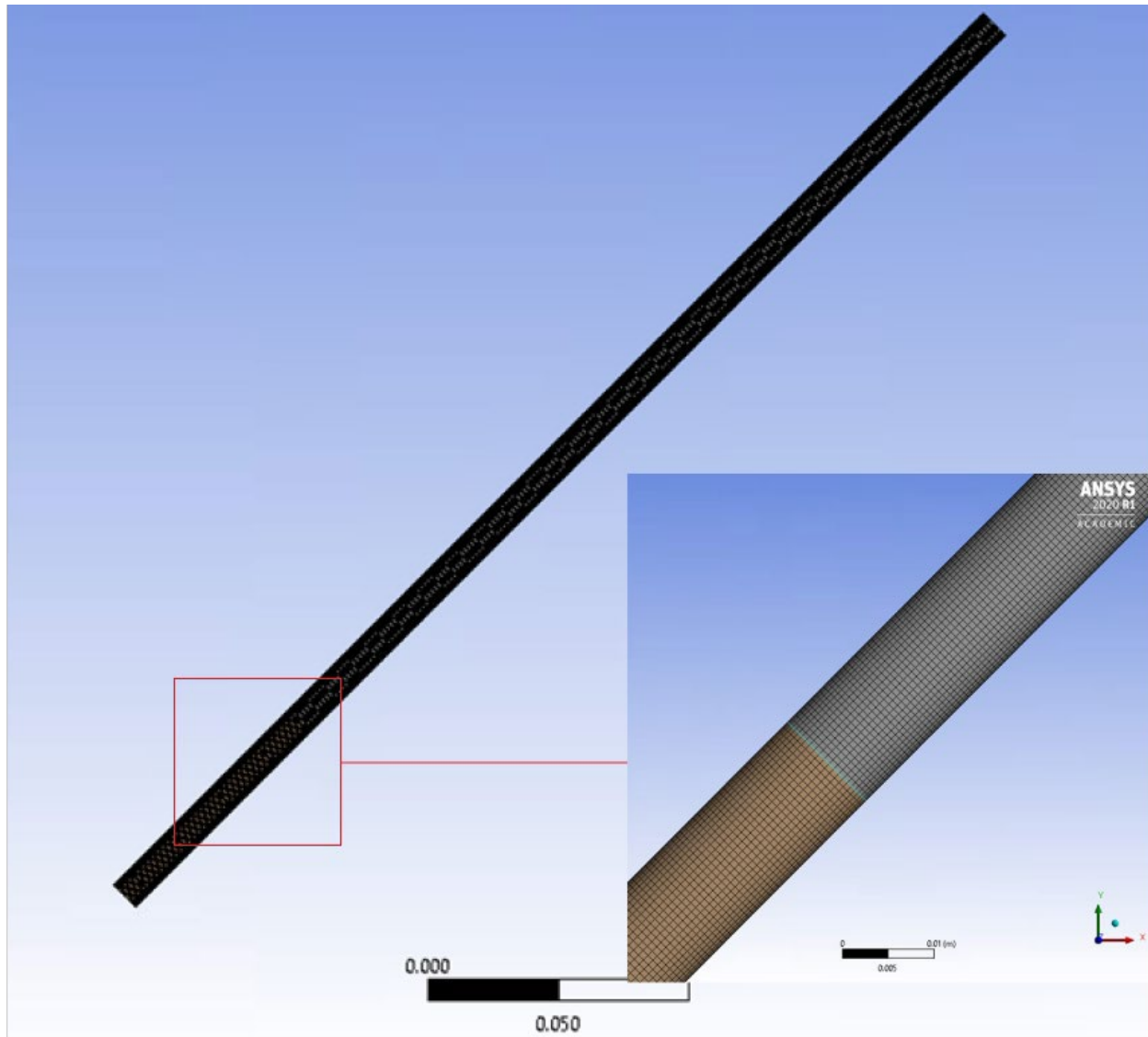


Figure 6.7: Mesh generation for the 45 degrees heat pipe showing the evaporator and condenser sections

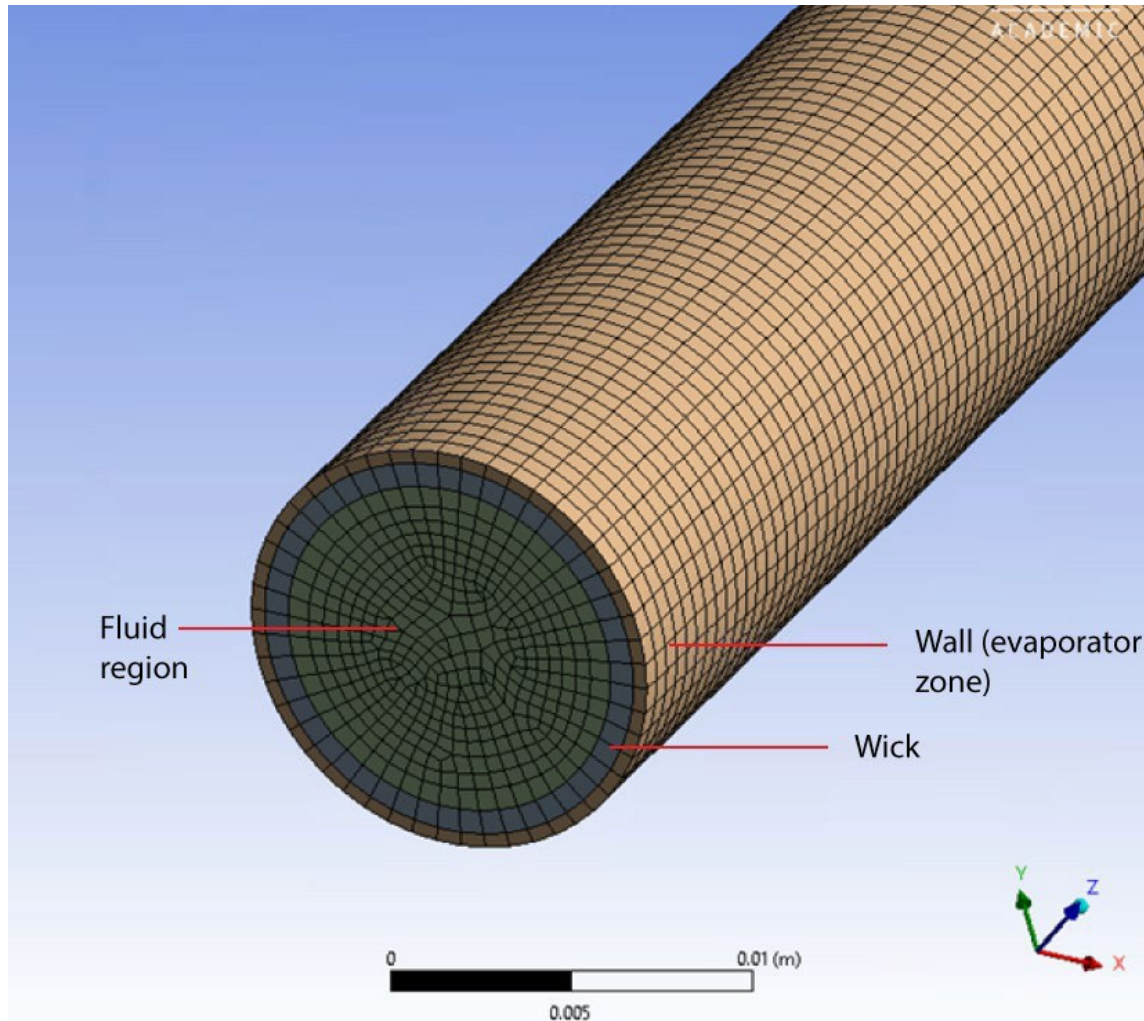


Figure 6.8: Mesh generation on the geometry surface

6.5. Boundary conditions applied in modelling heat pipes

To simulate heating and evaporation, a constant temperature is defined at the evaporator and condenser section wall boundaries. The condenser section is cooled to dissipate the heat generated by vapour condensation. According to the experimental apparatus, it is assumed that the condenser is cooled by water. As a result, the convection heat transfer coefficient is defined as the boundary condition on the condenser's wall. The following formula was used to calculate the corresponding heat transfer coefficients:

$$h_c = \frac{Q_c}{2\pi r L_c (T_{c,av} - T_\infty)} \quad (6.18)$$

Here h_c represents the heat transfer coefficient in the condenser, the rate of heat transfer from the condenser is represented by Q_c . L_c represents the condenser height, T_∞ and $T_{c,av}$ are the average temperature of the condenser and average temperature in the cooling water, respectively. Water was used as the working fluid in this model, with a fill ratio of 15%. The boundary conditions parameters, solution settings, general, operational, and material conditions for the heat pipes are given on APPENDIX B.

6.6. Convergence criterion

A transient simulation with a time step of 0.0005 s is used to model the two-phase flow dynamic behaviour. The time step was chosen based on the Courant number, which is the ratio of the time step to the time required for fluid to pass through a cell. The maximum Courant number permitted near the interface for VOF models is 250. The Courant number is less than three for a time step of 0.0005. After approximately 12 minutes, the simulation reaches a steady state. This model incorporates a SIMPLE algorithm for pressure–velocity coupling and a first-order upwind scheme for momentum and energy determination. Geo-Reconstruct and PRESTO discretization are also used in the simulation for the volume fraction and pressure interpolation schemes, respectively.

The primary phase is defined as water-vapour, while the secondary phase is defined as water-liquid. The boiling point temperature of 373 K is used to calculate mass and heat transfer during the evaporation and condensation processes, and the latent heat of vapourisation used in the UDF code is given in Equation 6.19. The simulation begins by heating the liquid pool in the evaporator. Evaporation begins, and phase change occurs when the saturation temperature (373 K) is reached. The saturated vapour is then elevated to the condenser, where it condenses along the cold walls, forming a thin liquid film.

$$L_{hv} = -0.0614342 \times T^2 \times T + 1.58927 \times T^2 - 2364.18 \times T + 2500790 \quad (6.19)$$

6.7. Chapter summary

This Chapter discussed the numerical methodology used in this study for CFD modelling of the heat pipe. Following the presentation of the governing equations, the computational model and heat transfer equations used in the investigation were discussed. The numerical model used in this study and the governing equation was described in detail, as was the geometry used to simulate the flow with coupled heat and mass transfer analysis. Additionally, the boundary conditions that were used to conduct all the analysis on the computational domain were defined. In summary, this chapter described the methodology used to generate the physical domain for the heat pipe geometry and to apply boundary conditions to numerical simulations to predict the performance of heat pipes within the computational domain.

Chapter 7 CFD Modelling Results and Discussion

This Chapter presents results obtained from the CFD simulation performed for the different heat pipe tilt angles. Experimental results from the literature are compared with the results obtained from the CFD modelling to validate the present model. A summary concludes the Chapter.

7.1. Simulations method for different tilt angles of the heat pipe

In this section, the results for the three different heat pipe orientations were considered, namely 90° (vertical), 45° and 0° (horizontal) tilt angles, as illustrated in Figure 7.1, are presented.

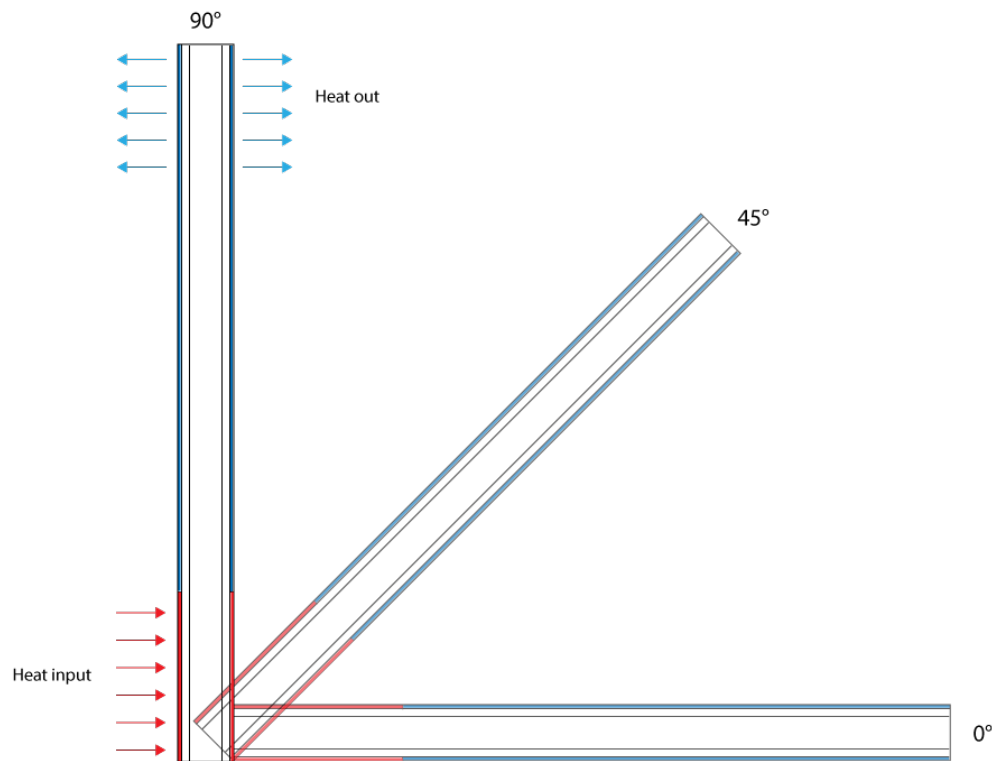


Figure 7.1: Three heat pipe orientations

In determining changes in the saturated liquid temperature $T_l(t)$, a transient temperature profile is achieved using a lumped capacitance model³ applied to the entire heat pipe, as

described in [103]. Thus, when considered uniform, the saturated liquid temperature in the transport section was equal to both the vapour and operating temperatures of the heat pipe. The heat pipe begins at ambient temperature by imposing a constant heat flux q'' (in this study, the constant temperature) on the evaporator section and cooling the condenser section exclusively via convection. The overall heat pipe's lumped capacitance model is expressed as:

$$(\rho c V)_{tot} \frac{dT_l(t)}{dt} = q'' A_e - h_c A_c [T_l(t) - T_\infty], \quad (7.1)$$

The overall heat capacity of the heat pipe is represented by $(\rho c V)_{tot}$, which accounts for the thermal energy storage terms of the wick, wall and working fluid. The outer surface of the evaporator and condenser is represented by A_e and A_c , respectively. As a starting point, the saturated liquid temperature is set to

$$T_l(0) = T_\infty \quad (7.2)$$

Using a mass balance of a liquid layer on a non-material control volume the velocity of the liquid front can $d\varepsilon/dt$ be expressed as a function of the difference between the average velocity U_o at the evaporator section entrance and the liquid layer vaporization rate from horizontal and vertical surfaces such that

$$\frac{d\varepsilon}{dt} = U_o - \frac{\dot{m}_{evap}}{\rho_l h w}, \quad (7.3)$$

in the case, h is the depth and w is the width of a rectangular groove.

³ The lumped capacitance model is an analysis that reduces thermal systems to several discrete lumps with an assumption that inside each lump, temperature difference is negligible.

The liquid in the wet region will evaporate when heat flux is applied to the evaporator wall evaporate. Volumes in the dry and wet region are controlled and defined as moving non-material control volumes.

There are three assumptions considered in the dry region, i) there is no heat loss from the wall to the vapour, ii) one-dimensional heat conduction in x is considered, and iii) the integral energy balance on the control volume in the dry region and the constant wall properties (ρ_w , c_w , and k_w) is given by

$$\rho_w c_w \int_{\varepsilon(t)}^{L_e} \frac{\partial T_w}{\partial \tau} dx = -q_3'' + \int_{\varepsilon(t)}^{L_e} \frac{q''}{\delta} dx \quad (7.4)$$

where the groove wall thickness is δ and q_3'' is the net heat flux conducted through the wall. By Fourier's Law the dry to the wet region at the location $x = \varepsilon(t)$ is expressed as

$$q_3'' = k_w \left. \frac{\partial T_w}{\partial x} \right|_{x=\varepsilon(t)} = - \int_{\varepsilon(t)}^{L_e} \frac{\partial}{\partial x} \left(k_w \frac{\partial T_w}{\partial x} \right) dx. \quad (7.5)$$

Combining Equations (7.4) and (7.5) and rearranging yields

$$\int_{\varepsilon(t)}^{L_e} \left(\frac{1}{\alpha_w} \frac{\partial T_w}{\partial t} - \frac{\partial^2 T_w}{\partial x^2} - \frac{q''}{k_w \delta} \right) dx = 0. \quad (7.6)$$

Equation 7.6 is valid for the length of any dry wall,

At $t > 0$ and for $\varepsilon(t) < x < L_e$,

$$\frac{1}{\alpha_w} \frac{\partial T_w}{\partial t} = \frac{\partial^2 T_w}{\partial x^2} + \frac{q''}{k_w \delta}. \quad (7.7)$$

The boundary conditions are given as:

At $x = L_e$,

$$\left. \frac{\partial T_w}{\partial x} \right|_{x=L_e} = 0, \quad (7.8)$$

At $x = \varepsilon(t)$,

$$T_w(\varepsilon, t) = T_l(t), \quad (7.9)$$

where Equation (7.8) ensures that the heat pipe's far end is insulated, and Equation (7.9) specifies that the liquid front temperature is equal to the saturated liquid temperature and the initialisation condition is set such that

$$T_w(x, 0) = T_l(0) \quad (7.10)$$

The assumptions in the wet region are as follows, i) the temperature along the wall groove is constant and equal to the saturated liquid temperature T_l , and ii) compared to the wall thickness δ , the liquid thickness h is small.

$$\int_0^{\varepsilon(t)} \frac{d[(\rho c)_{eff} T_l]}{dt} dx = q_3'' + \int_0^{\varepsilon(t)} \frac{q''}{\delta} dx - \int_0^{\varepsilon(t)} \frac{\dot{m}_{evap}'' H_{fg}}{\delta} dx, \quad (7.11)$$

where the effective heat capacity, which is a liquid-wall combination in the evaporator's wet region is represented as $(\rho c)_{eff}$.

For groove wicks, $(\rho c)_{eff} = \rho_w c_w + \rho_l c_l (h/\delta)$. Equation (7.11) rearranges,

At $t > 0$ and for $0 < x \leq \varepsilon(t)$,

$$\frac{\dot{m}_{\text{evap}} H_{fg}}{\delta} = k_w \frac{\partial^2 T_w}{\partial x^2} + \frac{q''}{\delta} - \frac{d[(\rho c)_{\text{eff}} T_l]}{dt}, \quad (7.12)$$

integrating between $x = 0$ and $x = \varepsilon(t)$ and establishing that in the wall of the adiabatic section, heat is conducted, it follows that

$$\frac{\dot{m}_{\text{evap}} H_{fg}}{\delta w} = k_w \left. \frac{\partial T_w}{\partial x} \right|_{x=\varepsilon(t)} + \frac{q''}{\delta} \varepsilon(t) - \frac{d[(\rho c)_{\text{eff}} T_l]}{dt} \varepsilon(t). \quad (7.13)$$

Equation (7.13) shows that in the liquid front interface, the heat is delivered by the wall is equal to the latent heat absorbed by the vaporizing liquid.

q''_{eff} as shown in Equation (7.14) for effective heat flux is the difference between the heat flux input and stored thermal energy in the evaporator wet region

$$q''_{\text{eff}} \triangleq q'' - \frac{d[(\rho c)_{\text{eff}} T_l]}{dt} \delta, \quad (7.14)$$

and combining Equation (7.13) with Equations (7.3) and (7.14), the liquid front location is determined by.

$$\left. \frac{\partial T_w}{\partial x} \right|_{x=\varepsilon(t)} = \frac{\rho_l h H_{fg}}{k_w \delta} \left(U_0 - \frac{d\varepsilon(t)}{dt} - \frac{q''_{\text{eff}}(t) \varepsilon(t)}{\rho_l h H_{fg}} \right). \quad (7.15)$$

By assuming a saturated liquid, the initial condition is set in the groove such that

At $t = 0$,

$$\varepsilon(0) = L_e. \quad (7.16)$$

A numerical solution is required for the transient heat conduction problem associated with the time-varying boundary condition (Equation 7.5) and initial conditions (Equations 7.9 and 7.10).

The evaporator length was divided into N small elements using a fully implicit finite difference scheme with a fixed mesh grid. Due to the presence of the sharp liquid front condition (Equation. 7.5), the liquid front's position was determined using an implicit backward Euler method (1st-order in time and 2nd-order in space).

7.2. Examples of CFD results with visualisation of processes in the heat pipes

The water-vapour fraction moves from the heating section to the cooling section due to the density difference, whereas the cooling section is used for condensing the vapour and returning the liquid to the heating section due to gravity and/or the force of capillary action in the wick structure. Due to the gravitational effect, changing the orientation of the heat pipe from 0° to 90° significantly increases the flow of liquid to the evaporator section. This also results in a decrease in heat transfer in the outward direction and an increase in the heat pipe's thermal resistance.

The example in the variation of the water-liquid volume of fraction in the evaporator and condenser region for the vertical heat pipe for a constant heat input temperature of 333.15 K are shown in Figure 7.2 for the first 12 seconds of operation.

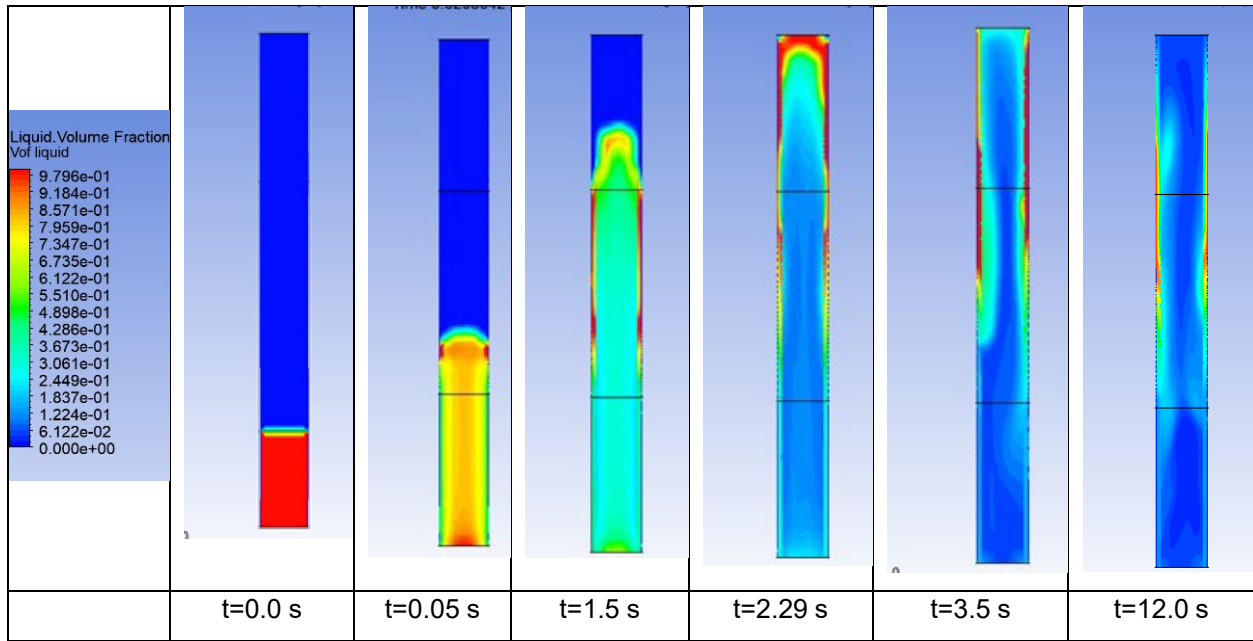


Figure 7.2: Boiling process in the wicked heat pipe for temperature heat input of 333.15 K

The presence of only liquid (water-liquid volume fraction = 1) is shown by a red colour, while the presence of only vapour (water-vapour volume fraction = 0) is depicted by blue colour. At the start of the process (when $t = 0.0$ s) the water-liquid pool in the evaporator initially occupies 15% of the total heat pipes' volume. When the liquid reaches the boiling point, it begins to evaporate, and phase change occurs. The continuous liquid evaporation results in a decrease in the volume fraction of liquid and an increase in the volume fraction of the vapour. The saturated vapour is then transported upwards to the condenser zone. When the vapour reaches the condenser's wall, where a boundary condition for the heat rejection is specified, the vapour condenses along the condenser walls. This liquid then returns by the aid of capillary action through the wick to the evaporator section and replenishes the liquid pool to maintain the evaporator-condensation process.

Figure 7.3 below shows an example of variation in the liquid volume of fraction for the horizontally mounted heat pipe, in which the 300-W heat input rate is specified on the outer wall of the evaporator. It can be observed that with a constant heat flux input of 300

W, the water-liquid fraction (blue colour) at the bottom of the heat pipe rapidly dries out after about 150 seconds.

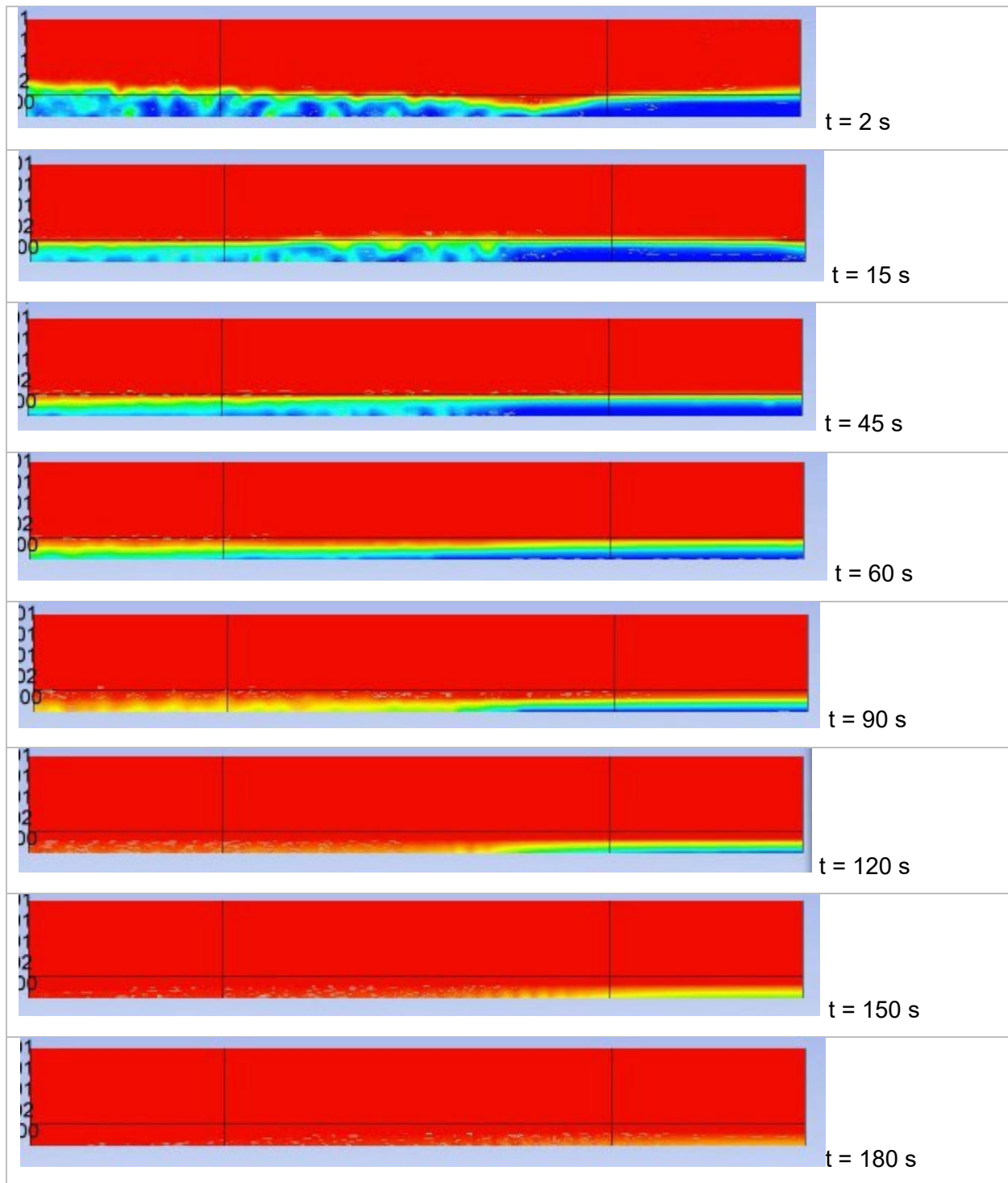


Figure 7.3: Vapour volume fraction of horizontal heat pipe with 300 W constant heat input

7.3. CFD results for the Thermacore heat pipe (for application in a solar thermal plant)

CFD simulations of the heat pipe operation, described in Figure 6.5, were conducted, and results on the variations of fluid and vapour fractions and temperatures inside the heat pipe as functions of time are presented in Figures in Appendices B2 and B3, respectively.

After approximately twenty minutes elapsed in numerical simulations, the evaporation and condensation processes in the heat pipe reach a quasi-steady state⁴.

The total simulation time of the heat pipe was 60 mins. The input temperature was varied from 303.15 K to 393.15 K at the evaporator section and set to 293.15 K at the condenser section. Figures 7.4 – 7.6 show the plots for the input temperature at 303.15 K of the heat input and output rates (evaporator and condenser sections) and volume fractions of liquid and vapour for three tilt angles of the heat pipe. As it can be seen in Figures 7.4 and 7.5 the energy conversion principle is observed in the solution of governing equations describing the operation of the heat pipe: the amount of heat absorbed in the evaporation zone is rejected in the condensing zone. For the above-specified boundary conditions, the heat transfer rate is the highest for the vertically mounted heat pipe (57 W), followed by the heat pipe with 45° tilt angle (45 W). The horizontal heat pipe demonstrates the lowest heat transfer rate at 34.5 W.

In Figure 7.5, the red coloured line illustrates the presence of the water-vapour fraction, and the blue coloured line indicates the water-liquid fraction of the volume. At initialisation, 15% of the total internal volume of the heat pipe is filled with liquid (as shown in APPENDIX B1). With a constant heat input rate, the simulation reached a steady regime of operation in approximately 20 minutes. From the 20th minute to the 60th minute, it can be observed that the water-liquid and water-vapour volume fraction formed opposite sinusoidal waves indicating evolution in the evaporation and condensation processes.

Figures 7.7 and 7.8 show the corresponding results for the heat input and output rates on the evaporator and condenser sections of the heat pipe for the case in which the temperature level at the evaporator is increased to 333.15 K, and the condenser

⁴ Quasi-steady state refers to a situation that does not change rapidly enough that it can be deemed constant.

temperature is left unchanged at 293.15 K. It can be seen that the heat transfer rates increased to about 85, 79 and 74 W for the vertical, tilted and horizontal heat pipe, respectively.

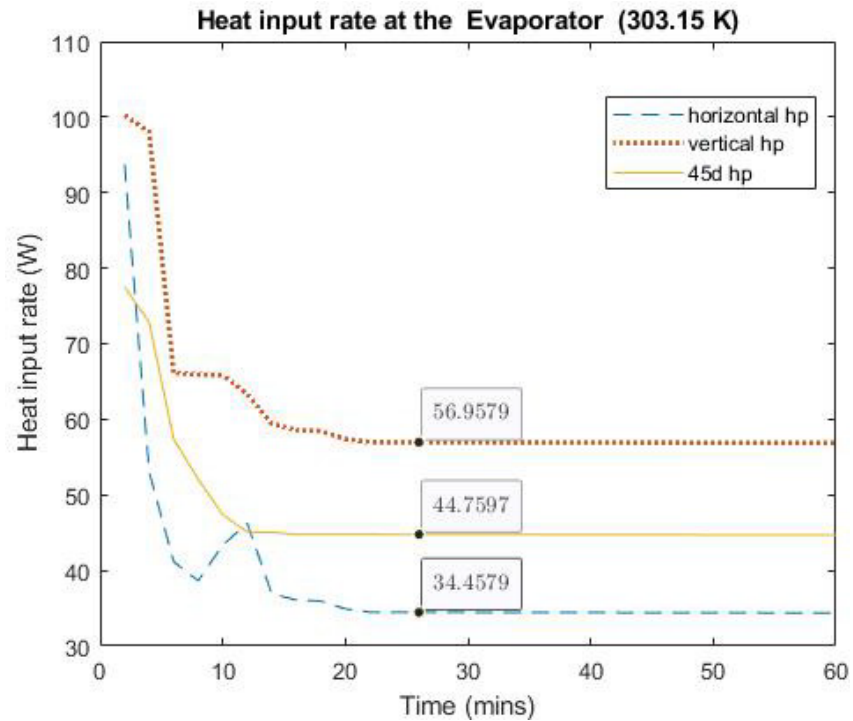


Figure 7.4: Heat input rate in the evaporator for the temperature of the evaporator at 303.15 K

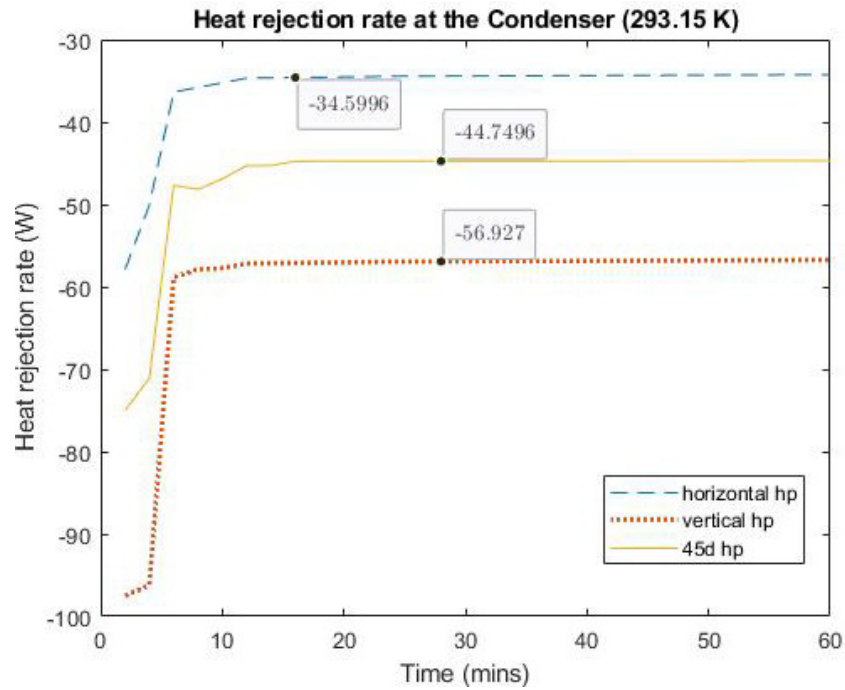


Figure 7.5: Heat rejection rate in the condenser for the temperature of the evaporator at 303.15 K

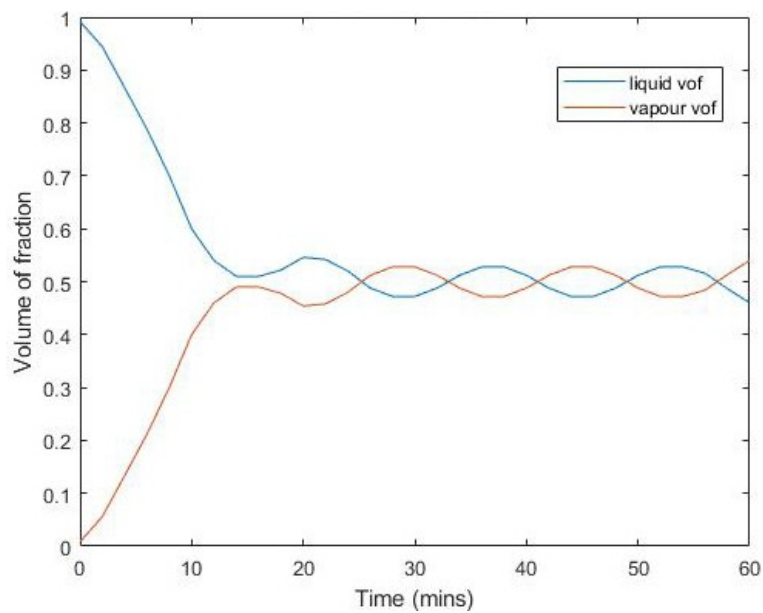


Figure 7.6: Variation of the liquid and vapour volume of fraction as a function of time (without dry-out)

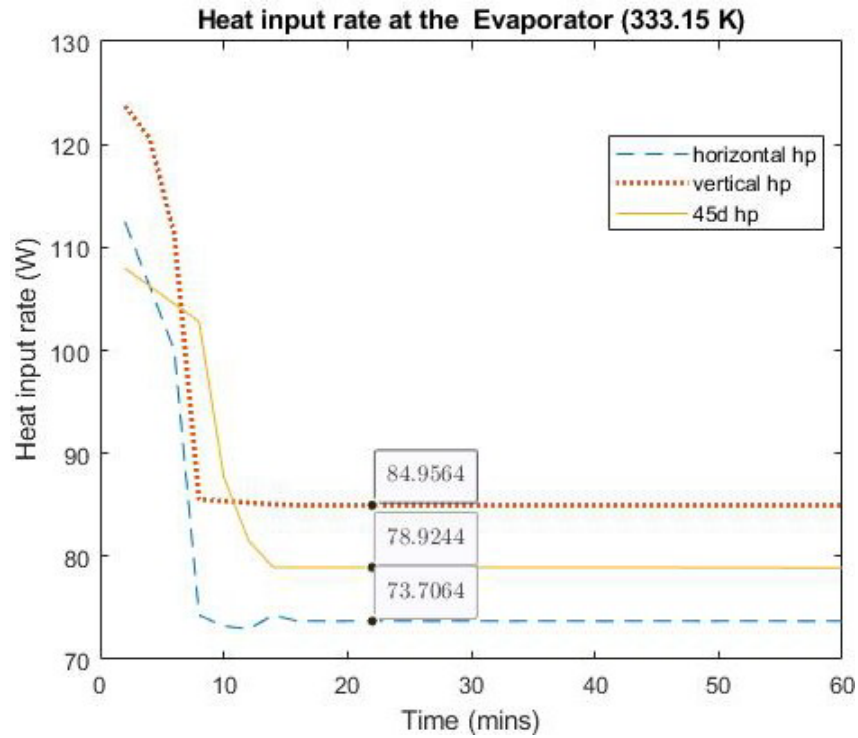


Figure 7.7: Heat input rate in the evaporator for the temperature of the evaporator at 333.15 K

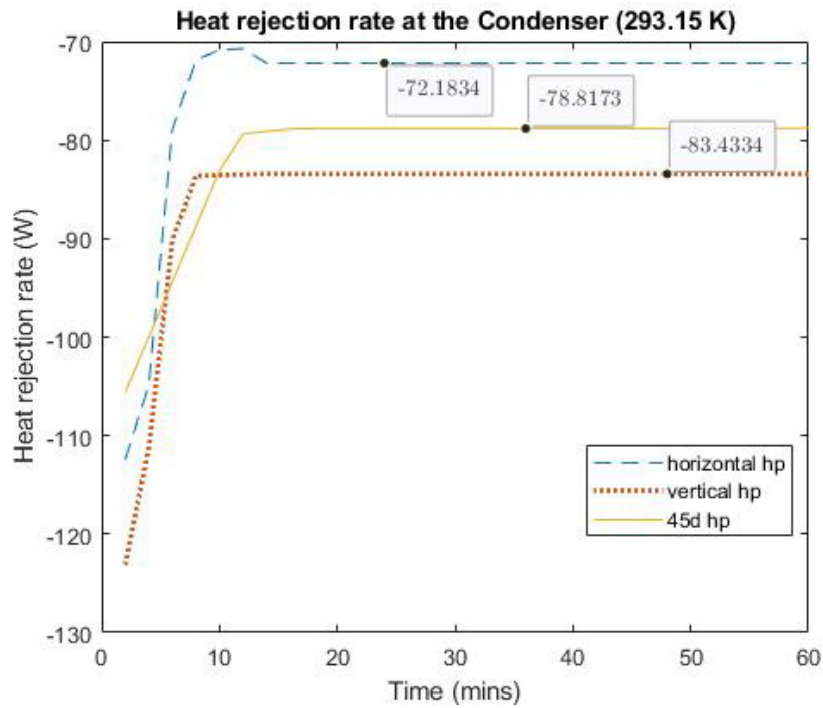


Figure 7.8: Heat rejection rate in the condenser for the temperature of the evaporator at 333.15 K

Table 7.1 shows the comparison between the obtained CFD results and the experimental temperature distribution on the horizontal heat pipe's outer wall for the heat pipe with the heating rate of 172.87 W [194]. Such comparison was conducted for qualitative estimation of the accuracy of the developed model since the heat pipe modelled and experimentally tested have a similar configuration but different dimensions.

In the CFD study, the temperature boundary condition is used for the heat input. Thus, a temperature boundary condition of 393.15 K on the evaporator section was specified, which corresponds to the heating rate of 150.50 – 138.28 W for the heat pipe with different tilt angles. As it can be seen in Table 7.1, the CFD model adequately describes the process taking place inside of the horizontal heat pipe.

Tables 7.2-7.4 show the heat transfer rates in quasi-steady state for different orientations of the heat pipe at different time intervals simulated for heat input temperatures at the evaporator section equal to 353.15 K, 373.15 K, and 393.15 K while having a constant temperature of 293.15 K at the condenser for all cases.

Table 7.1: Comparison between horizontal heat pipe experimental data input rate of 172.87 W [188] and CFD simulated heat pipe with 145 W heat input rate

Section	Position	$T_{\text{cfd}} \text{ (K)}$			$T_{\text{exp}} \text{ (K)}$ HHP	$T_{\text{cfd_av}} \text{ (K)}$			$T_{\text{exp_av}}$ (K), HHP
		VHP	HHP	45DHP		VHP	HHP	45DHP	
Evaporator	T_{e1}	373.15	372.9	373	345.75	367.05	356.69	364.29	341.6
	T_{e2}	360.95	340.48	355.58	337.45				
Condenser	T_{c1}	316.52	304.12	308.21	317.05	304.835	298.56	300.63	316.5
	T_{c2}	293.15	293	293.05	315.95				

Table 7.2: Heat transfer rates in the heat pipe as the function of time and tilt angle for the temperature of the condenser at 353.15 K

The temperature of the evaporator, equal to 353.15 K						
Time	Heat input rate at the evaporator (W)			Heat rejection rate at the condenser (W)		
	VHP	HHP	45DHP	VHP	HHP	45DHP
0	0	0	0	0	0	0
10	92.7425	80.47	87.685	-92.6225	-80.35	-87.565
20	90.2025	77.93	85.145	-90.0825	-77.81	-85.025
30	90.18525	77.91275	85.12775	-90.0653	-77.79275	-85.00775
40	90.18525	77.91275	85.12775	-90.0653	-77.79275	-85.00775
50	90.18525	77.91275	85.12775	-90.0653	-77.79275	-85.00775
60	90.18525	77.91275	85.12775	-90.0653	-77.79275	-85.00775

From the results, it can be observed that the vertical heat pipe provides the highest heat transfer rate while varying the temperature input, followed by the heat pipe with the 45-degree tilt angle. The horizontal heat pipe demonstrates the lowest heat transfer rate and could not be tested up to the power limit because the dry-out⁵ phenomenon occurs.

Table 7.3: Heat transfer rates in the heat pipe as the function of time and tilt angle for the temperature of the condenser at 373.15 K

The temperature of the evaporator, equal to 373.15 K						
Time, min	Heat input rate at the evaporator (W)			Heat rejection rate at the condenser (W)		
	VHP	HHP	45DHP	VHP	HHP	45DHP
0	0	0	0	0	0	0
10	122.8225	110.55	117.765	-122.699	-110.426	-117.641
20	120.2825	108.01	115.225	-120.159	-107.886	-115.101
30	120.2653	107.99275	115.20775	-120.141	-107.869	-115.084
40	120.2653	107.99275	115.20775	-120.141	-107.869	-115.084
50	120.2653	107.99275	115.20775	-120.141	-107.869	-115.084
60	120.2653	107.99275	115.20775	-120.141	-107.869	-115.084

⁵ Dry-out means the wick structure cannot return sufficient working fluid from the condenser region to the evaporator region.

Table 7.4: Heat transfer rates in the heat pipe as the function of time and tilt angle for the temperature of the condenser at 393.15 K

The temperature of the evaporator, equal to 393.15 K						
Time, min	Heat input rate at the evaporator (W)			Heat rejection rate at the condenser (W)		
	VHP	HHP	45DHP	VHP	HHP	45DHP
0	0	0	0	0	0	0
10	153.0575	140.785	148	-152.945	-140.673	-147.888
20	150.5175	138.245	145.46	-150.405	-138.133	-145.348
30	150.5003	138.2278	145.4428	-150.388	-138.115	-145.33
40	150.5003	138.2278	145.4428	-150.388	-138.115	-145.33
50	150.5003	138.2278	145.4428	-150.388	-138.115	-145.33
60	150.5003	138.2278	145.4428	-150.388	-138.115	-145.33

From the results, it can be observed that the vertical heat pipe provides the highest heat transfer rate while varying the temperature input, followed by the heat pipe with the 45-degree tilt angle. The horizontal heat pipe demonstrates the lowest heat transfer rate and could not be tested up to the power limit because the dry-out⁶ phenomenon occurs.

Figure 7.9 shows the plot of the heat transfer rate in the heat pipe against the temperature specified on the outer surface of the evaporator for three positions of the heat pipe. It could be seen that as the temperature increase results in an almost linear heat transfer rate rise.

⁶ Dry-out means the wick structure cannot return sufficient working fluid from the condenser region to the evaporator region.

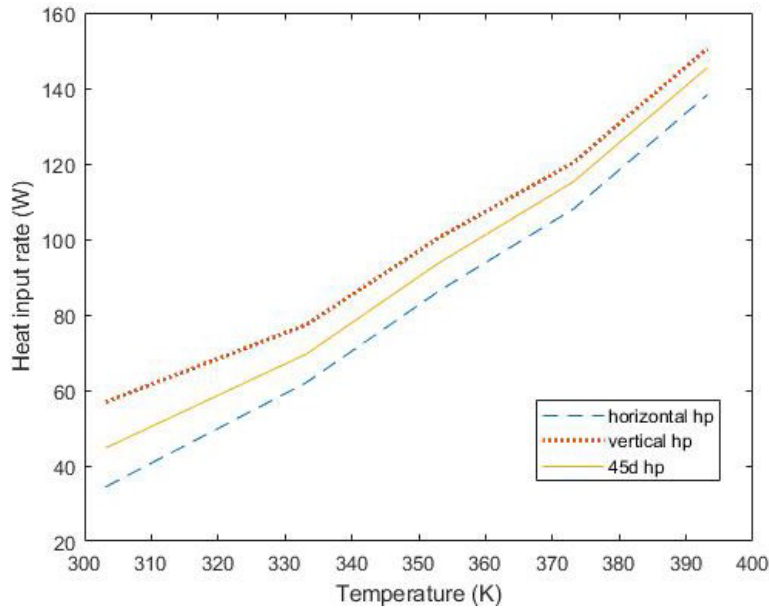


Figure 7.9: Heat transfer rate in the heat pipe as a function of the evaporator temperature for different tilt angles

7.4. Validation of CFD modelling method by thermal studies

During CFD simulations of the Thermacore heat pipe, the average temperature of the evaporator and condenser sections (T_{e1} , T_{e2} , T_{c1} , and T_{c2}) has been monitored at four different positions (as illustrated in Figure 6.5a). The monitoring points for measuring temperatures T_{e1} , T_{e2} , T_{c1} , and T_{c2} were set in the body of the evaporator and condenser walls. These temperature distributions in the walls of the heat pipe filled with the water-liquid, occupying 15% of the total volume, are shown in Figure 7.10(a-c) for various tilt angles ($\theta = 0^\circ, 45^\circ, 90^\circ$) and the specified temperatures on the outer surface of the evaporator. The temperature values influence the performance and capacity of the heat pipe, which can be enhanced through careful selection of the working fluid, design, and tilt angle. Due to the effect of gravity on the working fluid, the temperature of the T_{e2} is lower than T_{e1} for the vertical position heat pipe, and the temperature rises along the length of the evaporator in the horizontal heat pipe. For the tilted heat pipe, there is no difference between T_{e2} and T_{e1} . These results are in agreement with results published in [195].

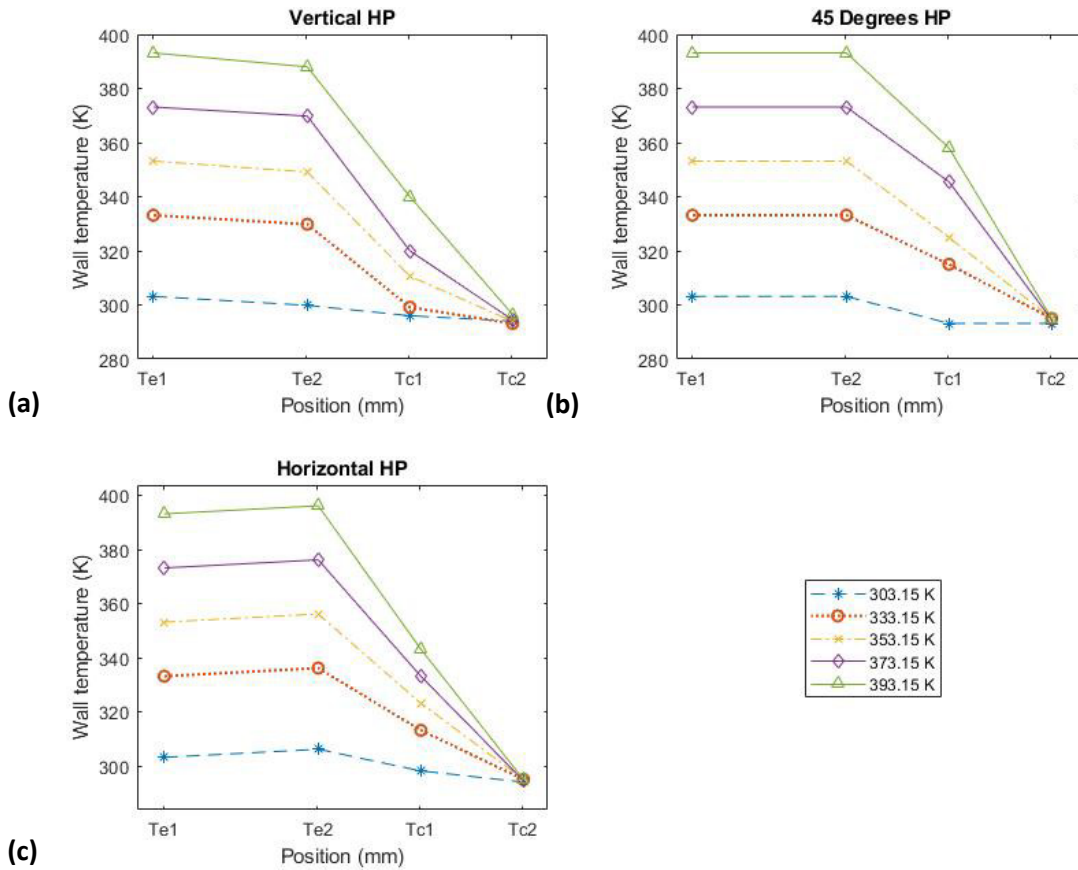


Figure 7.10: Average temperature distribution in the heat pipe as a function of constant temperature heat input boundary condition at different tilt angles (a) vertical (b) 45 degrees and (c) horizontal

Additional simulations were conducted for the same design of Thermacore heat pipe but using the constant heat input rate of 40 and 150 W as a boundary condition on the surface of the evaporator. Results are shown in Figure 7.11 (a-c) for the various tilt angles.

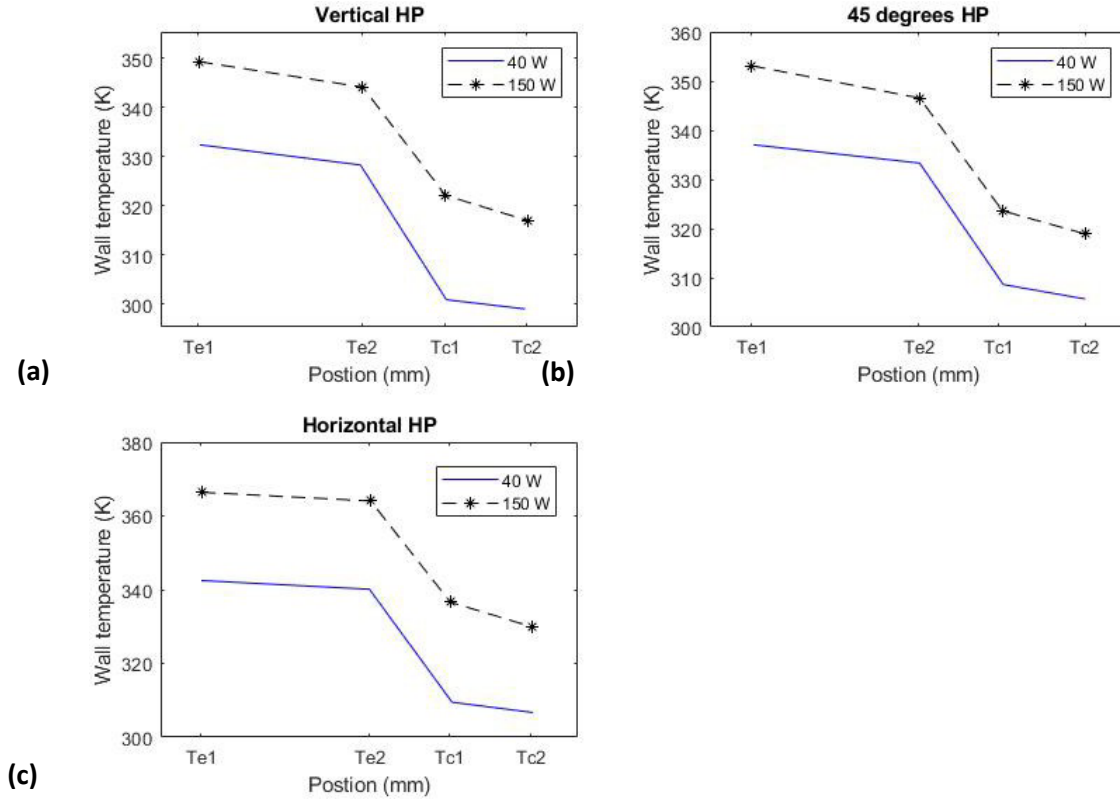
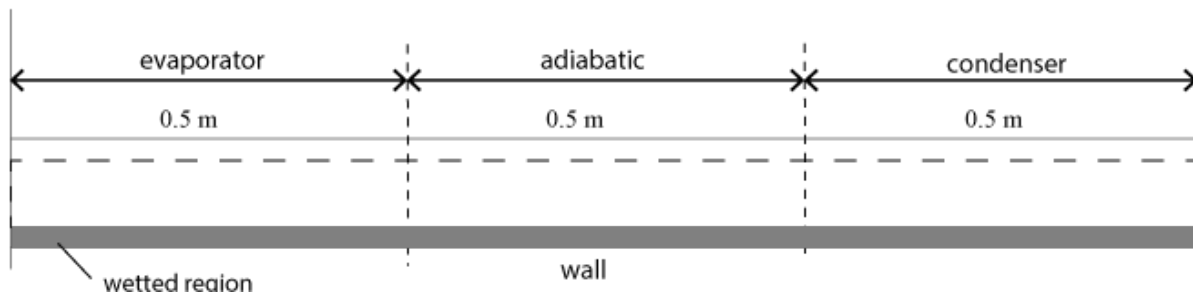


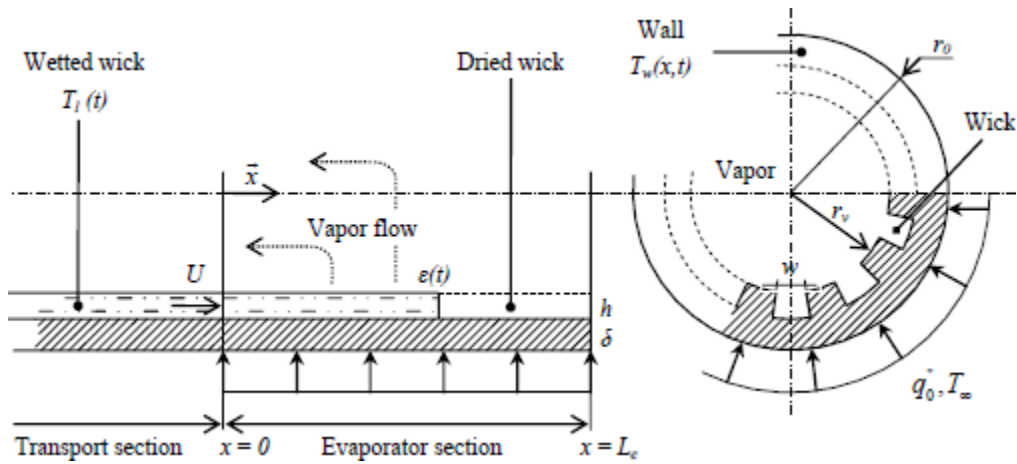
Figure 7.11: Average temperature distribution in the heat pipe as a function of constant heat input rate boundary condition at different tilt angles (a) vertical (b) 45 degrees and (c) horizontal

It can be observed in Figure 7.11 that the temperature continuously reduces along the length of the heat pipe for any orientation. These results also in full agreement with the results described in [189].

To validate the numerical solution, the CFD model was created using the geometry of the horizontal heat pipe in [196], see Figure 7.12, for which authors obtained the analytical solution for the specific case of rewetting a 0.5 m grooved evaporator with uniform heating. It is important to highlight that ethanol was used in the study by [196]. In this study, ethanol as well as water-vapour and water-liquid are used as the primary and secondary phases, respectively, in the created CFD model.



a



b

Figure 7.12: Dimensions (a) and schematic details (b) of heat pipe by Yan and Ochterbeck 1996 [196]

Table 7.5 presents the summary of heat pipe parameters. It is also worth mentioning that a constant heat flux was used instead of the temperature in this new CFD model. At the start, the liquid front is located at $x = 0$ and then begins to flow at the heated region. Without considering the evaporation effects along the wetted region in the evaporator (**Figure. 7.13a**), the numerical predictions for the locations of the liquid fronts for the ethanol working fluid fit well with the analytical solution developed in [196]. The rewetting process, which is the liquid recovery or liquid rewetting, is the advancement of the capillary column with the liquid moving in the dried region [179]. It is faster at lower heat fluxes because less fluid is evaporated from the liquid front edge. When the effects of

evaporation along the wetted region are included in the current CFD model, the difference in the liquid front predictions significantly increases.

Table 7.5: Summary of new heat pipe design parameters for the current study

Copper/ water	
Parameter Design	Current study
Outer diameter (mm)	50
Inner diameter (mm)	46.6
Wick thickness (mm)	1.7
Evaporator length (cm)	28.6
Adiabatic length (cm)	51.4
Condenser length (cm)	20
Initial temperature (K)	333 and 353
Ambient temperature (K)	313
Heat load input (W)	40, 150 & 175
Inclination Angle	0

As illustrated in **Figure 7.13b**, at the 5000 W/m² heat flux, complete rewetting of the internal evaporator surface occurs more slowly than the model predicted in [196]. This is owing to the fact the applied heat load along wet region in the evaporator's wall evaporates some of the liquid flowing as the film, thereby decreasing the liquid rewetting velocity. The current model indicates that at higher heat fluxes (15000 W/m²), the flowing film would not completely rewet the heating zone.

The liquid front advances after a while until it reaches about 0.10 m from the evaporator's beginning ($x = 0$) and then starts to recede. Dry-out occurs when the heat flux applied across the plate exceeds the liquid layer's maximum rewetting heat capacity. As a result, errors in the estimation of the maximum rewetting heat flux exist. For the sample test, the current model performed in this study provides value of 1400 W/m² for the maximum rewetting heat flux while a value of 1800 W/m² was predicted by Yan and Ochterbeck

[196]. Overall, the maximum heat flux remains reasonably consistent and provides a complete picture of the heat load effects along the wet region.

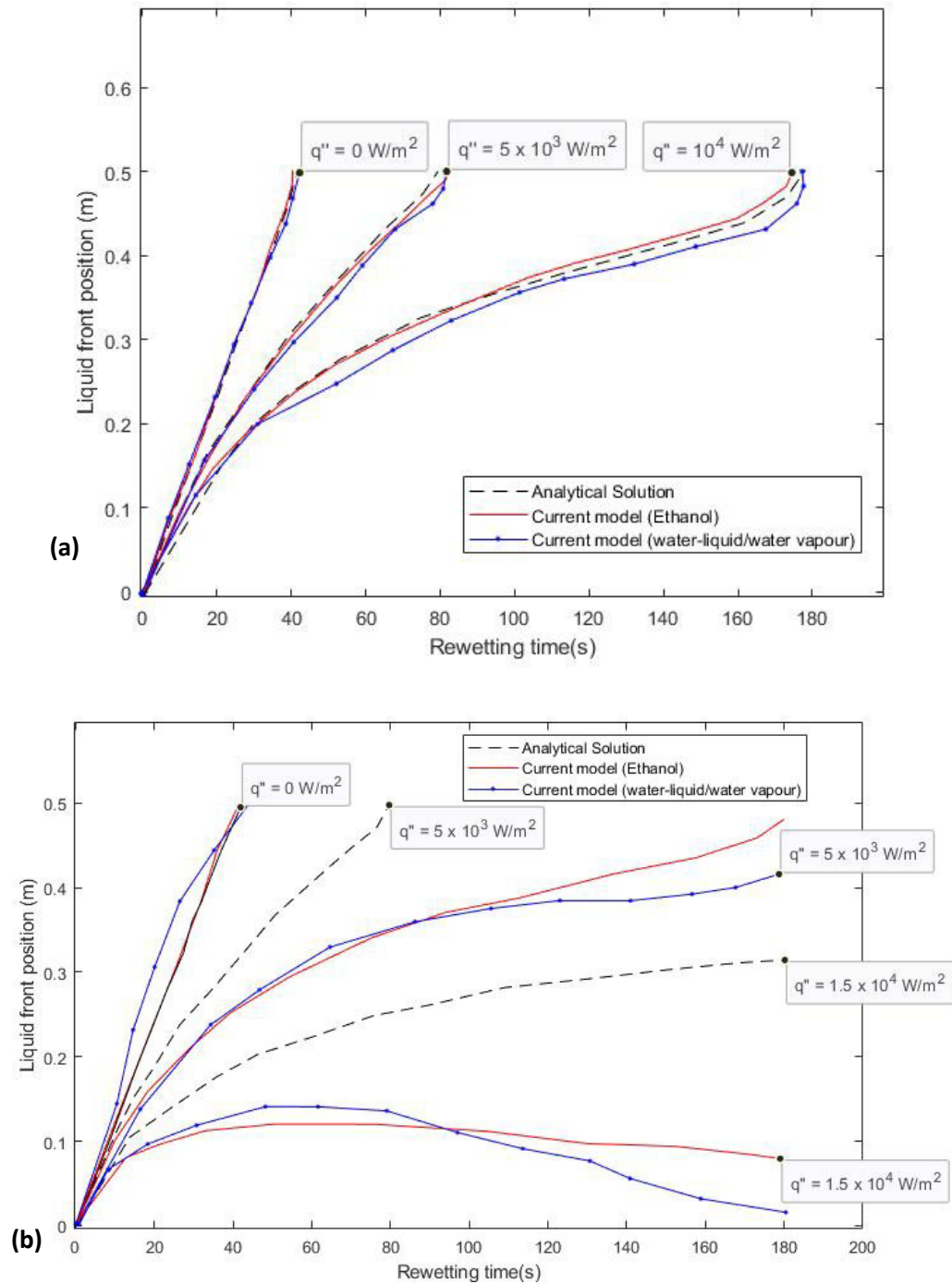


Figure 7.13: Validation and comparison of the current model with [196] without (a) and with (b) evaporation along the wetting region in the evaporator

7.5. Further validation of the CFD modelling method for a heat pipe

To further validate the CFD model, the axial distribution and the liquid front position of the wall temperature were determined using the developed CFD modelling method, using the design of the heat pipe studied experimentally in [103] with water as the working fluid, and the CFD results were compared to data from the experimental investigations. These experiments include the following: measurement of a) the capillary limiting heat flux b) measurements of the abrupt temperature rise indicative of wick dry-out; and c) the evaporator section's wall and vapour temperature profiles following a power step increase. The design configuration of the heat pipe is the same, shown in Figure 7.12, but it has different values of dimensions. The heat pipe is the copper-water one with a wick made of two layers of copper screen. The design parameters of this heat pipe are shown in **Table 7.6**.

Table 7.6: Heat pipe design parameters by [103]

Parameter Design	Ambrose et al., (1987)[103]
Outer diameter (mm)	25.5
Inner diameter (mm)	22.2
Wick thickness (mm)	1.11
Evaporator length (cm)	10.16
Adiabatic length (cm)	25.4
Condenser length (cm)	10.16
Number of layers	2
Mesh number (in ¹)	100
Wire diameter (m)	1.143×10^{-4}
Permeability (m ²)	1.93×10^{-10}
Initial temperature (K)	293
Ambient temperature (K)	293
Convective heat transfer coeff. (W.m ⁻² K ⁻¹)	200 - 500
Heat load input (W)	150 - 300
Overall heat capacity (J.K ⁻¹)	455
Inclination Angle	0°

The heat pipe was mounted horizontally and considered initially to be either operating at a power level below the capillary limit or being completely saturated with static liquid and then restarted at room (low) temperature. The temperature data collected during the experiments in study [103] was analysed and compared to the predictions made by the current transient model.

7.5.1. Comparison with data for a copper wrapped screen wick

The CFD model results compared to experimental results described in [103]. Experiments were conducted to determine a copper-water heat pipe's transient response to step changes in power input at the constant cooling rate. Adequate start-up CFD data was generated to validate the model. The transient behaviour of the heat pipe temperatures and liquid front locations were determined as a function of the evaporator's power input, the condenser's cooling conditions, and the wick's initial void fractions.

7.5.1.1. Effect of the heat input rate

In the study by Ambrose et al. (1987) [103], better predictions were obtained when the mean liquid velocity was estimated using Darcy's flow model, which considered the effects of radial hydrostatic gravity pressure drop. It should be noted that the axial groove provides a less tortuous liquid flow than the screened wick structure provides due to its geometry. As a result, the groove's liquid pressure drop is smaller than that of any other porous media. Darcy's flow model was used to correct the liquid mean velocity for the screened wick using a measured permeability, $K = 1.93 \times 10^{-10} \text{ m}^2$, and given by

$$U_0 = \frac{K}{\mu_l} \left(\frac{2\sigma}{r_{eff}} - 2\rho_l g r_v \right) \frac{1}{L_a + L_c} \quad (7.17)$$

The temperature predictions for the wall are compared to the experimental results of [103] in Figure 7.14. In this case, the model-predicted operating temperature values, with a close match the experimental values of 175 W. For high heat fluxes, the numerical peak

temperature of the heat pipe is reached more rapidly. This is due to a combination of two factors: a steeper temperature gradient due to axial conduction and an increase in the wick's dried region. Figure 7.15 shows that the position of the liquid front is dependent on the applied heat load. The current quantitative findings match the investigations in [103] into the evaporator's partial dry-out followed by liquid rewetting. For the liquid front predictions, the agreement between the current study model and Ambrose calculations is reasonably comparable. The extent of the dried region, as predicted by the model increases as the heat input increases. Additionally, it is worth mentioning that the uncertainty in these curves is primary as a result of the disparity of wick structures and pore size variations.

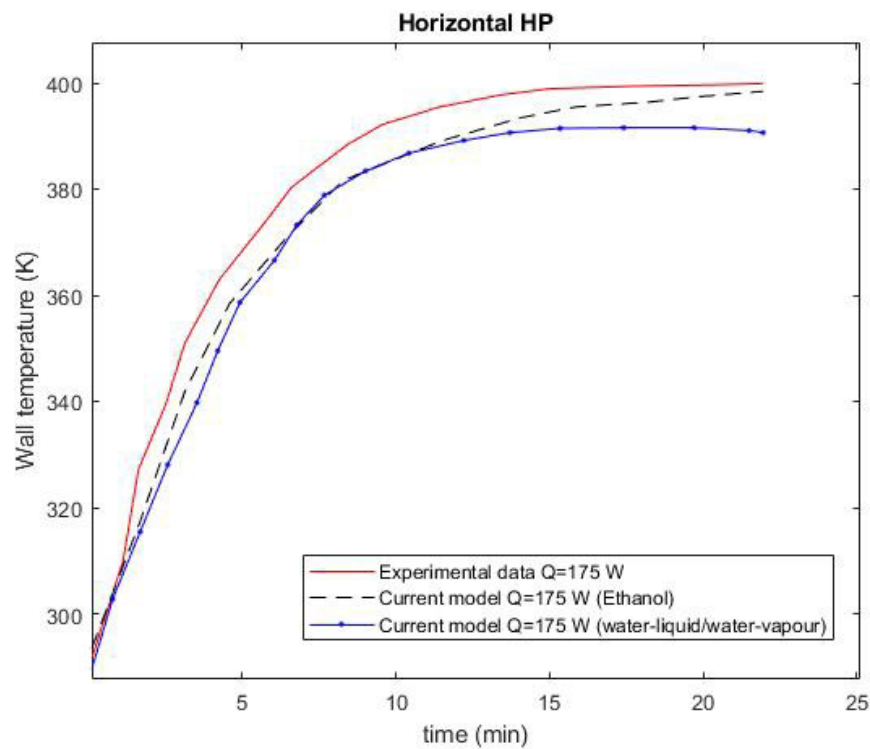


Figure 7.14: Comparison of Transient Heat Pipe Temperature Profiles with Experimental Data in [103]

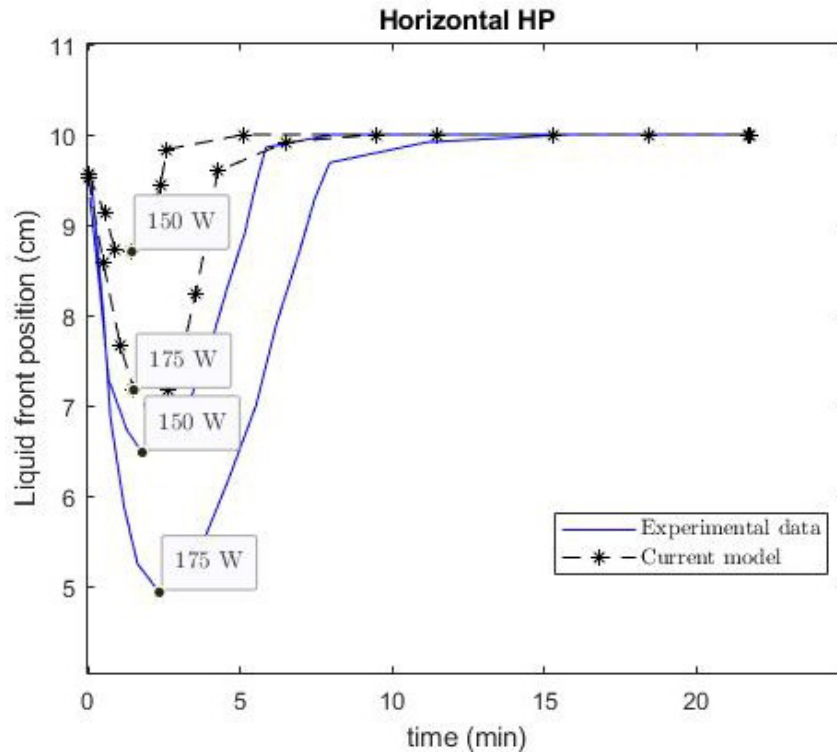


Figure 7.15: Comparison of liquid front position with experimental data in [103]

In **Figure 7.16** a full dryout is predicted for the heat input rate of 300 W. Between 225 and 300 W, a critical heat load exists such that the liquid front position remains stationary during the transient temperature increase. The amount of energy stored in the heat pipe is a critical factor in determining the rate of dryout of the liquid column. With increasing heat input, the time required to dry out decreases and the time required to rewet (if any) increases due to the longer dried region. When the liquid rewets the dried evaporator's hot surface, the energy stored in the heat pipe is increased due to the higher heat pipe temperatures, and the rewetting process takes longer. The heat transport capability gradually increases as the stored energy is removed. The evaporator recovery process following a partial dryout may become insufficient if the heat transport capacity is insufficient to remove the stored energy.

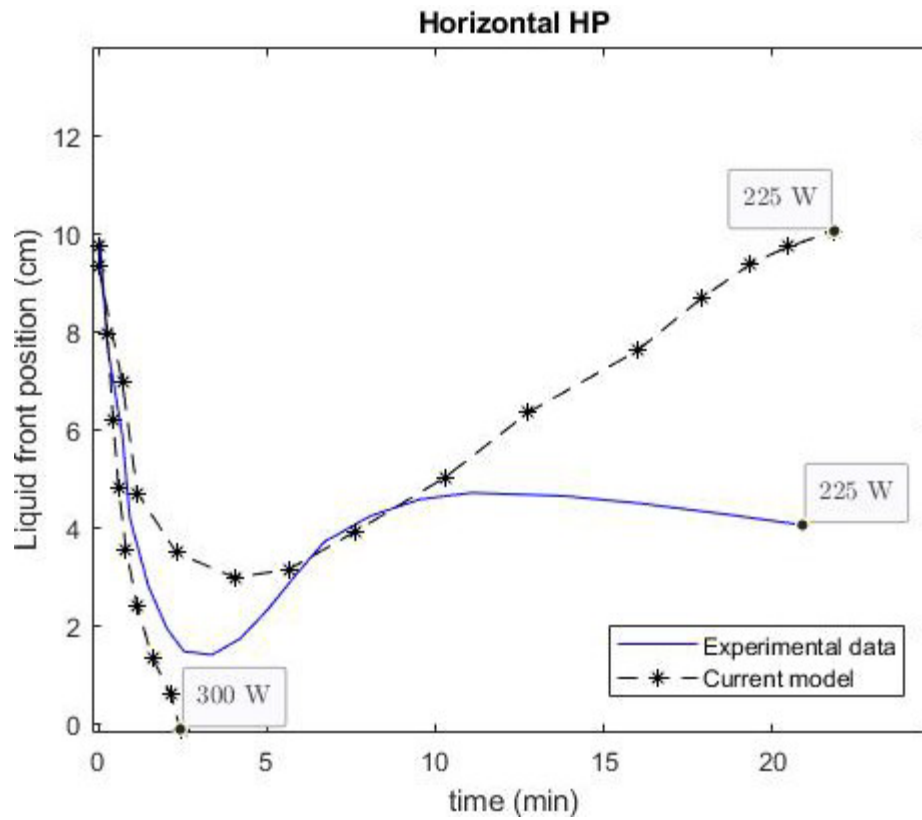


Figure 7.16: Liquid front position for 225 W (experimental and current) and 300 W (current study) predicting dryout

7.6. Chapter summary

This Chapter investigated the thermal performance of heat pipes at various tilt angles, while varying the input temperatures or heat input rates. Overall, the best thermal performance was achieved with a tilt angle of $\theta = 90^\circ$, highlighting the importance of gravitational forces. Depending on the geometry of the heat pipe, the working fluid, the heat rate input, and the condenser cooling rate, liquid behaviour and the different transient temperature is consistent with the calculated capillary limit as observed. Dryout in heat pipes can occur when there is a sharp temperature gradient in the dried region caused by higher heat input rates at constant condenser cooling conditions. This produces the superheat steam, and the stored energy at the evaporator region accumulates the heat to such an extent that the size of the dried region increases. The differences between the theoretical model's results and the experimental results are due to two main factors: a) simplifying the model's boundary conditions and b) performing an uncertainty analysis on the experimental data.

Chapter 8 Conclusions and recommendations

8.1. Conclusions

This Chapter summarises the findings of the current study. The broad objective of this work was to advance knowledge for an innovative LFR-ORC power system for which environmental and techno-economic assessments were performed to examine how competitive the integration of LRC and ORC's is to emerging renewable energy technologies such as photovoltaic and wind turbines. Furthermore, the heat transfer medium (heat pipe) for a thermal storage system was studied to develop the detailed CFD modelling method to better visualise and predict the performance of the different oriented heat pipes. The conclusions are presented in a logical order to enable a comparison to the research objectives (in Chapter 1, Section 1.2).

1. This study identified the environmental aspects which could help in determining the relative significance in terms of risk to the environment of the different RETs. In the process of manufacturing a renewable energy product, the organisation should consider the harmful emissions, land contamination, waste arisings, effluent discharges, and the use of resources (i.e., fuel, water, materials etc.) as this aspect relates to those an organisation can control. Other aspects organisations can control or may have an influence over are:
 - The land use – which may enhance the wildlife habitats and biodiversity on-site, and
 - The product design – which could improve the environmental performance and may extend the life of products.

For example, in the process of generating electricity using a wind turbine, an impact could be the reduction of climate change impacts and sustainable energy production, while another aspect could be zero-emissions during generation. In a situation where wind turbines are deployed on hills, that could be a visual impact on stakeholders in the region.

2. This study compared mainstream renewable energy technologies (RETs) with emerging solar-thermal technologies using an integrated environmental and techno-economic feasibility assessment (ETEA) framework while adopting the

eco-efficiency to measure the functional and monetary value of the systems. Eco-efficiency assessment provides useful resources for guiding decision towards the consideration of the economic and environmental aspects of a system at the same time. The results showed marked alteration in the preference ranking of the scoped six RETs, which initially based solely on the techno-economic assessment of electricity output, which was skewed more to mainstream RETs (Photovoltaic - PV, and Wind Turbine – WT), outperforming the solar-thermal RETs, with lower LCOE on average. However, the inclusion of environmental assessment showed a shift in preference towards PT-ST, PT-ORC and LFR-ORC, the three solar-thermal RETs with favourable ETEI scores. This clearly demonstrates the merit of the proposed framework in conducting a holistic sustainability appraisal of RETs, explicitly taking into consideration the total energy output (electricity + thermal) attributed to the ORC system associated with the solar thermal RETs.

Based solely on environmental performance, PT-ST and PT-ORC respectively showed the least and the highest impacts of all the six RETs, largely attributed to the gross carbon burden on a life-cycle basis from the manufacturing-to-use stages. The LFR-ORC system appear as competitive solar thermal RETs for future applications, outperforming the mainstream RETs studied, which is attributed to their lower environmental impacts (approximately 100% lower LLCI on average). Further, PT-ORC and LFR-ORC appear to be favourable based on their high NPV, beating the other mainstream RETs. However, PT-ORC emerges as the least sustainable of all the options, mainly attributed to the use of steel in component manufacturing and the use of synthetic oil as heat transfer fluid.

It is noteworthy that this study only considered the conventional ORC for thermal energy recovery, which warrants further research on more efficient material resource provision and optimisation of the component manufacturing process for thermal energy recovery and storage. New research is also needed to explore innovative measures for end-of-life recovery and reuse of the component materials, which would further improve the environmental performance of the RETs.

3. The final objective of this study was to develop a detailed three-dimensional CFD modelling method that enables accurate simulations of the evaporation and condensation processes in a porous-wick heat pipe in different orientations as well as the transient operations of a variety of low-temperature heat pipes starting from room temperature. The simulation of these processes is one of the steps required to model the entire solar power plant system and requires using special UDFs integrated into the Volume of Fluid method to account for phase change and mass transfer of the material during boiling and condensation processes. The results from the CFD simulation demonstrate that ANSYS Fluent software, when combined with the VOF and UDFs, can accurately predict phenomena occurring inside the heat pipe with different orientations. The flow visualisation demonstrates that the CFD simulation accurately reproduced the multiphase flow characteristics associated with pool boiling in the evaporator section. The results also demonstrate the CFD model's ability to visualise the pool boiling behaviour of water as the working fluid.

The balance between the capillary pressure provided by the wick in a heat pipe or vapour chamber and the flow resistance to liquid resupply at the evaporator determines the maximum steady-state heat load that can be sustained. This maximum heat load is referred to as the capillary limit; operation at constant heat loads in excess of the capillary limit results in evaporator wick dry-out. For this reason, the effect of the maximum heat load input was also investigated. The results showed that the heat transfer rate of the heat pipe always increases as the heat input rate (on the evaporator end) increases. However, for the horizontal heat pipe studied in this work, dry out occurred when the heat input temperature was above 393.15 K. The liquid was not able to flow back quickly enough from the condenser to rewet the evaporator section as a result of the high heat input rate (for fixed condenser cooling conditions). These numerical results were compared to previous investigations in [103], and the CFD relevant features which are in relatively good agreement with experiments are:

- a. The distribution of the liquid within the wick structure, which influences the transport capacity and transient operation of room-temperature heat pipes.

- b. Dryout process, which was predicted when the rates of the liquid evaporation in the wet region exceeded the supply rate by the capillary-induced flow. Dryout was always preceded by a rapid temperature increase in the dry region, whereas temperatures in the wet region may have remained uniformly distributed.

Disparities between numerical and experimental results are primarily due to the wick structure being simplified and assumed to be uniformly isotropic and saturated.

8.2. Recommendations for future work

The numerical analysis presented in this study applies to standard heat pipe configurations with conventional wicks for solar thermal applications. The following recommendations could be made for future heat pipe CFD modelling:

- Any physical phenomenon that has an effect on the liquid pressure drops in conventional heat pipes must be accounted for in the transient heat pipe model and should be investigated.
- The effects of wick saturation on the working fluid during dryout and rewetting should be included in investigations
- The numerical model should be extended to include more complex heat pipe configurations such as capillary pumped loops or loop heat pipes with estimation of the transient response of the capillary driven systems. Additional research should be conducted to determine the dryout performance of these advanced heat pipe concepts.

References

1. EIA. *International Energy Outlook 2019 with projections to 2050*. 2019; Available from: <https://www.eia.gov/outlooks/ieo/>.
2. Bourrelle, J.S., *Zero energy buildings and the rebound effect: A solution to the paradox of energy efficiency?* Energy and Buildings, 2014. **84**: p. 633-640.
3. IEA. *World Energy Outlook 2020*, IEA, Paris. 2020; Available from: <https://www.iea.org/reports/world-energy-outlook-2020>.
4. IEA. *Oil Information: Overview*, IEA, Paris. 2020; Available from: <https://www.iea.org/reports/oil-information-overview>.
5. Statista. *Daily demand for crude oil worldwide from 2006 to 2021 (in million barrels)**. 2020 [cited 2021 18/02/2021]; Available from: <https://www.statista.com/statistics/271823/daily-global-crude-oil-demand-since-2006/>.
6. da Graça Carvalho, M., *EU energy and climate change strategy*. Energy, 2012. **40**(1): p. 19-22.
7. GmbH, S.S. *Technical Sheet Engine SOLO 161* 2007 [cited 2019 08/04/2019]; Available from: <http://www.buildup.eu/sites/default/files/content/SOLO%20Stirling%20161.pdf>.
8. Varun, I.K. Bhat, and R. Prakash, *LCA of renewable energy for electricity generation systems—A review*. Renewable and Sustainable Energy Reviews, 2009. **13**(5): p. 1067-1073.
9. Alexander, T. and H.G. Hector, *Techno-economic analysis of key renewable energy technologies (PV, CSP and wind)*. 2011, Publications Office of the European Union.
10. Bravo Y., C.M., Serra L.M., Monné C., Alonso S., Moreno F., Muñoz M., *Dish-Stirling technology for power generation. Environmental evaluation*. 2011.
11. BSW. *Statistische Zahlen der deutschen Solarstrombranche (Photovoltaik)*. 2012 [cited 2018 August 19]; Available from: http://www.solarwirtschaft.de/fileadmin/media/pdf/bsw_solar_fakten_pv.pdf.
12. Nicholas DiOrio, A.D., Steven Janzou. *Economic Analysis Case Studies of Battery Energy Storage with SAM. Technical Report NREL/TP-6A20-64987*. 2015 [cited 2018; Available from: <https://www.nrel.gov/docs/fy16osti/64987.pdf>.
13. Salehin, S., et al., *Assessment of renewable energy systems combining techno-economic optimization with energy scenario analysis*. Energy, 2016. **112**: p. 729-741.
14. Abreu, M.F., A.C. Alves, and F. Moreira, *Lean-Green models for eco-efficient and sustainable production*. Energy, 2017. **137**: p. 846-853.
15. Lieberei, J. and S.H. Gheewala, *Resource depletion assessment of renewable electricity generation technologies—comparison of life cycle impact assessment methods with focus on mineral resources*. The International Journal of Life Cycle Assessment, 2017. **22**(2): p. 185-198.
16. Mazzaferro, C.A. *Life Cycle Assessment of Electricity Production from Concentrating Solar Thermal Power Plants*. 2017 [cited June 2019; Available from: tesi.cab.unipd.it/57365/1/Alberti_Mazzaferro_Cinzia_1131026.pdf.
17. Ma, W., X. Xue, and G. Liu, *Techno-economic evaluation for hybrid renewable energy system: Application and merits*. Energy, 2018. **159**: p. 385-409.
18. Tschiggerl, K., C. Sledz, and M. Topic, *Considering environmental impacts of energy storage technologies: A life cycle assessment of power-to-gas business models*. Energy, 2018. **160**: p. 1091-1100.
19. Zhang, C., et al., *Eco-efficiency assessment of technological innovations in high-grade concrete recycling*. Resources, Conservation and Recycling, 2019. **149**: p. 649-663.

20. Apichonnabutr, W. and A. Tiwary, *Trade-offs between economic and environmental performance of an autonomous hybrid energy system using micro hydro*. Applied Energy, 2018. **226**: p. 891-904.
21. IRENA, *Renewable Power Generation Costs in 2017*, International Renewable Energy Agency. 2018: Abu Dhabi. p. 1-160.
22. Edenhofer, O., *The IPCC Special Report on Renewable Energy Sources and Climate Change Mitigation*. 2011: New York.
23. Kobos, P.H., J.D. Erickson, and T.E. Drennen, *Technological learning and renewable energy costs: implications for US renewable energy policy*. Energy Policy, 2006. **34**(13): p. 1645-1658.
24. Galiana, I. and C. Green, *Let the global technology race begin*. Nature, 2009. **462**: p. 570.
25. Khan, J. and M.H. Arsalan, *Solar power technologies for sustainable electricity generation – A review*. Renewable and Sustainable Energy Reviews, 2016. **55**: p. 414-425.
26. REN21. *Renewables 2016 Global Status Report*. 2016; 5-32]. Available from: <https://www.ren21.net/gsr-2016/chapter03.php>.
27. Fthenakis, V., J.E. Mason, and K. Zweibel, *The technical, geographical, and economic feasibility for solar energy to supply the energy needs of the US*. Energy Policy, 2009. **37**(2): p. 387-399.
28. Schellekens, G., et al. *100% renewable electricity - A roadmap to 2050 for Europe and North Africa*. 2010; Available from: <http://hdl.handle.net/20.500.11850/86833>.
29. Breeze, P. *The Cost of Power Generation - The current and future competitiveness of renewable and traditional technologies*. 2010 [cited 2018 18-12-2018]; Available from: <http://lab.fs.uni-lj.si/kes/erasmus/The%20Cost%20of%20Power%20Generation.pdf>.
30. WBCSD. *Eco-efficiency: creating more value with less impact*. . 2006 [cited 2019; Available from: <https://docs.wbcsd.org/2006/08/EfficiencyLearningModule.pdf>.
31. Mankins, J.C., *Technology readiness assessments: A retrospective*. Acta Astronautica, 2009. **65**(9): p. 1216-1223.
32. Thomassen, G., et al., *A review of the sustainability of algal-based biorefineries: Towards an integrated assessment framework*. Renewable and Sustainable Energy Reviews, 2017. **68**: p. 876-887.
33. John Twidell, T.W., *Renewable Energy Resources*. 2015: Taylor and Francis.
34. IEA. *Global Energy Review 2020*, IEA, Paris. 2020; Available from: <https://www.iea.org/reports/global-energy-review-2020>.
35. IEA. *Concentrating Solar Power (CSP)*, IEA, Paris. 2020; Available from: <https://www.iea.org/reports/concentrating-solar-power-csp>.
36. Witmer, L. *Overview of Solar Thermal Power Systems || EME 811: Solar Thermal Energy for Utilities and Industry*. 2017 [cited 2021 January]; Available from: <https://www.e-education.psu.edu/eme811/node/682>
37. Robert Foster, M.G., Alma Cota, Jeanette Moore, Vaughn Nelson, *Solar Energy: renewable Energy and the Environment*, in *Introduction to Renewable Energy*. 2011.
38. Schiel, W. and T. Keck, *9 - Parabolic dish concentrating solar power (CSP) systems*, in *Concentrating Solar Power Technology*, K. Lovegrove and W. Stein, Editors. 2012, Woodhead Publishing. p. 284-322.
39. Turchi, C.S., J. Stekli, and P.C. Bueno, *11 - Concentrating solar power*, in *Fundamentals and Applications of Supercritical Carbon Dioxide (sCO₂) Based Power Cycles*, K. Brun, P. Friedman, and R. Dennis, Editors. 2017, Woodhead Publishing. p. 269-292.
40. Pitz-Paal, R., *Chapter 19 - Solar Energy – Concentrating Solar Power*, in *Future Energy (Second Edition)*, T.M. Letcher, Editor. 2014, Elsevier: Boston. p. 405-431.

41. Hoffschmidt, B.B. *Receivers for Solar Tower Systems [WWW Document]*. 2014 [cited 2021 January 5]; Available from: <http://sfera2.sollab.eu/networking/announcement-summer-schools/summer-schools/summer-school-presentation-2014>.
42. Rahbar, K., et al., *Review of organic Rankine cycle for small-scale applications*. Energy Conversion and Management, 2017. **134**: p. 135-155.
43. Galloway, E., *History and progress of the steam engine: with a practical investigation of its structure and application*. 1834: T. Kelly.
44. Shuman, F., *The Direct Acting Solar Engine: the Prime Mover of the Immediate Future*. 1907: Review Pub. & Printing Company.
45. Tabor, H. and L. Bronicki, *Small turbine for solar energy power package*. 1961.
46. Pytilinski, J., *Solar energy installations for pumping irrigation water*. Solar energy, 1978. **21**(4): p. 255-262.
47. Curran, H., *Organic working fluids in Rankine engines*. Journal of Energy, 1981. **5**(4): p. 218-223.
48. Bronicki, L. *Ormat Rankine power unit*. in *7th Intersociety energy conversion engineering conference*. 1972.
49. Wang, X. and L. Zhao, *Analysis of zeotropic mixtures used in low-temperature solar Rankine cycles for power generation*. Solar Energy, 2009. **83**(5): p. 605-613.
50. Dolz, V., et al., *HD Diesel engine equipped with a bottoming Rankine cycle as a waste heat recovery system. Part 1: Study and analysis of the waste heat energy*. Applied Thermal Engineering, 2012. **36**: p. 269-278.
51. Quoilin, S., *Sustainable energy conversion through the use of organic Rankine cycles for waste heat recovery and solar applications*. 2011, University of Liège, Liège, Belgium.
52. Wang, E., et al., *Study of working fluid selection of organic Rankine cycle (ORC) for engine waste heat recovery*. Energy, 2011. **36**(5): p. 3406-3418.
53. Wang, W., et al., *Preliminary experimental study of single screw expander prototype*. Applied Thermal Engineering, 2011. **31**(17-18): p. 3684-3688.
54. Saleh, B., et al., *Working fluids for low-temperature organic Rankine cycles*. Energy, 2007. **32**(7): p. 1210-1221.
55. Schuster, A., et al., *Energetic and economic investigation of Organic Rankine Cycle applications*. Applied thermal engineering, 2009. **29**(8-9): p. 1809-1817.
56. Stoppato, A., *Energetic and economic investigation of the operation management of an Organic Rankine Cycle cogeneration plant*. Energy, 2012. **41**(1): p. 3-9.
57. Bao, J. and L. Zhao, *A review of working fluid and expander selections for organic Rankine cycle*. Renewable and sustainable energy reviews, 2013. **24**: p. 325-342.
58. Larjola, J., *Electricity from industrial waste heat using high-speed organic Rankine cycle (ORC)*. International journal of production economics, 1995. **41**(1-3): p. 227-235.
59. Invernizzi, C., P. Iora, and P. Silva, *Bottoming micro-Rankine cycles for micro-gas turbines*. Applied thermal engineering, 2007. **27**(1): p. 100-110.
60. Chen, H., et al., *Progress in electrical energy storage system: A critical review*. Progress in Natural Science, 2009. **19**(3): p. 291-312.
61. Denholm, P., et al., *The Role of Energy Storage with Renewable Electricity Generation*. 2010.
62. Kim, Y., et al., *Potential and Evolution of Compressed Air Energy Storage: Energy and Exergy Analyses*. Entropy, 2012. **14**: p. 1501-1521.
63. Akinyele, D.O. and R.K. Rayudu, *Review of energy storage technologies for sustainable power networks*. Sustainable Energy Technologies and Assessments, 2014. **8**: p. 74-91.
64. Parkinson, G. *World's largest solar thermal plant with storage comes on-line*. 2013 [cited 2021 January]; Available from: <https://reneweconomy.com.au/worlds-largest-solar-thermal-plant-with-storage-comes-on-line-63533/>.

65. Peterson, G.P., *An Introduction to Heat Pipes, Modeling, Testing and Applications*. John Wiley and Sons, Inc., New York. , 1994.
66. Glauger, R.S., "Heat Transfer Device, U.S. Patent 2, 348, Editor. 1944.
67. Trefethen, L., "On the Surface Tension Pumping of Liquids or a Possible Role of the Candlewick in Space Exploration. GE Technical Internal Service Note, G15-D114, General Electric Co., Schenectady, NY, 1962.
68. Grover, G.M., Cotter, T.P., and Erikson, G.F., "Structures of Very High Thermal Conductivity. *Journal of Applied Physics*, 1964. **35**: p. 1190-1191.
69. Faghri, A., *Heat Pipe Science and Technology*. 1995, Bristol: y, Taylor & Francis.
70. Ivanovskii, M.N., Sorokin, V.P., and Yagodkin, I.V, *The Physical Principles of Heat Pipes*, ed. O.S.i. Physics. 1982: Oxford University Press Edn.
71. Ghodbane, M., et al., *A numerical simulation of a linear Fresnel solar reflector directed to produce steam for the power plant*. *Journal of cleaner production*, 2019. **231**: p. 494-508.
72. Ghodbane, M., et al., *Performance assessment of linear Fresnel solar reflector using MWCNTs/DW nanofluids*. *Renewable Energy*, 2020. **151**: p. 43-56.
73. Said, Z., et al., *Optical performance assessment of a small experimental prototype of linear Fresnel reflector*. *Case Studies in Thermal Engineering*, 2019. **16**: p. 100541.
74. Barbón, A., et al., *Investigating the influence of longitudinal tilt angles on the performance of small scale linear Fresnel reflectors for urban applications*. *Renewable Energy*, 2019. **143**: p. 1581-1593.
75. Bayón-Cueli, C., et al., *A cost-energy based methodology for small-scale linear Fresnel reflectors on flat roofs of urban buildings*. *Renewable Energy*, 2020. **146**: p. 944-959.
76. Bellos, E. and C. Tzivanidis, *Development of analytical expressions for the incident angle modifiers of a linear Fresnel reflector*. *Solar Energy*, 2018. **173**: p. 769-779.
77. Bellos, E., C. Tzivanidis, and A. Papadopoulos, *Secondary concentrator optimization of a linear Fresnel reflector using Bezier polynomial parametrization*. *Solar Energy*, 2018. **171**: p. 716-727.
78. Marefati, M., M. Mehrpooya, and M.B. Shafii, *A hybrid molten carbonate fuel cell and parabolic trough solar collector, combined heating and power plant with carbon dioxide capturing process*. *Energy Conversion and Management*, 2019. **183**: p. 193-209.
79. Zamzaman, A., et al., *An experimental study on the effect of Cu-synthesized/EG nanofluid on the efficiency of flat-plate solar collectors*. *Renewable Energy*, 2014. **71**: p. 658-664.
80. Bijarniya, J.P., K. Sudhakar, and P. Baredar, *Concentrated solar power technology in India: A review*. *Renewable and Sustainable Energy Reviews*, 2016. **63**: p. 593-603.
81. Javidmehr, M., F. Joda, and A. Mohammadi, *Thermodynamic and economic analyses and optimization of a multi-generation system composed by a compressed air storage, solar dish collector, micro gas turbine, organic Rankine cycle, and desalination system*. *Energy Conversion and Management*, 2018. **168**: p. 467-481.
82. Erdogan, A., C.O. Colpan, and D.M. Cakici, *Thermal design and analysis of a shell and tube heat exchanger integrating a geothermal based organic Rankine cycle and parabolic trough solar collectors*. *Renewable Energy*, 2017. **109**: p. 372-391.
83. Calise, F., et al., *Design and simulation of a prototype of a small-scale solar CHP system based on evacuated flat-plate solar collectors and Organic Rankine Cycle*. *Energy Conversion and Management*, 2015. **90**: p. 347-363.
84. Abam, F., et al., *A comparative performance analysis and thermo-sustainability indicators of modified low-heat organic Rankine cycles (ORCs): An exergy-based procedure*. *Energy Reports*, 2018. **4**: p. 110-118.
85. Bellos, E. and C. Tzivanidis, *Parametric analysis and optimization of an Organic Rankine Cycle with nanofluid based solar parabolic trough collectors*. *Renewable Energy*, 2017. **114**: p. 1376-1393.

86. Elakhdar, M., et al., *A combined thermal system of ejector refrigeration and Organic Rankine cycles for power generation using a solar parabolic trough*. Energy Conversion and Management, 2019. **199**: p. 111947.
87. E.W. Lemmon, I.H.B., M.L. Huber, M.O. McLinden, *NIST Reference Fluid Thermodynamic and Transport Properties Database - REFPROP, Version 10.0*. National Institute of Standards and Technology, Standard Reference Data Program, Gaithersburg, 2017.
88. Li, J., et al., *Performance analyses and improvement guidelines for organic Rankine cycles using R600a/R601a mixtures driven by heat sources of 100°C to 200°C*. International Journal of Energy Research, 2019. **43**(2): p. 905-920.
89. Ashouri, M., et al., *Exergy and exergo-economic analysis and optimization of a solar double pressure organic Rankine cycle*. Thermal Science and Engineering Progress, 2018. **6**: p. 72-86.
90. Ardeh, E.A.-A., et al., *Exergy and economic assessments of solar organic Rankine cycle system with linear V-Shape cavity*. Energy Conversion and Management, 2019. **199**: p. 111997.
91. Cioccolanti, L., S.R. Hamedani, and M. Villarini, *Environmental and energy assessment of a small-scale solar Organic Rankine Cycle trigeneration system based on Compound Parabolic Collectors*. Energy Conversion and Management, 2019. **198**: p. 111829.
92. Cioccolanti, L., R. Tascioni, and A. Arteconi, *Mathematical modelling of operation modes and performance evaluation of an innovative small-scale concentrated solar organic Rankine cycle plant*. Applied Energy, 2018. **221**: p. 464-476.
93. Youssef, E. and S. Dennoun, *Preliminary Assessment of an Organic Rankine Cycle Power Plant Derived by Linear Fresnel Reflector*. International Journal of Renewable Energy Research, 2018. **8**(4): p. 2014-2024.
94. Mahlia, T., et al., *Organic rankine cycle (ORC) system applications for solar energy: Recent technological advances*. Energies, 2019. **12**(15): p. 2930.
95. Cau, G. and D. Cocco, *Comparison of medium-size concentrating solar power plants based on parabolic trough and linear Fresnel collectors*. Energy procedia, 2014. **45**: p. 101-110.
96. Ruan, T., *Techno-Economic Analysis of an Innovative Purely Solar Driven Combined Cycle System based on Packed Bed TES Technology*. 2019, KTH School of Industrial Engineering and Management.
97. El hamdani, F., et al., *Techno-Economic Evaluation of a Concentrating Solar Power Plant Driven by an Organic Rankine Cycle*. Journal of Solar Energy Engineering, 2020. **142**(6).
98. Mihoub, S., *Design, economic, and environmental assessments of linear Fresnel solar power plants*. Environmental Progress & Sustainable Energy, 2020. **39**(3): p. e13350.
99. Goswami, P.K. and N.D. Choudhury, *Techno-economic evaluation of linear Fresnel reflector based concentrated solar power plant for Karbi Anglong district of Assam*. AIP Conference Proceedings, 2019. **2091**(1): p. 020018.
100. Cotter, T.P., *Heat Pipe Startup Dynamics*, in *SAE Thermionics Conversion Specialist Conference*, . 1967: Palo Alto, CA. p. 344-348.
101. Faghri, A., *Frozen Start-up Behavior of Low-Temperature Heat Pipes*. International Journal of Heat and Mass Transfer, 1992. **35**: p. 1681-1694.
102. Colwell, G.T.a.C., W.S, *Measurements of the Transient Behavior of a Capillary Structure Under Heavy Thermal Loading*. International Journal of Heat and Mass Transfer, 1984. **27**: p. 541-551.
103. Ambrose, J.H., Chow, L.C., and Beam, J.E, *Transient Heat Pipe Response and Rewetting Behavior*. Journal of Thermophysics and Heat Transfer, 1987. **1**: p. 222-227.

104. El-Genk, M.S.a.H., L., *An Experimental Investigation of Water Heat Pipe*. International Journal of Heat and Mass Transfer, 1993. **36**: p. 3823-3830.
105. Jang, J.H. *Transient Characterisitcs of a Grooved Water Heat Pipe with Variable Heat Load*. in *ASME Winter Annual Meeting*,. 1990. Dallas, TX.
106. El-Genk, M.S., Huang, L., and Tournier, J-M., "*Transient Experiments of an Inclined Copper-Water Heat Pipe*". Journal of Thermophysics and Heat Transfer, 1995. **9**: p. 109-116.
107. Legierski, J., Viciek, B., and Mey, G, *Measurements and Simulations of Transient Characteristics of Heat Pipes*,. Microelectronics Reliability, 2006. **46**: p. 109–115.
108. Koito, Y., Imura, H., Mochizuki, M., Saito, Y., Torii, S, *Numerical analysis and experimental verification on thermal fluid phenomena in a vapor chamber*. Appl. Thermal Eng, 2006. **26**: p. 1669–1676.
109. Chang, Y.W., Cheng, C.H., Wang, J, C., Chen, S.L.,, *Heat pipe for cooling of electronic equipment*. Energy Convers. Manage, 2008. **49**: p. 3398–3404.
110. Alizadehdakhel, A., Rahimi, M., Alsairafi, A. A., *CFD modeling of flow and heat transfer in a thermosyphon*. Int. J. Heat Mass Transfer, 2010. **45**: p. 312–318.
111. ISO, 14040 – *Environmental Management. Life Cycle Assessment. Principles and Framework*. International Organization for Standardization. 2006a.
112. ISO, 14044—*Environmental Management. Life Cycle Assessment. Requirements and Guidelines*. International Organization for Standardization. 2006b.
113. Ahmad, J., et al., *Techno economic analysis of a wind-photovoltaic-biomass hybrid renewable energy system for rural electrification: A case study of Kallar Kahar*. Energy, 2018. **148**: p. 208-234.
114. Chong, W.T., et al., *Techno-economic analysis of a wind–solar hybrid renewable energy system with rainwater collection feature for urban high-rise application*. Applied Energy, 2011. **88**(11): p. 4067-4077.
115. Lang, T., D. Ammann, and B. Girod, *Profitability in absence of subsidies: A techno-economic analysis of rooftop photovoltaic self-consumption in residential and commercial buildings*. Renewable Energy, 2016. **87**: p. 77-87.
116. Yang, H., Z. Wei, and L. Chengzhi, *Optimal design and techno-economic analysis of a hybrid solar–wind power generation system*. Applied Energy, 2009. **86**(2): p. 163-169.
117. Astrup, T.F., et al., *Life cycle assessment of thermal Waste-to-Energy technologies: Review and recommendations*. Waste Management, 2015. **37**: p. 104-115.
118. Curran, M., et al., *How Well Does LCA Model Land Use Impacts on Biodiversity?—A Comparison with Approaches from Ecology and Conservation*. Environmental Science & Technology, 2016. **50**(6): p. 2782-2795.
119. Jung, J., N. von der Assen, and A. Bardow, *Sensitivity coefficient-based uncertainty analysis for multi-functionality in LCA*. The International Journal of Life Cycle Assessment, 2014. **19**(3): p. 661-676.
120. von der Assen, N. and A. Bardow, *Life cycle assessment of polyols for polyurethane production using CO2 as feedstock: insights from an industrial case study*. Green Chemistry, 2014. **16**(6): p. 3272-3280.
121. von der Assen, N., et al., *Life cycle assessment of CO2 capture and utilization: a tutorial review*. Chemical Society Reviews, 2014. **43**(23): p. 7982-7994.
122. Humburg, I. *Umberto product family*. 2018; Available from: <https://www.ifu.com/en/umberto/>.
123. Ecoinvent, *Ecoinvent Centre for Life Cycle inventories database Version 3.4*. 2014.
124. Muller, K. and D.A. Sturm, *Standardized Eco-efficiency Indicators*. 2001.
125. Guinée, J., *Handbook on life cycle assessment — operational guide to the ISO standards*. The International Journal of Life Cycle Assessment, 2001. **6**(5): p. 255-255.

126. Kicherer, A., et al., *Eco-efficiency*. The International Journal of Life Cycle Assessment, 2006. **12**(7): p. 537.
127. ISO, *14045 - Environmental Management–Eco-Efficiency Assessment of Product Systems–Principles, Requirements and Guidelines*. 2012.
128. EC-JRC, *Guidance for the Implementation of the EU Product Environmental Footprint (PEF) during the Environmental Footprint (EF) Pilot Phase—Version 4.0*. 2016.
129. Katsigiannis, Y., P. Georgilakis, and E. Karapidakis, *Multi-objective genetic algorithm solution to the optimum economic and environmental performance problem of small autonomous hybrid power systems with renewable*. Renewable Power Generation, IET, 2010. **4**: p. 404-419.
130. ISO. *ISO 15686-5:2017 - BUILDINGS AND CONSTRUCTED ASSETS -- SERVICE LIFE PLANNING -- PART 5: LIFE-CYCLE COSTING*. 2017 [cited 2019 15th August]; Available from: <https://www.iso.org/standard/61148.html>.
131. PKN. *PN-EN 60300-3-3: 2017-07 - English version*. 2017 [cited 2019 15th August]; Available from: <http://sklep.pkn.pl/pn-en-60300-3-3-2017-07e.html>.
132. Miah, J.H., S.C.L. Koh, and D. Stone, *A hybridised framework combining integrated methods for environmental Life Cycle Assessment and Life Cycle Costing*. Journal of Cleaner Production, 2017. **168**: p. 846-866.
133. Moschetti, R., L. Mazzarella, and N. Nord, *An overall methodology to define reference values for building sustainability parameters*. Energy and Buildings, 2015. **88**: p. 413-427.
134. Menikpura, S.N.M., J. Sang-Arun, and M. Bengtsson, *Assessment of environmental and economic performance of Waste-to-Energy facilities in Thai cities*. Renewable Energy, 2016. **86**: p. 576-584.
135. Minne, E. and J.C. Crittenden, *Impact of maintenance on life cycle impact and cost assessment for residential flooring options*. The International Journal of Life Cycle Assessment, 2015. **20**(1): p. 36-45.
136. Akhlaghi, F., *Life cycle costing — a tool for decision making*. Facilities, 1987. **5**(8): p. 4-10.
137. Almutairi, K., et al., *Life cycle assessment and economic analysis of residential air conditioning in Saudi Arabia*. Energy and Buildings, 2015. **102**: p. 370-379.
138. Luo, L., E. van der Voet, and G. Huppes, *Life cycle assessment and life cycle costing of bioethanol from sugarcane in Brazil*. Renewable and Sustainable Energy Reviews, 2009. **13**(6): p. 1613-1619.
139. Zhao, W., G. Huppes, and E. van der Voet, *Eco-efficiency for greenhouse gas emissions mitigation of municipal solid waste management: A case study of Tianjin, China*. Waste Management, 2011. **31**(6): p. 1407-1415.
140. Adaramola, M.S., S.S. Paul, and S.O. Oyedepo, *Assessment of electricity generation and energy cost of wind energy conversion systems in north-central Nigeria*. Energy Conversion and Management, 2011. **52**(12): p. 3363-3368.
141. Clauser, C. and M. Ewert, *The renewables cost challenge: Levelized cost of geothermal electric energy compared to other sources of primary energy – Review and case study*. Renewable and Sustainable Energy Reviews, 2018. **82**: p. 3683-3693.
142. Foster, J., L. Wagner, and A. Bratanova, *LCOE models: A comparison of the theoretical frameworks and key assumptions*. 2014.
143. Campbell, M., et al. *Minimizing utility-scale PV power plant LCOE through the use of high capacity factor configurations*. in *2009 34th IEEE Photovoltaic Specialists Conference (PVSC)*. 2009.
144. Bernal-Agustín, J.L. and R. Dufo-López, *Economical and environmental analysis of grid connected photovoltaic systems in Spain*. Renewable Energy, 2006. **31**(8): p. 1107-1128.

145. Gu, Y., et al., *Techno-economic analysis of a solar photovoltaic/thermal (PV/T) concentrator for building application in Sweden using Monte Carlo method*. Energy Conversion and Management, 2018. **165**: p. 8-24.
146. Zhang, X., et al., *The early design stage for building renovation with a novel loop-heat-pipe based solar thermal facade (LHP-STF) heat pump water heating system: Techno-economic analysis in three European climates*. Energy Conversion and Management, 2015. **106**: p. 964-986.
147. Lang, T., E. Gloerfeld, and B. Girod, *Don't just follow the sun – A global assessment of economic performance for residential building photovoltaics*. Renewable and Sustainable Energy Reviews, 2015. **42**: p. 932-951.
148. Sayigh, A.A.M., *Comprehensive renewable energy*. 2012, Elsevier: Amsterdam :.
149. Rehman, S., M.A. Bader, and S.A. Al-Moallem, *Cost of solar energy generated using PV panels*. Renewable and Sustainable Energy Reviews, 2007. **11**(8): p. 1843-1857.
150. El-Shimy, M., et al., *Economics of Variable Renewable Sources for Electric Power Production*. 2017.
151. Hamburg, i., *Umberto NXT Universal*. 2017.
152. NREL, *System Advisor Model Version 2017.9.5 (SAM 2017.9.5)*. Golden, CO. 2017.
153. ANSYS. *What is ANSYS: Solving the Unsolvable*. 2020; Available from: <https://www.ansys.com/>.
154. MATLAB. *MATLAB Product Description*. 2018; Available from: https://uk.mathworks.com/help/matlab/learn_matlab/product-description.html.
155. NREL. *Annual Technology Baseline (ATB)*. 2017 April 5]; Available from: <https://atb.nrel.gov/>.
156. OpenEI. *Transparent Cost Database*. [cited 2018 July 27].
157. Turchi, C., *Parabolic Trough Reference Plant for Cost Modeling with the Solar Advisor Model (SAM)*. 2010, ; National Renewable Energy Lab. (NREL), Golden, CO (United States). p. Medium: ED; Size: 112 pp.
158. Kurup, P. and C.S. Turchi, *Parabolic Trough Collector Cost Update for the System Advisor Model (SAM)*. 2015.
159. Gilman, P. and T. Ferguson, *Reference Manual for the System Advisor Model's Wind Power Performance Model*. 2014.
160. NREL. *System Advisor Model (SAM) - Financial Models*. 2018 [cited 2018 12-09-2018]; Available from: <https://sam.nrel.gov/financial-models.html>.
161. Klason, T., *Modelling of Biomass Combustion in Furnaces*, in *Department of Energy Science* 2006, Lund Institute of Technology Sweden.
162. IRENA, *RENEWABLE ENERGY TECHNOLOGIES: COST ANALYSIS SERIES: Biomass for Power generation*. 2012.
163. Jacobson, M.Z., *Review of solutions to global warming, air pollution, and energy security*. Energy & Environmental Science, 2009. **2**(2): p. 148-173.
164. Kutscher, C., F. Burkholder, and J. Kathleen Stynes, *Generation of a Parabolic Trough Collector Efficiency Curve From Separate Measurements of Outdoor Optical Efficiency and Indoor Receiver Heat Loss*. Journal of Solar Energy Engineering, 2011. **134**(1): p. 011012-011012-6.
165. ADRASE. *Mainland Spain and Balearic Islands*. 2018 [cited 2018 August 9]; Available from: <http://www.adrase.com/en/>.
166. EnergyPlus. *Weather Data*. 2018 [cited 2018 April 6]; Available from: <https://energyplus.net/weather>.
167. Commission, E. *Photovoltaic Geographical Information System (PVGIS)*. 2018; Available from: <https://ec.europa.eu/jrc/en/pvgis>.
168. Wirz, M., M. Roesle, and A. Steinfeld, *Design Point for Predicting Year-Round Performance of Solar Parabolic Trough Concentrator Systems*. Vol. 136. 2013.

169. IRENA, *Renewable capacity statistics 2018*, I.R.E.A. (IRENA), Editor. 2018: Abu Dhabi.
170. Till Zimmermann, Max Rehberger, and S. Gößling-Reisemann, *Material Flows Resulting from Large Scale Deployment of Wind Energy in Germany*. 2013.
171. Patil, V.R., et al., *Techno-economic comparison of solar organic Rankine cycle (ORC) and photovoltaic (PV) systems with energy storage*. Renewable Energy, 2017. **113**: p. 1250-1260.
172. Government, S. *Calculating carbon savings from wind farms on Scottish peat lands: a new approach*. 2008; Available from: <https://www.gov.scot/publications/calculating-carbon-savings-wind-farms-scottish-peat-lands-new-approach/pages/13/#page-top>.
173. Kalita, P., et al., *Feasibility study of installation of MW level grid connected solar photovoltaic power plant for northeastern region of India*. Sadhana, 2019.
174. Carly Federman, P.R., Christina Watt, Paul Kell, Jack Speroni, Ana Haines, Zach Hershey, Cameron Barnhill, Piero Morote *Wind Turbine Team at Virginia Tech Siting & Project Development Written Report*. 2020.
175. Sayma, A., *Computational fluid dynamics*. Bookboon.
176. Hu, H.H., *Chapter 10 - Computational Fluid Dynamics*, in *Fluid Mechanics (Fifth Edition)*, P.K. Kundu, I.M. Cohen, and D.R. Dowling, Editors. 2012, Academic Press: Boston. p. 421-472.
177. Anderson, J., *Computational Fluid Dynamics*. 1995, New York, NY, United States: McGraw-Hill Education - Europe.
178. Diersch, H.-J., Fletcher, C. A. J., *Computational Techniques for Fluid Dynamics. Vol. I: Fundamental and General Techniques. Vol. II: Specific Techniques for Different Flow Categories. Berlin etc., Springer-Verlag 1988. XIV, 409 pp., 183 figs./XI, 484 pp., 183 figs., DM 198,00 as a Set. ISBN 3-540-18151-2/3-540-18759-6 (Springer Series in Computational Physics)*. ZAMM - Journal of Applied Mathematics and Mechanics / Zeitschrift für Angewandte Mathematik und Mechanik, 1990. **70**(9): p. 409-410.
179. Tu, J., G.H. Yeoh, and C. Liu, *Computational fluid dynamics : a practical approach*. 2013.
180. Ferziger, J.H., M. Perić, and R.L. Street, *Computational methods for fluid dynamics*. Vol. 3. 2002: Springer.
181. CFX-Solver, A., *Theory guide*. Release II, 2006.
182. V, V.H.a.M., *An Introduction to Computational Fluid Dynamics: The Finite Volume Method*, ed. S. Edition. 2007: Pearson Education Limited.
183. Fluent, A., *ANSYS Fluent User's Guide*. 2011.
184. Murtha, M. *Terminology Explained: What is multiphase flow*. 2017 [cited 2021; Available from: <https://blogs.dnvgl.com/software/2017/06/terminology-explained-multiphase-flow/>].
185. Fadhl, B., L.C. Wrobel, and H. Jouhara, *Numerical modelling of the temperature distribution in a two-phase closed thermosyphon*. Applied Thermal Engineering, 2013. **60**(1): p. 122-131.
186. Lee WH, *Pressure Iteration Scheme for Two-Phase Modeling*. 1979: Los Alamos Scientific Laboratory.
187. Lee, W., *A Pressure Iteration Scheme for Two-Phase Flow Modeling*. Computational Methods for Two-Phase Flow and Particle Transport, 2013: p. 61–82.
188. Li, Q.W., C.; Wang, Y.; Wang, Z.; Li, H.; Lian, C, *Study on the effect of the adiabatic section parameters on the performance of pulsating heat pipes*. Applied Thermal Engineering, 2020(180).
189. Launder BE and Spalding DB, *Lectures in mathematical models of turbulence*. 1972, London, England: Academic Press.
190. Chung TJ, *Computational Fluid Dynamics*. 2002: Cambridge University Press.

191. Ekambara K, D.M., Joshi JB, *CFD simulation of homogeneous reactions in turbulent pipe flows-Tubular non-catalytic reactors*. Chemical Engineering Journal, 2006. **117**: p. 23-29.
192. Saber MH, A.H. *Simulation and CFD Analysis of heat pipe heat exchanger using Fluent to increase of the thermal efficiency*. in *Proceedings of the 7th WSEAS International Conference on Heat and Mass Transfer*. 2010. Cambridge.
193. Ekambara K, S.R., Nandakumar K, Masliyah JH,, *CFD simulation of bubbly two-phase flow in horizontal pipes*. Chemical Engineering Journal, 2008. **144**: p. 277-288.
194. *Copyright*, in *Future Energy (Second Edition)*, T.M. Letcher, Editor. 2014, Elsevier: Boston. p. iv.
195. Alireza Esmailzadeh, M.S., Nik Nazri Nik Ghazali, Hendrik Simon Cornelis Metselaar, Azuddin Bin Mamat, Mohammad Sajad Naghavi Sanjani and Soudeh Iranmanesh *Thermal Performance and Numerical Simulation of the 1-Pyrene Carboxylic-Acid Functionalized Graphene Nanofluids in a Sintered Wick Heat Pipe*. Energies, 2020.
196. Yan, Y.H.a.O., J.M.,. *Integral Method Solutions for Rewetting of Finite Length Surfaces with Uniform Heating*. in *National Heat Transfer Conference*. 1996. Houston TX.
197. Chi, S.W., *Heat Pipe Theory and Practice*, ed. M. Graw-Hill. 1976, Washington London: Hemisphere Publishing Company.
198. Chisholm, D., *The Heat Pipe*. 1971, London, England: Mills and Boon.
199. Busse, C.A., *Theory of the Ultimate Heat Transfer of Cylindrical Heat Pipes*. International Journal of Heat and Mass Transfer, 1973. **16**: p. 169–186.
200. Dunn, P.D.a.R., D.A.,, *Heat Pipes*, ed. r. Edn. 1982, New York: Pergamon Press.
201. Garimella, S.V.a.S., C.B., *Recent Advances in the Modeling and Applications of Conventional and Non-conventional heat pipes*. Advances in Heat Transfer, 2001. **35**: p. 249-308.

APPENDIX A

This section provides further insight on geometry designs, wick structures, the general design characteristics and steady-state performance of a room temperature heat pipe, operating temperature range, working fluids and heat transport limitations of a typical heat pipe.

Low-Temperature Heat Pipes: General Design Characteristics

Theoretically, at any temperature a heat pipe can operate between the triple and supercritical states of the working fluid. However, depending on the application, heat pipe has different temperature operating range and the maximum heat transport capacity. As a result, caution must be exercised in selecting the working fluid based on the operating temperature and pressure condition, as well as chemical compatibility with the container and wick materials [197].

Temperature Range of Operation and Working Fluids

Cryogenic heat pipes operate between 0 and 200 K, low heat pipes operate between 200 and 550 K, medium heat pipes operate between 550 and 770 K, and high (liquid metal) heat pipes operate between 750 and 3000 K. At room temperature, the working fluids are typically polar molecules and halocarbons such as ammonia, and water etc.; at cryogenic temperatures, the working fluids are typically elemental or simple organic gases, or liquid metals. Figure A1-1 illustrates the approximate useful range of several low temperature working fluids. Heat pipe with low-temperature can transfer more heat axially than cryogenic heat pipes, but not as much as high-temperature heat pipes. The four temperature range boundaries should be regarded as approximations, as some fluids cross over into the next temperature range.

The surface tension and thermal conductivity of several low-temperature working fluids are depicted in Figure A1-2. Whatever the geometry of the heat pipe, the best performance is obtained by using fluids with a high liquid-vapor surface tension σ , a high

latent heat H_{fg} , a high liquid density ρ_l , and a low liquid dynamic viscosity μ_l . These thermophysical properties are quantified by [197, 198] in terms of the figure of merit, which is defined as

$$\eta \triangleq \frac{\rho_l \sigma H_{fg}}{\mu_l} \quad \text{Equation A1}$$

Working fluids exhibiting higher thermal potentials are preferable utilized in heat pipes. For heat pipes that operate at room temperature, the most frequently used materials for wick structures and containers are aluminum or stainless steel for ammonia heat pipes and copper for water heat pipes.

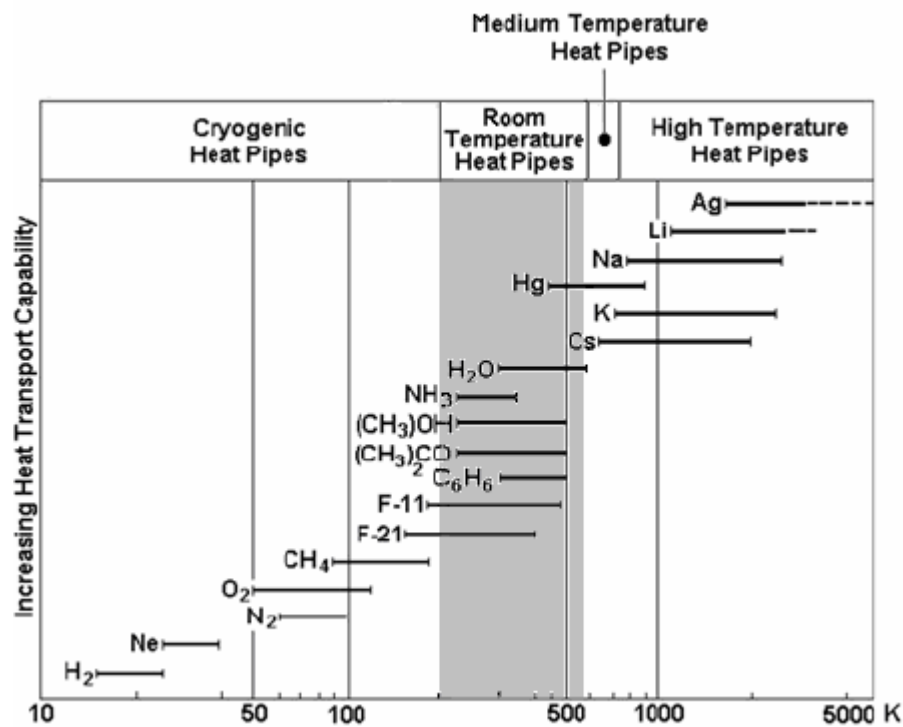


Figure A1- 1: Temperature Range of Operation and Working Fluids [65]

As illustrated in Figure A1-1 and A1-2, water possesses superior thermophysical properties such as heat of vapourisation and surface tension, while also being relatively safe and easy to handle.

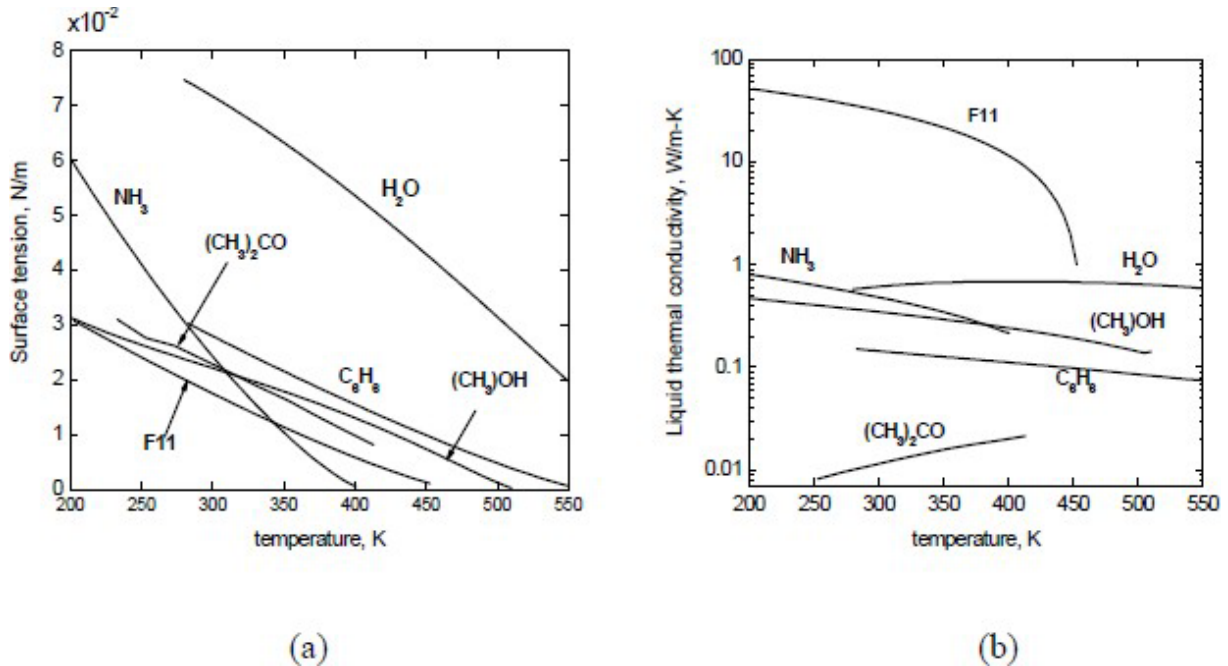


Figure A1- 2: Low-Temperature fluids for (a) surface tension and (b) liquid thermal conductivity

Anhydrous ammonia is an excellent working fluid below the freezing point of water and above 200 K. It is widely used in spacecraft and instrument control applications operating in the 200-350 K temperature range. However, precautions should be taken with ammonia exposures in the liquid and vapour states.

Heat pipe geometry designs and wick structures

As with other types of heat pipes, low-temperature heat pipes have a variety of geometric designs depending on their intended use. The conventional or cylindrical heat pipe (HP) is the most widely used, whereas other geometries such as flat plate heat pipes (FPHP) and disk-shaped heat pipes (DSHP) are more commonly used in electronic and

microelectronic cooling. Additionally, FPHP and DSHP can be approximated using models of conventional heat pipes with wall and wick thicknesses less than the heat pipe diameter.

Apart from the working fluid and external geometry, the primary distinction between heat pipes is the wick structure. The wick's primary function is to provide a path for condensate to return and to support the pressure gradients required for heat pipe operation. Improved wick structures have been developed because of efforts to push the operational limits of heat pipes. There are a variety of wick structures that are frequently used, including screen, grooves, felt, and sintered powder. Chi [197] provides an excellent overview of heat pipe wick designs. Each of these wicks shares a characteristic. The dimensions of the liquid flow passages are identical to those of the pressure support.

They are constructed using structures with a large flow passage and a small connecting slot, such as arteries and/or monogroove heat pipes (Figure A1-3). An ideal capillary wick structure maximizes the radius of the flow paths while minimizing the radius of the pore surface.

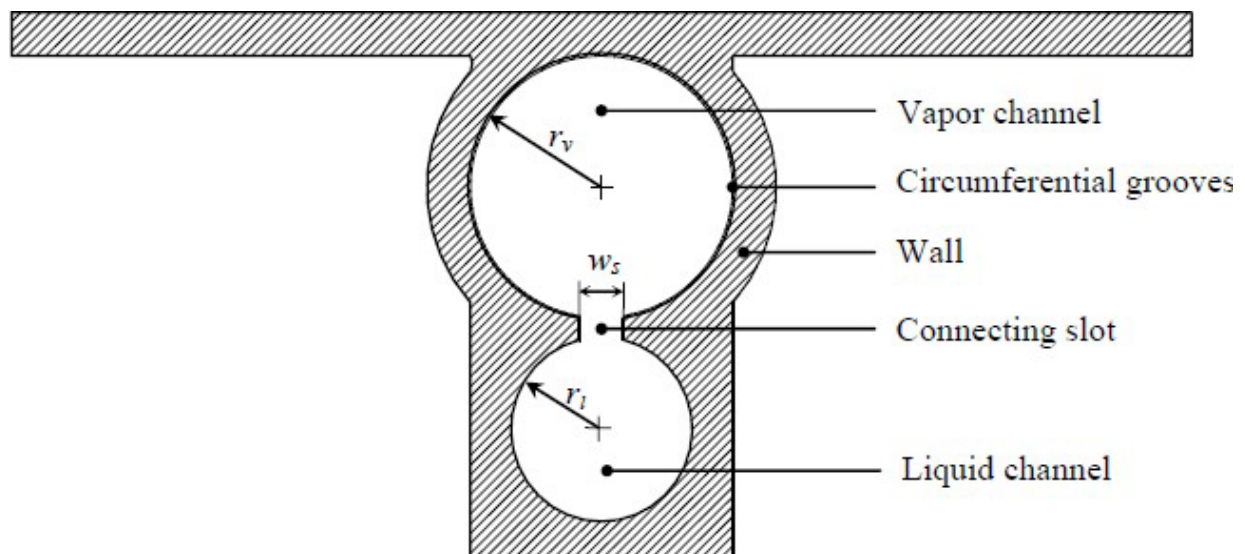


Figure A1- 3: Monogroove heat pipe cross sectional area

Typically, the heat pipe's capacity to transport energy decreases as the angle of operation against gravity increases. Due to the limited capillary force capability of grooved and screen meshed wicks, they typically cannot withstand significant gravitational forces and will dry out due to tilt angle. However, these wicks have been shown to perform well in zero-gravity applications and environments.

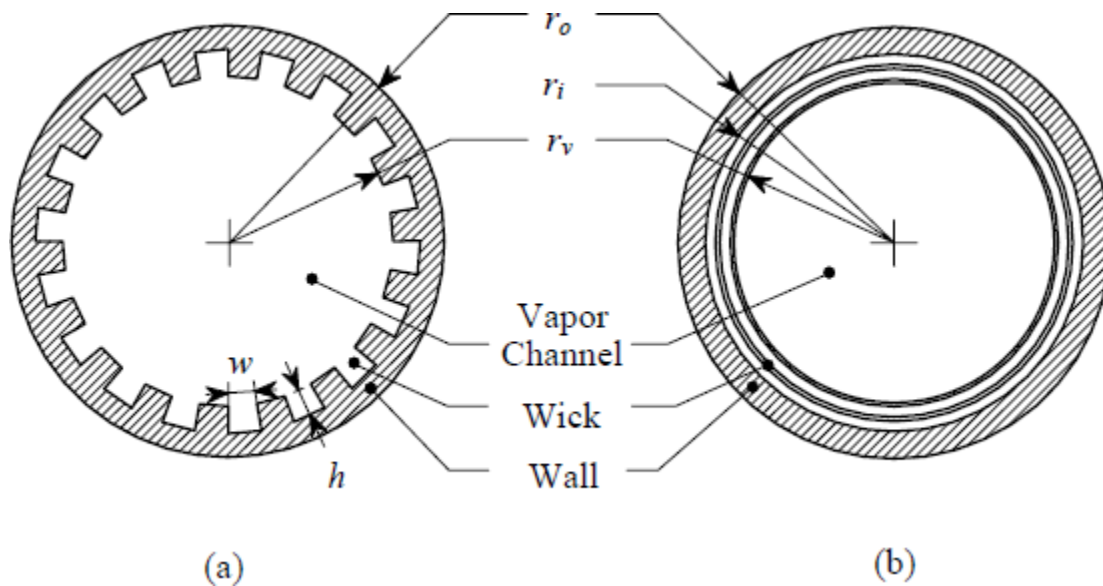


Figure A1- 4: (a) Rectangular Axial extruded grooves and (b) two layers of wrapped screens Cross-sectional Areas of a conventional Heat Pipe

These heat pipes feature a conventional geometry and wick structures comprised of either axially grooved or wrapped screens. Additionally, a configuration utilizing a single graded groove structure will be considered. A single graded groove structure has the purpose of enhancing capillary pumping without increasing flow resistance. The cross-sectional areas of Figures A1-3 and A1-4 illustrate the geometric characteristics of heat pipes.

Low-Temperature Heat Pipes Steady State Performance: Heat transport limitations

The steady state performance of a heat pipe is constrained by a variety of factors, including the working fluid's properties, the geometry of the design, and the pore size of the wick structure. The viscous, sonic, condenser, entrainment, capillary, and boiling limits all apply to heat pipe operations. As [199] demonstrated, the high vapour pressure and density of low-temperature heat pipes result in a small vapour velocity and pressure drop. As a result, the viscous, sonic, and entrainment limits are frequently exceeded, allowing the vapour to flow to the condenser section. As a result, the capillary and boiling limits are the primary constraints on heat transport in room-temperature heat pipes. Both constraints result in heat pipe failure.

Capillary limit

Capillary forces are not sufficient for transferring enough liquid from the condenser to the evaporator when there is insufficient capillary force in the wick, the evaporator section may experience dry-out, and the heat pipe will cease to function. The capillary limit can therefore be defined as the power level at which capillary action ceases to supply sufficient fluid to completely wet the evaporator. Under normal steady-state conditions, a heat pipe's wick structure must generate enough capillary-driven pressure to overcome the total pressure drop. At any time, the following condition must be satisfied regarding capillary pressure ΔP_{cap} :

$$\Delta P_{cap} \geq \Delta P_{tot}, \quad \text{Equation A2}$$

where ΔP_{tot} is the total pressure drop due to friction along the liquid path ΔP_l , the vapour path ΔP_v pressure drops in the liquid due to body forces (gravity, electromagnetic), and pressure drops due to phase change at the liquid-vapor interface. Pressure drops due to liquid-vapor phase change are generally negligible for room-temperature heat pipes due

to the low evaporation or condensation rates. Thus, the pressure drop balance may be reduced to:

$$\Delta P_{tot} = \Delta P_l + \Delta P_v + \Delta P_g. \quad \text{Equation A3}$$

The pressure balance in Equation A.3 is satisfied when a normal liquid-vapor meniscus is operating as described in Equation A.3. However, wick structure's effective pore size is constrained by its radius of curvature. Equation A4 represent the maximum capillary pumping reached by the wick developed at the wet and dry points

$$\Delta P_{cap,max} = \frac{2\sigma}{r_{eff}}, \quad \text{Equation A4}$$

The effective radius pore is represented by r_{eff} . And $\Delta P_{cap,max} = \Delta P_{tot}$. represents the occurrence of the maximum heat transport.

Boiling limit

Boiling point may also pose a problem for low-temperature heat pipes. When the applied heat flux is increased, nucleate boiling may occur within the wick structure. A build-up of vapour bubbles in an evaporator wick can be detrimental, leading to hot spots, impeding liquid circulation, and causing dry-out. A low-temperature heat pipe will often experience such phenomena at the upper end of its operating temperature range due to large radial heat fluxes. The boiling point is determined using nucleate boiling theory. In a steady state operation, it involves bubble formation, growth, and collapse. For a wick structure to avoid boiling, the maximum heat transfer rate is expressed as follows: [197]

$$Q_b = \frac{2\pi L_{eff} k_{eff} T_{v,sat}}{\rho_v H_{fg} \ln(r_i / r_v)} \left[\frac{2\sigma}{r_n} - \Delta P_{cap,max} \right], \quad \text{Equation A5}$$

where k_{eff} denotes the effective thermal conductivity of the liquid-wick combination, L_{eff} denotes the effective heat pipe length, $T_{v,sat}$ denotes the saturated vapour temperature, r_v and r_i were defined in Figures. A3 and A4, and r_n denotes the critical nucleation site radius, which [200] define as 0.1 to 25.0 μm for conventional metallic heat pipe case materials.

Heat pipes start up: Transient Operations

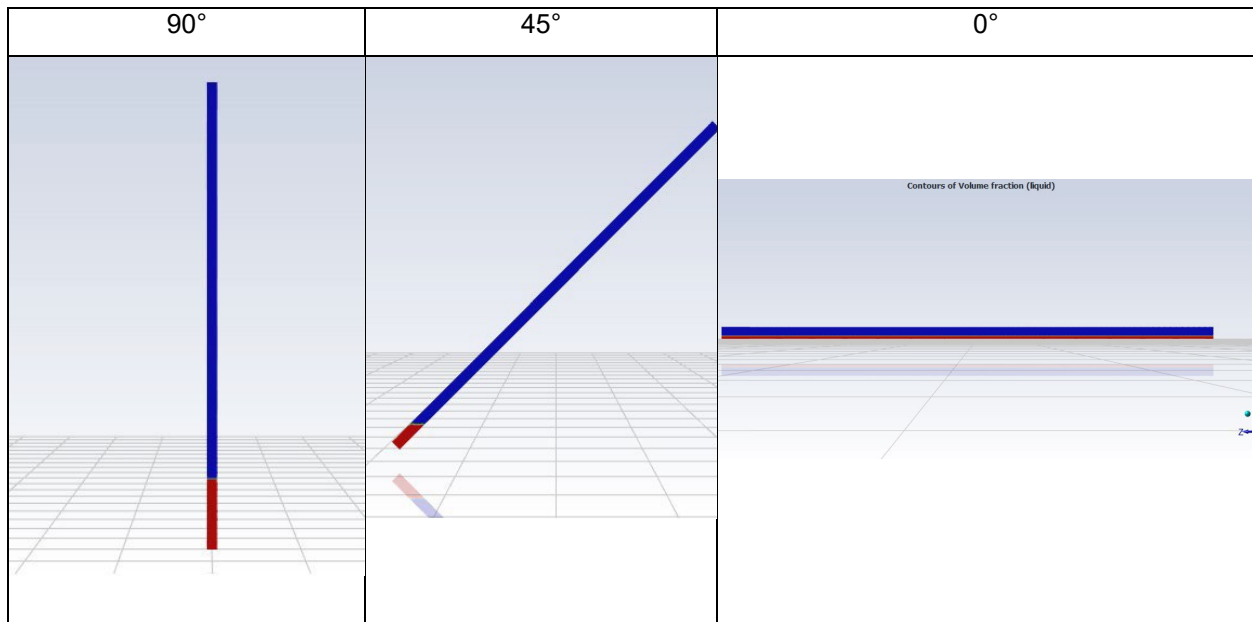
Heat pipes are typically not used in steady state conditions in a wide variety of thermal control applications. Since heat pipes were first used as energy converters capable of handling variable heat loads, transient operations have been involved [100]. Numerous heat pipes operate in transient conditions to address heat dissipation issues and temperature fluctuations associated with electronic components [201]. Thus, transient operations encompass not only startup and shutdown, but also power changes and reversed heat pipe operations caused by external condenser heating. One of the most severe cases of transient – which can result in a potential operating failure – occurs during the initial startup of a heat pipe that is thermally insulated from its environment. According to the thermal environment and the corresponding state of the working fluid, three types of startups exist: normal, supercritical, and frozen startups.

A normal startup is characterized by a rapid increase in heat loads from zero to a specified value while the working fluid remains static in the saturated liquid-vapor state. Increases in the temperature of the heat pipe or the input of heat load can result in a significant transfer of working fluid from the evaporator to the condenser. This is due to a volume change at the liquid-vapor interface. A successful startup is highly dependent on the time response and distribution of the liquid within the wick. A supercritical startup occurs when the working fluid is initially in the gaseous state, whereas a frozen startup occurs when the working fluid is initially in the frozen state [193, 201]. Thus, when operating a heat pipe under supercritical conditions, the working fluid must condense at temperatures below the critical point, while a heat pipe under frozen conditions must have melted working fluid to operate.

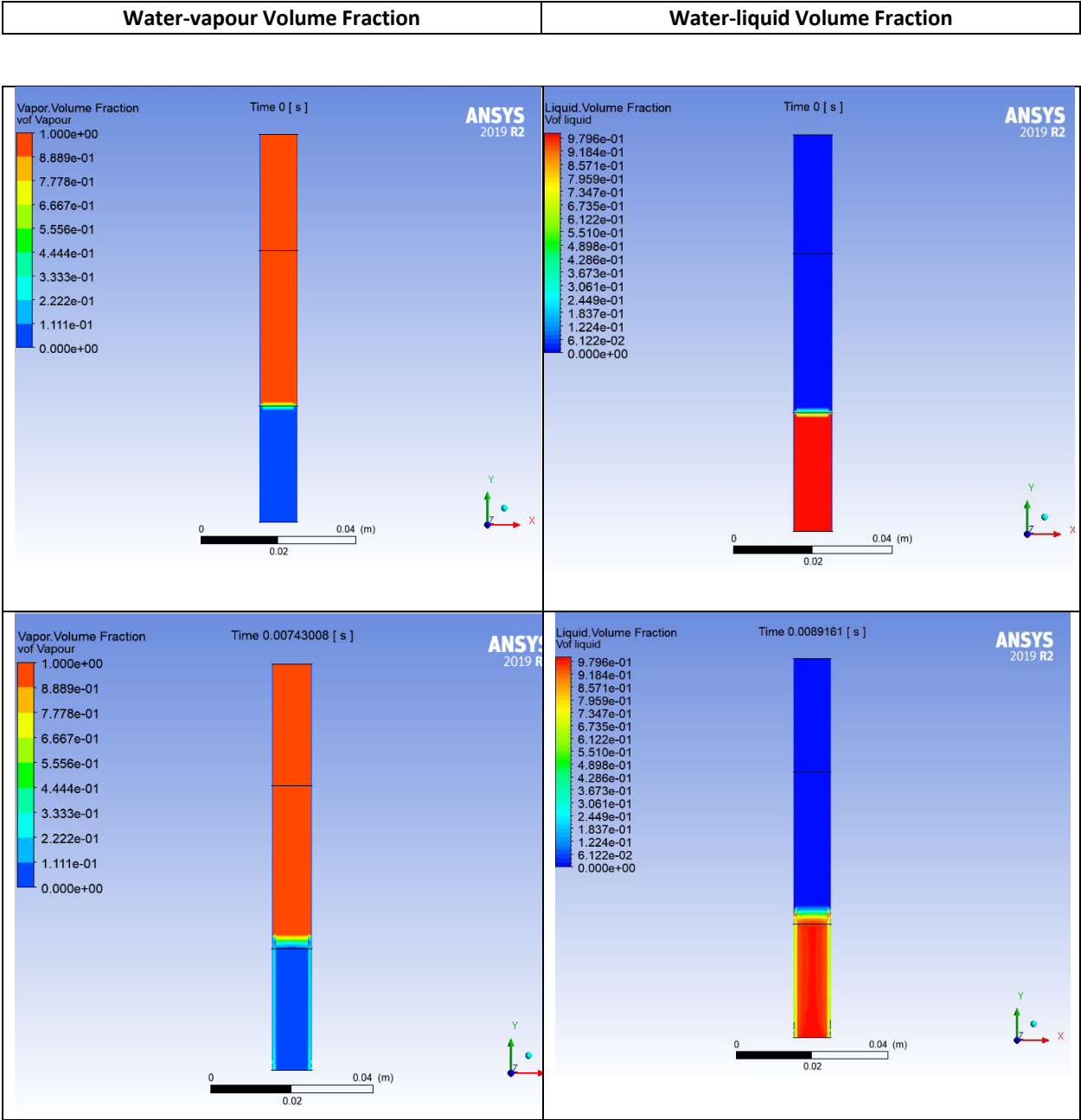
APPENDIX B

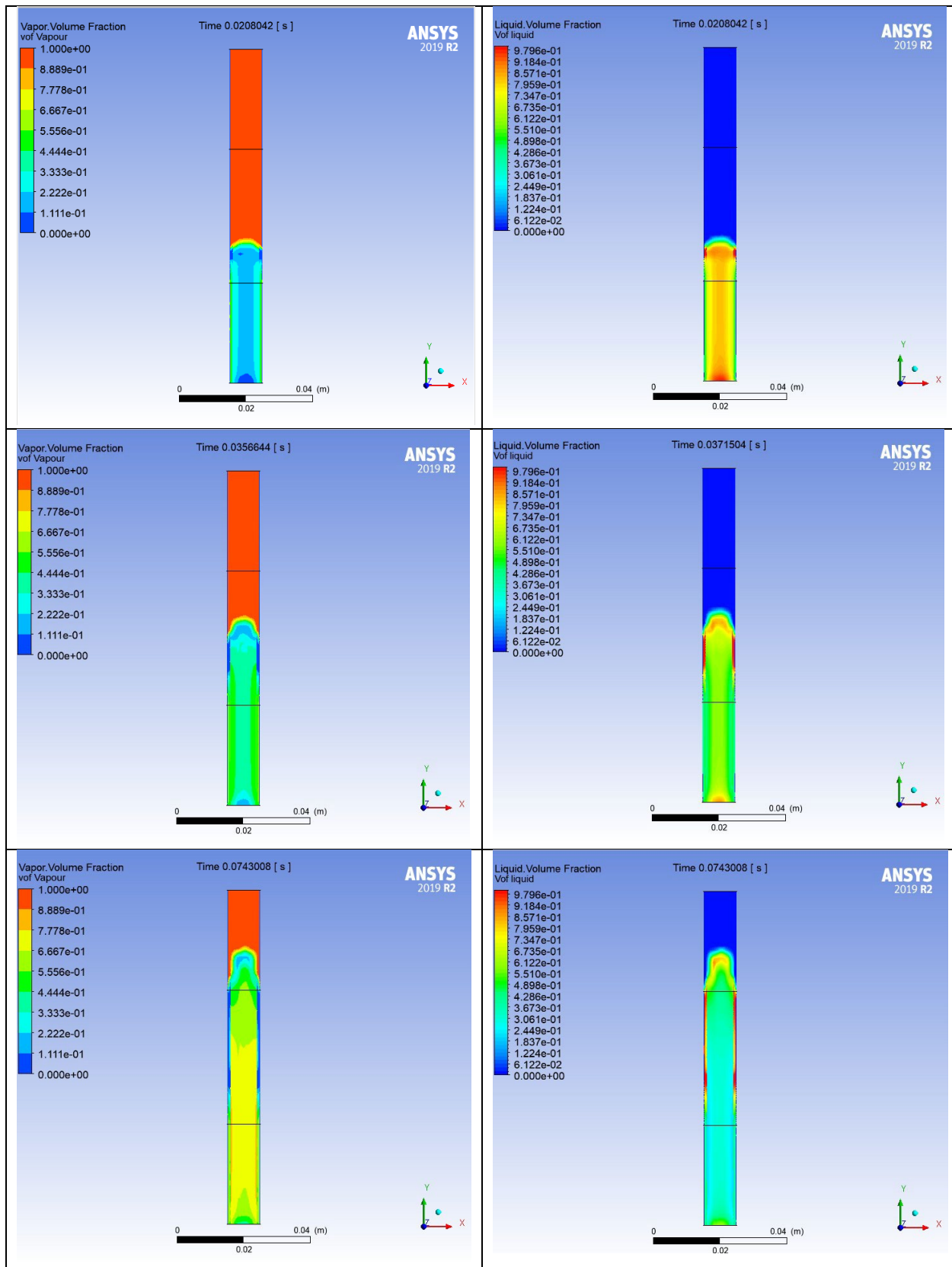
This section contains images for water-liquid for the 3-case heat pipes with a fill ratio of 15%. Also, in this section the water-liquid and water-vapour volume of fraction and temperature distribution for the vertical heat pipe are shown.

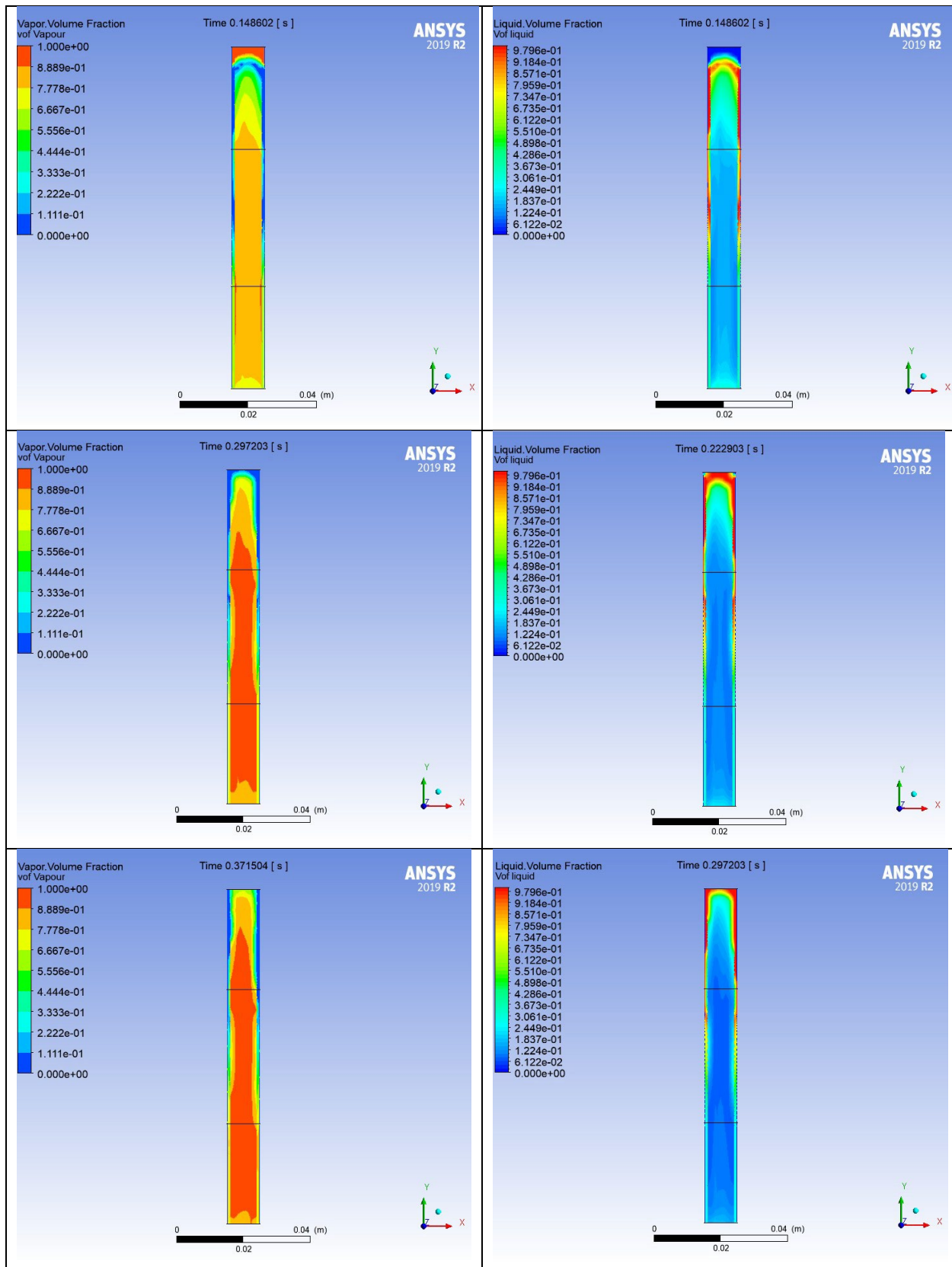
B1. 15% water-liquid filled ratio

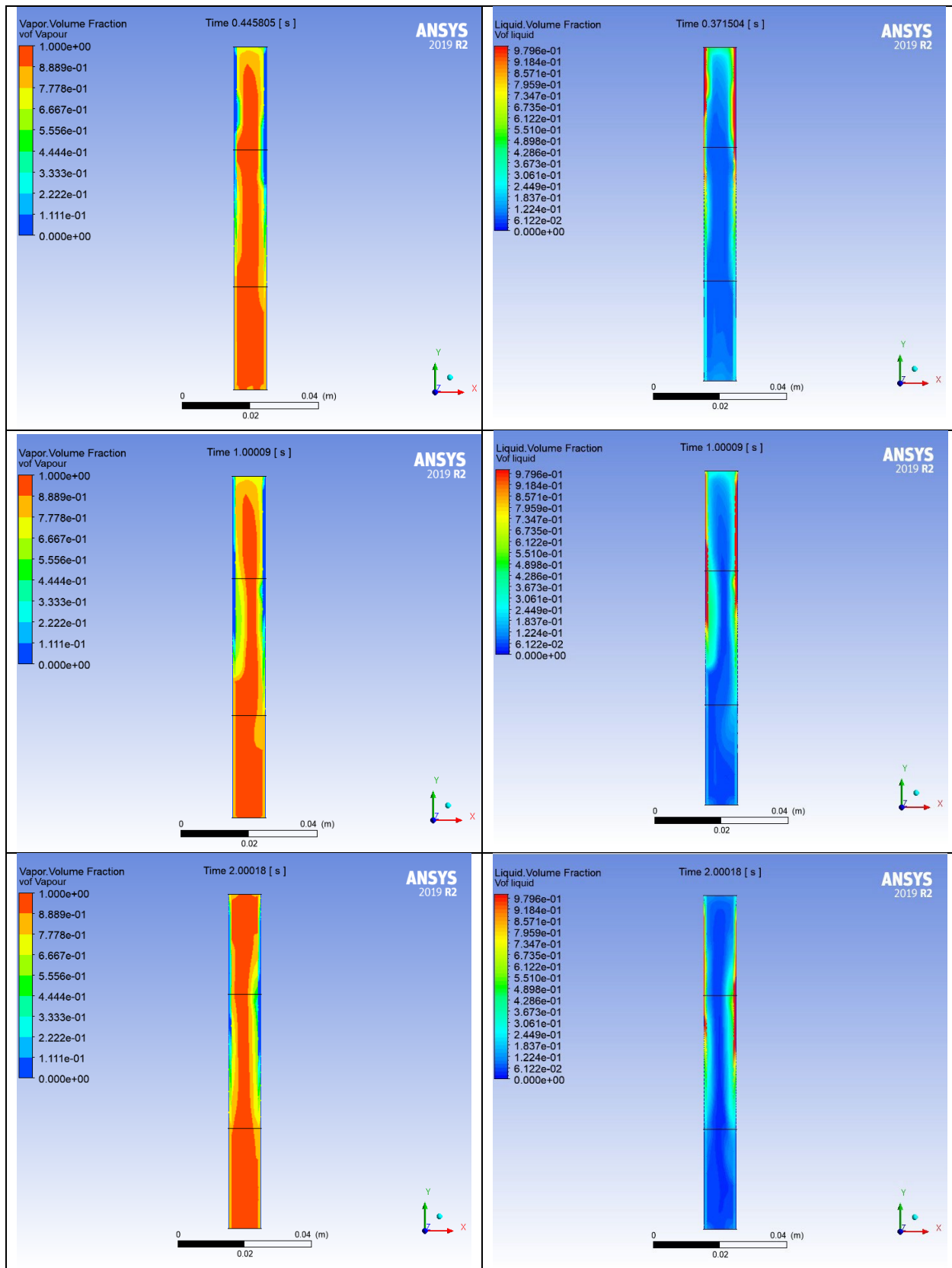


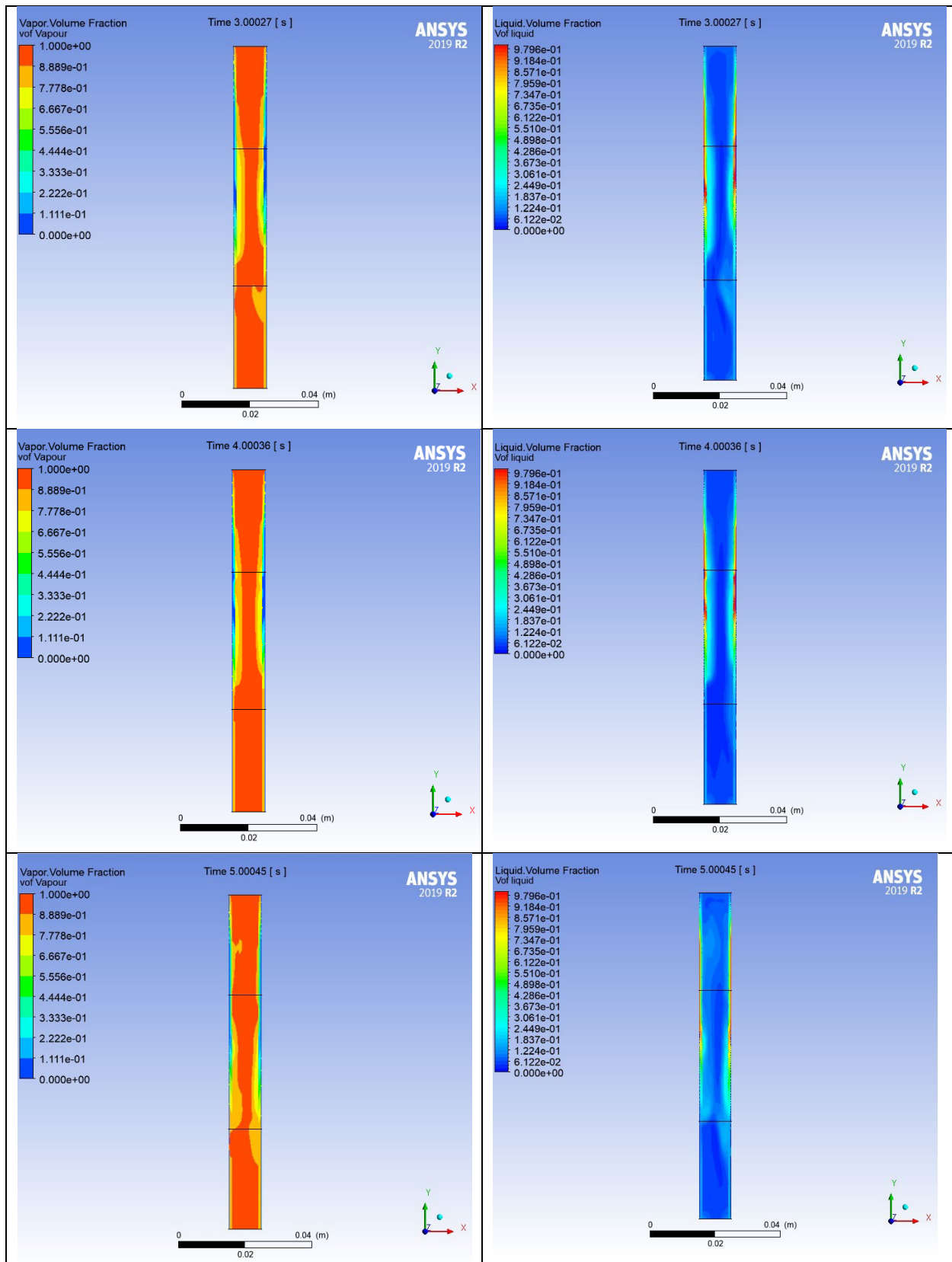
B2. Water-vapour and Water-liquid volume of fraction

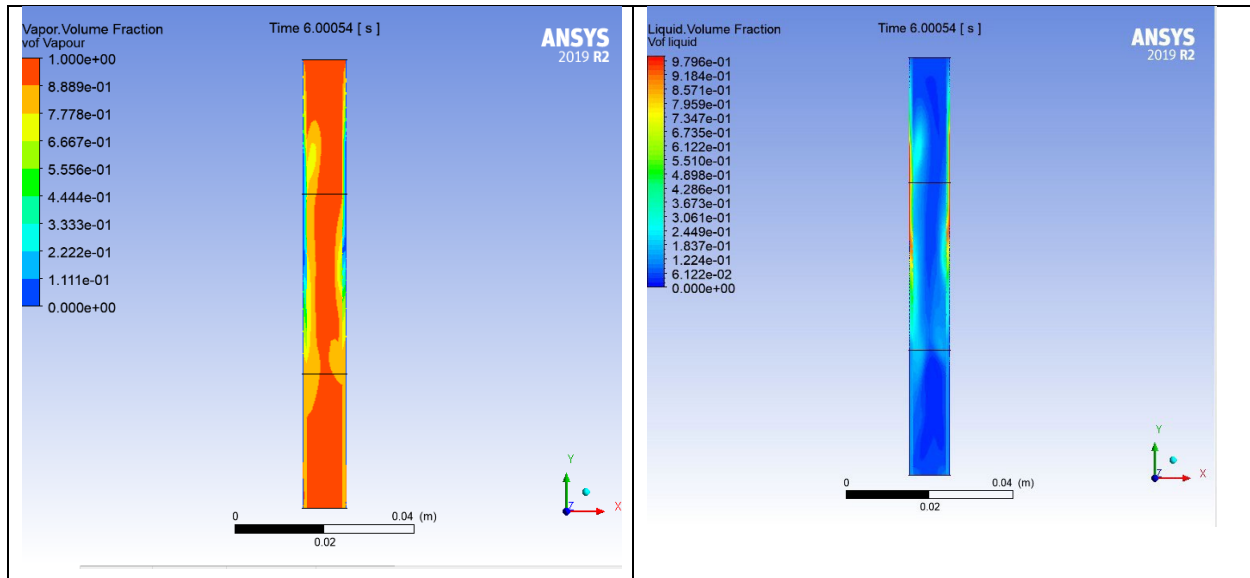




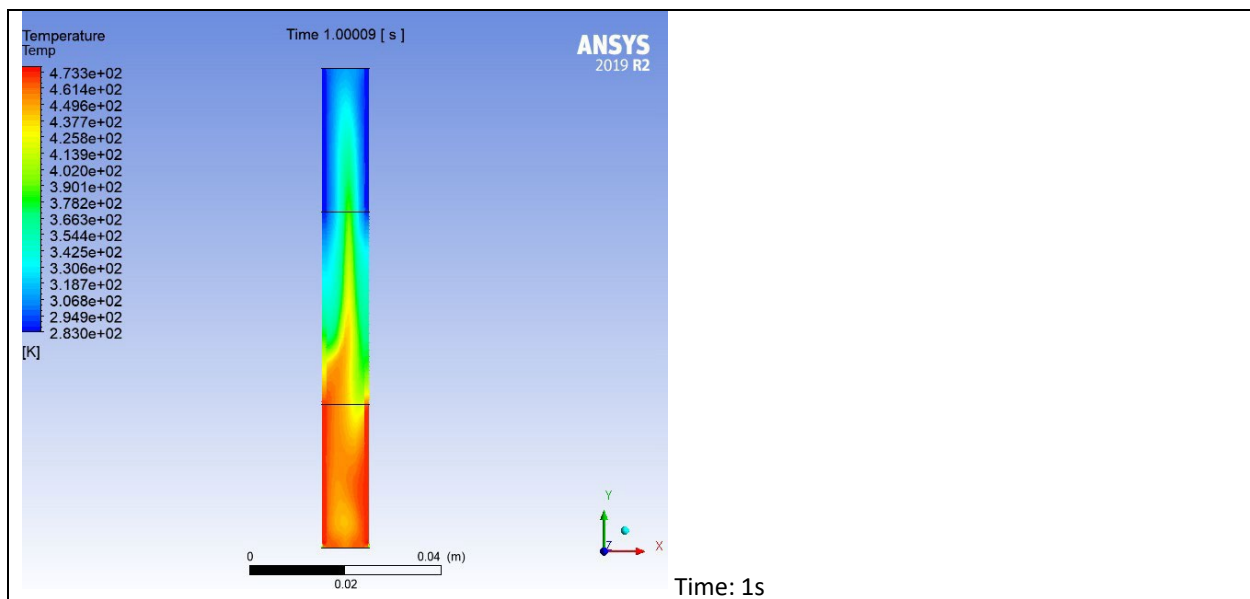


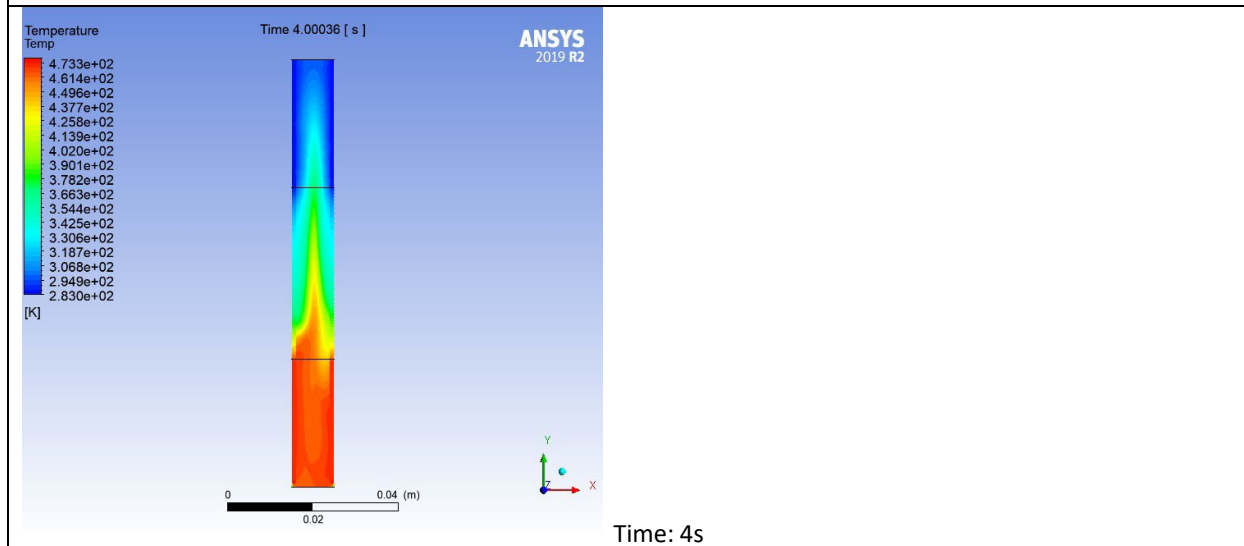
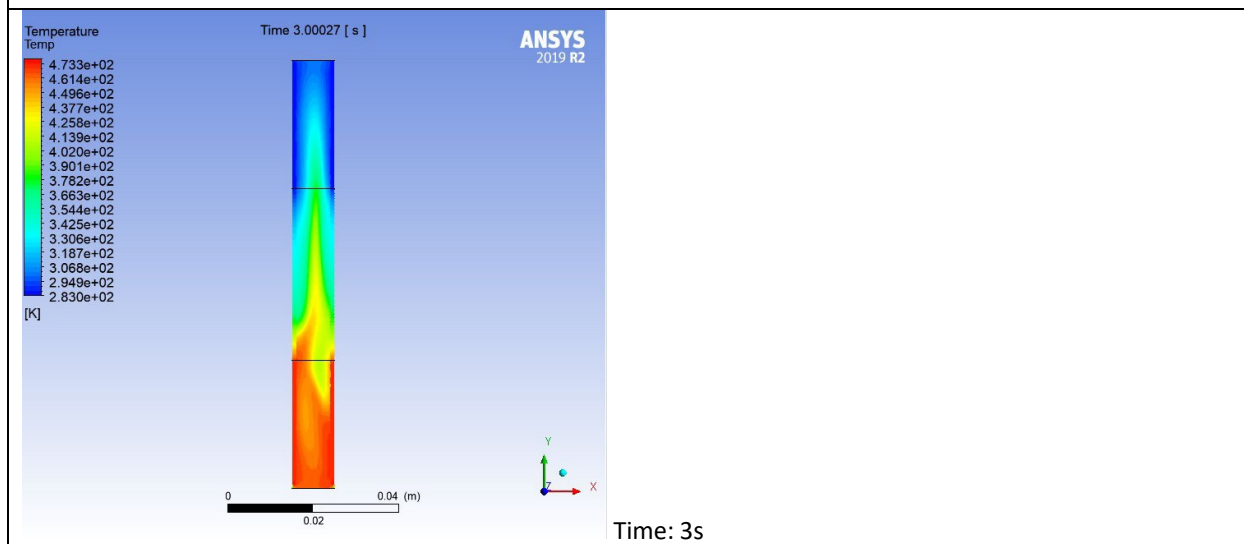
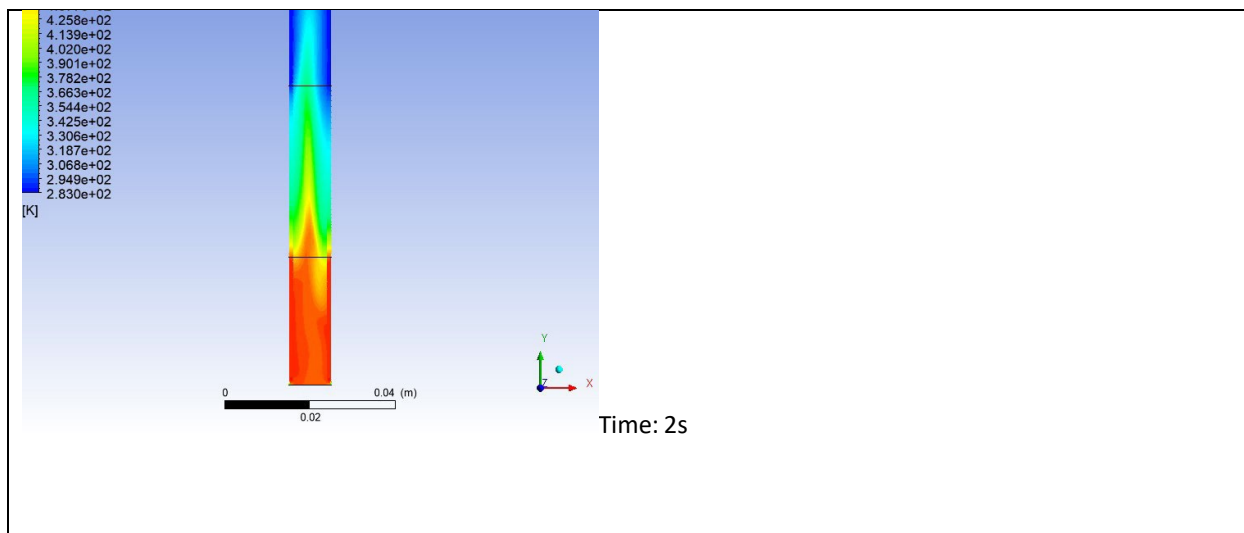


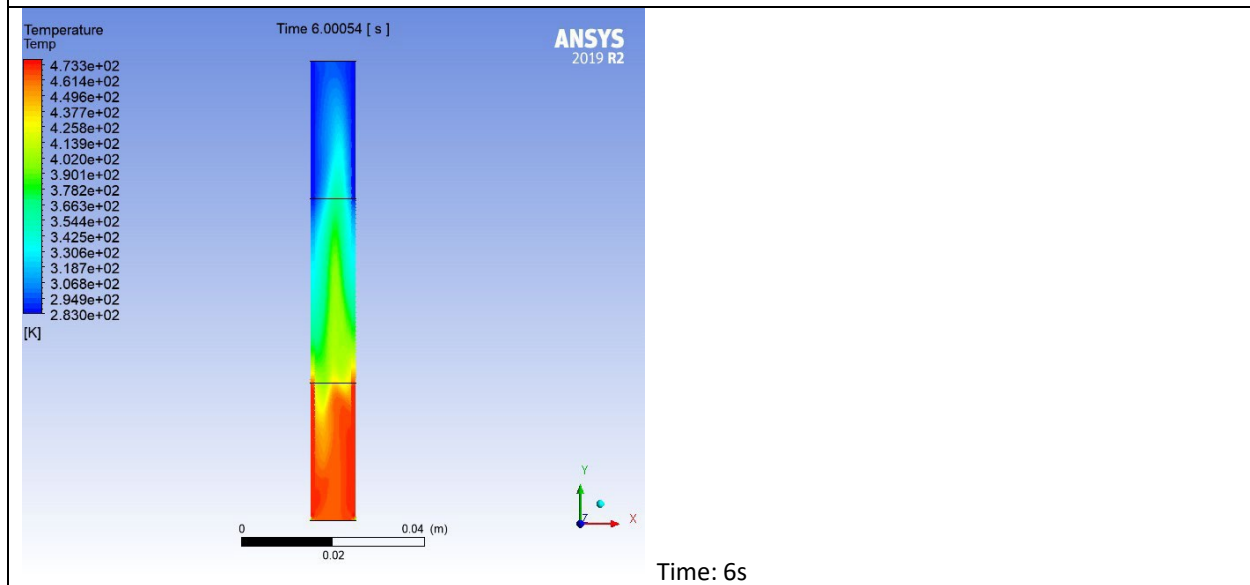
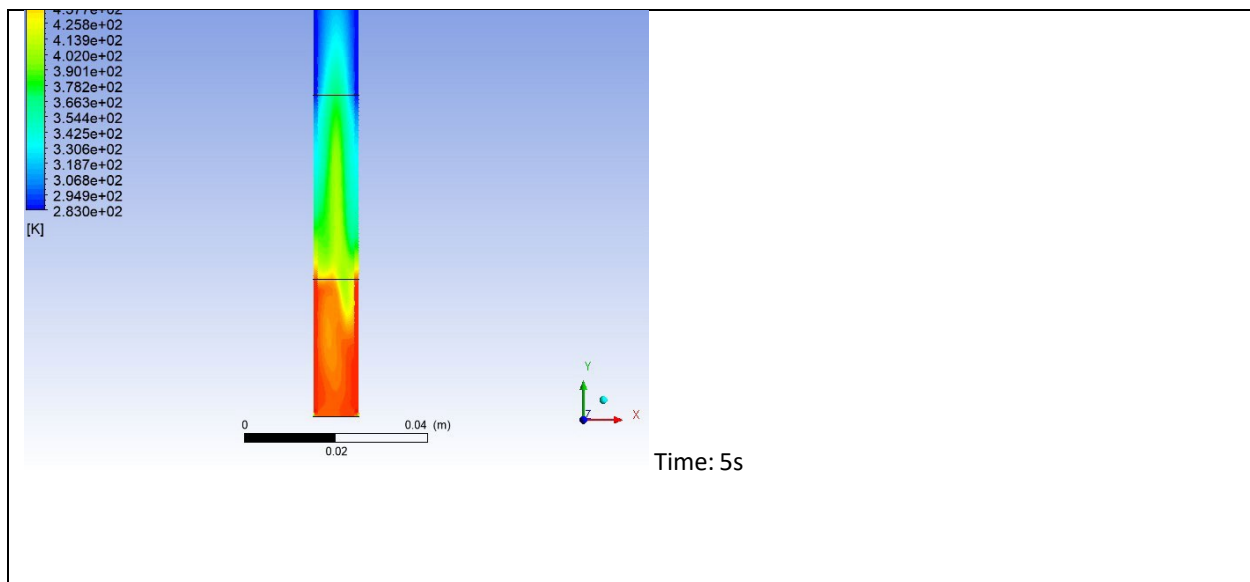




B3. Temperature profile







B4. Boundary Conditions

Table B 1: Boundary conditions for 3D vertical and horizontal Heat Pipe

Name	Type of condition	Set Parameters		
		Velocity (m/s)	Temperature (°K)	Temperature flow (W/m ²)
Evaporator	Wall	0	293.15	-
Condenser	Wall	0	303.15	-

Table B 2: Operational conditions.

Pressure (Pa)	Boiling temperature (°C)	Gravitation (m/s ²)
10000	46	9.81

Table B 3: Material conditions.

Material	Density (kg/m ³)	Thermal capacity (J/kg.K)	Thermal conductivity (W/m.K)	Dynamic viscosity (kg/m.s)
Liquid	998.2	4182	0.6	1.003×10^3
Vapour	Ideal-gas	dependence *	0.0261	1.34×10^{-5}

$$*c_p(T) = 1563.077 + 1.603755T - 0.002332784T^2 + 3.216101 \cdot 10^{-6}T^3 - 1.156527 \cdot 10^{-9}T^4$$

Table B 4: Material conditions.

Molar mass (kg/kmol)	Enthalpy (J/kmol)	Reference temperature (°C)
18.0152	0	25
18.01534	4.39952×10^7	25

Table B 5: General conditions.

Space dimension	Precision	Flow	Setting of the model
3D	double	non-stationary	evaporation – condensation: $T_{var} = 46 \text{ °C}$, $\beta_l = 0.1$, $\beta_v = 0.1$
		non-compressible, laminar	Multiphase model: mixture Liquid phase = water-liquid, Gaseous phase = water-vapor

Table B 6: Setting of the solution.

Type	Time	Coupling	Discretization	Discretization of pressure	Transient formulation
Pressure based	Transient	Coupled	Second-order upwind	PRESTO!	Bounded Second-Order Implicit

Table B 7: Multiphase Model

Multiphase Model		
Model	Formulation	Interface Modelling (Type)
Volume of Fluid; k-epsilon; RNG	Implicit	Sharp/Dispersed

Table B 8: Setting of the solution.

Under-relaxation factors	
Density	1
Body Forces	1
Pressure	0.75
Momentum	0.75
Energy	1
Volume Fraction	0.5
Vaporization Mass	1

Table B 9: Setting of the solution.

	Time Stepping method	Time step size	Number of Time steps	Max iterations/ time step	Reporting interval
3D vertical heat pipe	Fixed	0.0005	1200	150	20
3D horizontal heat pipe	Fixed	0.0005	1200	150	20
3D heat pipe (45 degrees)	Fixed	0.0005	1200	150	20

Table B 10: Geometry dimensions

Total hp length (mm)	Evaporator length (mm)	Condenser length (mm)	Wall diameter (mm)	Wick diameter (mm)	Vapour space diameter (mm)
472	94.4	377.6	12	11.2	9.7

APPENDIX C

C1. UDF code for Heat Pipe

```
#include "udf.h"

#define VAPOUR_PHASE_ID 2
#define LIQUID_PHASE_ID 3

#define POROUS_COLD_CELL_ZONE_ID 2
#define POROUS_HOT_CELL_ZONE_ID 44
#define CONDENSER_CELL_ZONE_ID 3
#define EVAPORATOR_CELL_ZONE_ID 4

#define EVAP_CONST 0.000001

#define C_EVAP_MASS_SOURCE(C,T) C_UDMI(C,T,0)
#define C_EVAP_HEAT_SOURCE(C,T) C_UDMI(C,T,1)
#define C_CAPILLARY_MOM_SOURCE_X(C,T) C_UDMI(C,T,2)
#define C_CAPILLARY_MOM_SOURCE_Y(C,T) C_UDMI(C,T,3)
#define C_CAPILLARY_MOM_SOURCE_Z(C,T) C_UDMI(C,T,4)

#define CAPILLARY_PRESSURE 0.1 /* 2.gamma.cos(theta)/R */

/* Coefficients from http://en.wikipedia.org/wiki/Antoine_equation */
/* and are for SI units and natural log */
#define ANTOINE_A 23.7836
#define ANTOINE_B 3782.89
#define ANTOINE_C -42.85

double vapour_pressure(double temp)
{
    /* get the absolute vapour pressure from temperature using the
    Antoine equation */
    double log_p;

    log_p = ANTOINE_A - ANTOINE_B/(temp + ANTOINE_C);

    return exp(log_p);
}

double boiling_temperature(double pres_abs)
{
    /* Get the boiling temperature for the absolute pressure using the
    Antoine equation */

    return (ANTOINE_B / (ANTOINE_A - log(pres_abs))) - ANTOINE_C;
}

double latent_heat_vapourisation(double temp)
{
    double temp_sq;

    temp -= 273.15; /* Equation for Celsius */
}
```



```

    temp_sq = temp*temp;

    return -0.0614342*temp_sq*temp + 1.58927*temp_sq - 2364.18*temp
+2500790.0; /* J/kg */
}

real area_factor(real volume, real vof)
{
    real factor;

    factor = pow(volume,2.0/3.0);
    factor *= 1.0 - 4.0*(vof-0.5)*(vof-0.5); /* = 1.0 at VOF=0.5, 0.0 at
VOF = 0.0 or 1.0 */

    return factor;
}

void set_evaporation_sources(Thread *lct, Thread *lct)
{
    real p_vapour;
    real mass_source;
    cell_t c;
    real vol;

    begin_c_loop(c,lct)
    {
        p_vapour = vapour_pressure(C_T(c,lct));
        vol = C_VOLUME(c,lct);
        /* Mass source positive if evaporating */
        mass_source = EVAP_CONST * (p_vapour - (C_P(c,lct) + op_pres)) *
area_factor(vol, C_VOF(c,lct)) / vol; /* Sources are volumetric */

        C_EVAP_MASS_SOURCE(c,lct) = mass_source;

        if (mass_source > 0.0)
            C_EVAP_HEAT_SOURCE(c,lct) = mass_source * C_H(c,lct);
        else
            C_EVAP_HEAT_SOURCE(c,lct) = mass_source * C_H(c,vct);
    }
    end_c_loop(c,lct)
}

void set_capillary_pressure_sources(Thread *lct, real *direction)
{
    cell_t c;
    real vol;
    real capillary_force;

    begin_c_loop(c,lct)
    {
        vol = C_VOLUME(c,lct);
        capillary_force = CAPILLARY_PRESSURE * area_factor(vol,
C_VOF(c,lct)) / vol;

```

```

ND_VS(C_CAPILLARY_MOM_SOURCE_X(c,lct),C_CAPILLARY_MOM_SOURCE_Y(c,lct),C_CA
PILLARY_MOM_SOURCE_Z(c,lct),=,direction,*,capillary_force);
    }
    end_c_loop(c,lct)
}

DEFINE_ADJUST(set_heat_pipe_sources, mixture_domain)
{
    Domain *liquid_domain;
    Domain *vapour_domain;
    Thread *lct;
    Thread *vct;
    real capillary_direction[ND_ND];

    liquid_domain = Get_Domain(LIQUID_PHASE_ID);
    vapour_domain = Get_Domain(VAPOUR_PHASE_ID);

    Message("\nOperating Pressure %f (Pa)\n",op_pres);
    Message("Boiling temperature at this pressure is %f
(K)\n",boiling_temperature(op_pres));

    Message("Setting sources in the evaporator... ");

    lct = Lookup_Thread(liquid_domain, EVAPORATOR_CELL_ZONE_ID);
    vct = Lookup_Thread(vapour_domain, EVAPORATOR_CELL_ZONE_ID);

    set_evaporation_sources(lct, vct);

    NV_D(capillary_direction,=,1.0,1.0,0.0);
    set_capillary_pressure_sources(lct,capillary_direction);

    Message("Done.\n");

    Message("Setting sources in the condenser... ");

    lct = Lookup_Thread(liquid_domain, CONDENSER_CELL_ZONE_ID);
    vct = Lookup_Thread(vapour_domain, CONDENSER_CELL_ZONE_ID);

    set_evaporation_sources(lct, vct);

    NV_D(capillary_direction,=,1.0,0.0,0.0);
    set_capillary_pressure_sources(lct,capillary_direction);

    Message("Done.\n");

    Message("Setting sources in the adiabatic porous zones... ");

    lct = Lookup_Thread(liquid_domain, POROUS_COLD_CELL_ZONE_ID);
    vct = Lookup_Thread(vapour_domain, POROUS_COLD_CELL_ZONE_ID);
    /* set_evaporation_sources(lct, vct); */

    NV_D(capillary_direction,=,1,-10.0,0.0);

```

```

    set_capillary_pressure_sources(lct, capillary_direction);

    lct = Lookup_Thread(liquid_domain, POROUS_HOT_CELL_ZONE_ID);
    vct = Lookup_Thread(vapour_domain, POROUS_HOT_CELL_ZONE_ID);
    /* set_evaporation_sources(lct, vct); */

    NV_D(capillary_direction,=,1,10.0,0.0);
    set_capillary_pressure_sources(lct, capillary_direction);

    Message("Done.\n");
}

DEFINE_SOURCE(vapour_mass_source, c, ct, ds, eqn)
{
    return C_EVAP_MASS_SOURCE(c, ct); /* Mass source positive if
evaporating */
}

DEFINE_SOURCE(liquid_mass_source, c, ct, ds, eqn)
{
    return -C_EVAP_MASS_SOURCE(c, ct); /* Mass source positive if
evaporating */
}

DEFINE_SOURCE(vapour_heat_source, c, ct, ds, eqn)
{
    return C_EVAP_HEAT_SOURCE(c, ct); /* Heat source positive if
evaporating */
}

DEFINE_SOURCE(liquid_heat_source, c, ct, ds, eqn)
{
    return -C_EVAP_HEAT_SOURCE(c, ct); /* Heat source positive if
evaporating */
}

DEFINE_SOURCE(capillary_mom_x_source, c, ct, ds, eqn)
{
    return C_CAPILLARY_MOM_SOURCE_X(c, ct);
}

DEFINE_SOURCE(capillary_mom_y_source, c, ct, ds, eqn)
{
    return C_CAPILLARY_MOM_SOURCE_Y(c, ct);
}

DEFINE_SOURCE(capillary_mom_z_source, c, ct, ds, eqn)
{
    return C_CAPILLARY_MOM_SOURCE_Z(c, ct);
}

```

C2. UDF to reset the operating pressure

```
#include "udf.h"

DEFINE_ON_DEMAND(reset_operating_pressure)
{
    #if !RP_HOST
        Domain *domain;
        Thread *t;

        real p_min;

        domain = Get_Domain(ROOT_DOMAIN_ID);

        /* Find minimum pressure in domain */

        p_min = REAL_MAX;

        thread_loop_c (t,domain)
        {
            if (NNLLP(THREAD_STORAGE(t,SV_P)))
            {
                cell_t c;

                begin_c_loop_int(c,t)
                {
                    if(C_P(c,t) < p_min) p_min = C_P(c,t);
                }
                end_c_loop_int(c,t)
            }
        }

        p_min = PRF_GRLow1(p_min);

        thread_loop_c (t,domain)
        if (NNLLP(THREAD_STORAGE(t,SV_P)))
        {
            cell_t c;

            begin_c_loop(c,t)
            {
                C_P(c,t) -= p_min;
            }
            end_c_loop(c,t)
        }

        thread_loop_f(t,domain)
        {
            Thread *t0 = t->t0;
        }
    }
}
```

```

if (FLUID_THREAD_P(t0))
  switch (THREAD_TYPE(t))
  {
    case THREAD_F_SLIDING_BOUNDARY:
      break;

    case THREAD_F_PERIODIC:
      if (NNULLP(THREAD_STORAGE(t,SV_P)))
      {
        face_t f;

        begin_f_loop (f,t)
        {
          F_P(f,t) -= p_min;
          F_P(F_SHADOW(f,t),t) = F_P(f,t);
        }
        end_f_loop (f,t)
      }
      break;

    case THREAD_F_PINLET:
    case THREAD_F_POUTLET:
      Message0("\nWARNING: Pressure boundary conditions must be
reset to match change in operating pressure (%f).",p_min);
      break;

    default:
      /* If it looks like a duck... */
      if (NNULLP(THREAD_STORAGE(t,SV_P)))
      {
        face_t f;

        begin_f_loop (f,t)
        {
          F_P(f,t) -= p_min;
        }
        end_f_loop (f,t)
      }
      break;
  }
}

Message0("\nOperating pressure changed from %f to ",op_pres);
op_pres += p_min;
Message0("%f.\n",op_pres);
#endif /* !RP_HOST */

node_to_host_real_1(op_pres);

#ifdef !RP_NODE
  RP_Set_Real("operating-pressure",op_pres);
#endif /* !RP_NODE */
}

```